TECHNISCHE
UNIVERSITÄT
DARMSTADT

Fachbereich Physik
GSI Theorie

# Structure of isomultiplets in $A$=8 and $A$=9 nuclei in the framework of Fermionic Molecular Dynamics

## Struktur von Isomultipletts in $A$=8 und $A$=9 Atomkernen im Rahmen der Fermionischen Molekulardynamik

Vom Fachbereich Physik
der Technische Universität Darmstadt

Zur Erlangung des Grades
eines Doktors der Naturwissenschaften (Dr. rer. nat.)

genehmigte Dissertation von
K. R. Henninger, M.Sc.
aus King William's Town (Südafrika)

Referent: Prof. Dr. Hans Feldmeier
Korreferent: Prof. Dr. Gabriel Martinez-Pinedo

Tag der Einreichung: 14.12.2015
Tag der Prüfung: 11.01.2016

Darmstadt 2016
D 17

# Structure of isomultiplets in $A$=8 and $A$=9 nuclei in the framework of Fermionic Molecular Dynamics

## Struktur von Isomultipletts in $A$=8 und $A$=9 Atomkernen im Rahmen der Fermionischen Molekulardynamik

Genehmigte Dissertation von K. R. Henninger, M.Sc.
aus King William's Town (Südafrika)

Referent: Prof. Dr. Hans Feldmeier
Korreferent: Prof. Dr. Gabriel Martinez-Pinedo

Tag der Einreichung: 14.12.2015
Tag der Prüfung: 11.01.2016

Darmstadt 2016
D 17

Bitte zitieren Sie dieses Dokument als:
URN: urn:nbn:de:tuda-tuprints-52818
URL: http://tuprints.ulb.tu-darmstadt.de-5281

## Erklärung zur Dissertation

Hiermit versichere ich, die vorliegende Dissertation ohne Hilfe Dritter nur mit den angegebenen Quellen und Hilfsmitteln angefertigt zu haben. Alle Stellen, die aus Quellen entnommen wurden, sind als solche kenntlich gemacht. Diese Arbeit hat in gleicher oder ähnlicher Form noch keiner Prüfungsbehörde vorgelegen.

Darmstadt, den February 24, 2016

(K.R. Henninger)

## Zusammenfassung

Schwach gebundene Kerne treten als Vermittler in der Kernsynthese stabiler Kerne auf. Aus diesem Grund besitzen theoretische Modelle schwach gebundener Kernmaterie viele Anwendungen in der Astrophysik. Diese Doktorarbeit befaßt sich mit den schwach gebundenen Kernen des ($A = 8$)-Isotripletts und des ($A = 9$)-Isodupletts, welche eine (entscheidende) Rolle in astrophysikalischen Reaktionen spielen.

Falls ein Kern schwach gebunden ist, befindet sich der Grundzustand nahe einer Zerfallsschwelle. Dies bedeutet, daß man Clusters und manchmal Halos im Grundzustand oder in anderen niedrig liegenden Zuständen schwach gebundener Kerne beobachtet. Solcher Strukturen wird manchmal durch den Ausdruck “Kopplung an das Kontinuum” Bezug genommen, da sie eine Beimischung von Streulösungen zur Wellenfunktion darstellen. Ihr Beitrag beeinflußt den asymptotischen Teil der Wellenfunktion, welcher wiederum auf berechnete Reaktionsraten einen schwerwiegenden Einfluß hat. Jedoch sind Cluster und Halokerne schwierig zu modellieren, da es Schwierigkeiten bereitet, Zugang zu räumlich ausgedehnten oder anisotropen Verteilungen ohne größere Modellräume zu erlangen. Das Ziel dieses Projekts ist es, den Grundzustand und die angeregten Zustände des ($A = 8$)-Isotripletts ($^{8}$Li, $^{8}$Be und $^{8}$B) und des ($A = 9$)-Isodupletts ($^{9}$Be und $^{9}$B) im Fermionischen Molekulardynamik-Modell (FMD-Modell) zu modellieren.

Die Kerne $^{8}$Li, $^{8}$Be, $^{8}$B, $^{9}$Be und $^{9}$B stellen ein reichhaltiges Forschungsgebiet zur Verfügung, da sie alle (mit Ausnahme des stabilen $^{9}$Be) im Grundzustand schwach gebunden (oder, wie im Falle des $^{8}$Be, ungebunden) sind. Sie alle spielen eine wichtige Rolle in der Astrophysik, so z. B. beim Fluß solarer Neutrinos und der Proton-Proton Kettenkernsynthese in Sternen mit solarer Masse. Von all diesen Kernen wird auch erwartet, interessante Phänomene wie Clusterbildung oder die Bildung von Halokernen im Grundzustand aufzuweisen. Die für diese Arbeit interessanten Strukturen sind die Folgenden: der Einproton-Halokern von $^{8}$B, die borromäische Clusterstruktur von $^{9}$Be und die Clusterstrukturen von $^{9}$B, $^{8}$Be und $^{8}$Li.

Schwach gebundene Spiegelkerne sind ebenso von allgemeinem Interesse: Die Energien und andere Eigenschaften, welche mit schwach gebundenen Kernen verknüpft sind, werden oft durch Messungen an Spiegelkernen gewonnen. Es ist wünschenswert zu wissen, wie genau diese bei der Behandlung von schwach gebundenen Systemen sind, da der Coulombbeitrag als der die Isospinsymmetrie vorrangig verletzende Term durch die schwache Bindung von Protonen beeinflußt werden kann, welche in der Nähe einer Zerfallsschwelle durch Teilchenemission auftreten kann (insbesondere bei der Thomas-Ehrman-Verschiebung). Ein zweites Ziel dieser Doktorarbeit ist deshalb, den Einfluß struktureller Unterschiede bei analogen Energieniveaus in den Spiegelkernen $^{8}$Li-$^{8}$B und $^{9}$Be-$^{9}$B zu untersuchen.

Im FMD-Modell ist es nicht notwendig, *a priori*-Annahmen bezüglich der Clusterstruktur zu machen. Trotzdem können sowohl Clusterstrukturen als auch kompakte (“schalenmodellartige”) Zustände gleich gut behandelt werden. Dies wird beispielhaft durch die Behandlung des in erster Anregung vorliegenden $0^{+}$-Zustands (Hoyle-Zustands) von $^{12}$C, und durch den Ladungsradius des $1^{-}$-Halozustands von $^{10}$Be erläutert. Das FMD-Modell ist ein mikroskopisches Modell, das die Kernstruktur in einer Wellenpaketbasis beschreibt. In der vorliegenden Arbeit konstruieren wir den Vielteilchen-Hilbertraum aus den antisymmetrisierten, hinsichtlich des Drehimpulses und der Parität projizierten Acht- und Neunteilchenzuständen, und legen die Kernwellenfunktionen des Grundzustands und einiger angeregter Zustände durch Diagonalisierung einer Argonne-V18-Wechselwirkung in dieser Basis fest. Verschiedene Observablen werden berechnet und mit den experimentellen Daten für jeden Kern verglichen.

Da $^{8}$Be einer jener Kerne ist, die in dieser Arbeit untersucht werden, wird die Fähigkeit des FMD-Modells, Zugang sowohl zu kompakten als auch zu clusterartigen Konfigurationen zu erlangen, besonders nützlich, weil der Grundzustand von $^{8}$Be durch eine Zweialpharesonanz gebildet wird, wohingegen die höherliegenden ($T = 1$)-Zustände kompakt sind. (Die Alphacluster können keine ($T = 1$)-Zustände

bilden.) In dieser Arbeit werden zwei neue Ansätze verfolgt, um die $(T = 1)$-Zustände der $^{8}$Be-Zustände zu modellieren. Bei diesen Ansätzen handelt es sich auf der einen Seite um die Einbeziehung der Isospinpartnerzustände der $^{8}$B- und $^{8}$Li-Zustände in der $^{8}$Be-Basis, auf der anderen Seite um die Festlegung von Nebenbedingungen für die $\langle \hat{\vec{T}}^{2} \rangle$- und $\langle \hat{\vec{S}}^{2} \rangle$-Werte der Basiszustände von $^{8}$Be.

Die Ergebnisse geben die experimentellen Eigenschaften des $(A = 8)$-Isotripletts und des $(A = 9)$-Isodupletts gut wieder. Von besonderer Bedeutung ist die Tatsache, daß die Berechnungen den Protonhalokern von $^{8}$B und die $(T = 1)$-Zustände von $^{8}$Be reproduzieren; Letztere bestätigt, daß das FMD-Modell in der Lage ist, sowohl die Clusterbildung als auch die schalenmodellartigen Zustände konsistent hervorzubringen. Die für das $(A = 8)$-Isotriplett berechneten Energieniveaus werden mit den neuesten Ergebnissen des No-Core-Schalenmodells verglichen und weisen eine beeindruckende Übereinstimmung auf, welche darauf hindeutet, daß dieses Vorgehen konkurrenzfähig zu den derzeitig anerkannten Methoden ist.

## Contents

# 1 Introduction

## 1.1 Motivation and Outline

Weakly-bound nuclei (which we will define as nuclei with a binding energy of less than 5 MeV/nucleon, or with a ground state that lies within ~100 keV of a decay threshold), occur as intermediates in the nucleosynthesis of stable nuclei [1,2]. For this reason, theoretical models of weakly-bound nuclear structure have many applications in astrophysics, among which are calculating nucleosynthetic reaction rates and determining the location of the driplines. This thesis concerns itself with the weakly-bound nuclei of the $A$=8 isotriplet and the $A$=9 isodoublet; all of which play a role in astrophysical reactions.

When a nucleus is weakly-bound, the ground-state is proximal to a decay threshold, either for nucleon- or $\alpha$-particle emission. As clustering occurs near thresholds for decay by particle emission [3], one observes clusters and sometimes even haloes in the ground- or low-lying states of weakly-bound nuclei. These structures contribute to the asymptotic part of the wave function.

Both clustering and haloes are difficult to model microscopically, as it is difficult to access spatially-extended or spatially-anisotropic distributions without large model-spaces. One requires a superposition of many states to reproduce spatially-anisotropic distributions starting from basis distributions with spatial isotropy (as in an harmonic-oscillator basis). The model-spaces required for such calculations thus soon become intractably-large. Theoretical models of halo and cluster structures are, however, highly-desirable for applications in *e.g.* calculation of nucleosynthetic reaction rates.

The nuclei $^8$Li, $^8$Be, $^8$B, $^9$Be and $^9$B provide a rich field of study, as all these (with the exception of the stable $^9$Be) are weakly-bound in the ground state (or unbound, in the case of $^8$Be). They are also all expected to show interesting behaviours like clustering or haloes in the ground state. Structures of interest are: the one-proton halo in $^8$B [4], the clustering, Borromean structure of $^9$Be, and the clustering structures in $^9$B, $^8$Be and $^8$Li [5]. Weakly-bound mirror pairs are also of general interest: energy levels and other properties such as reaction rates are often derived from measurements on the mirror nucleus, because weakly-bound nuclei are themselves produced at extremely low yields at astrophysically-relevant energies. One would wish to know how appropriate or accurate it is to use energy levels from the mirror nucleus, and how one would compensate for discrepancies between the mirror system and the weakly-bound nucleus itself. This has validity especially in the $^8$Li-$^8$B pair, for which much investigative theoretical work on the radiative-capture reaction $^7\text{Li}+\text{p}\to^8\text{B}+\gamma$ has been done using the mirror system $^7\text{Li}+\text{n}\to^8\text{Li}+\gamma$ (see [6] and refs. therein).

Several terms in the nucleon-nucleon interaction are isospin-symmetry breaking and thus lift the degeneracy of analogous energy levels in an isomultiplet. The Coulomb term is perhaps the most well-known of these. Additional isospin-symmetry breaking terms arise from the difference in the mass of charged and neutral pions (which affects the long-range part of the internucleon interaction). There is also the fact that the proton and neutron themselves have different masses, which can lead to a substantial difference in the kinetic energy term between isospin partner nuclei.

Nuclear Coulomb energy can, of course, be affected by proximity to a threshold for decay by particle emission, as in the example of the Thomas-Ehrman shift [7,8]. This shift is a special case involving analogous energy levels on either side of the threshold for proton emission in mirror nuclei. However, one can argue that the presence of any particle-emission threshold, not just a threshold for proton emission, will break the degeneracy of mirror levels in a way that is certainly outside treatment using “uniform sphere” approximations of the Coulomb energy [9]: near a threshold, sphericity is affected by clustering, especially in the asymptotic part of the wave function. A more accurate method of calculating Coulomb energy may take these shifts of energy into account. Such properties observed in proximity to a threshold for particle emission, and requiring an accurate reproduction of the asymptotics of the wave function, are often discussed under the umbrella of “coupling to the continuum”, or “continuum-coupling effects”, and of course have special relevance in weakly-bound nuclei, where the continuum plays an important role.

Both the $^{8}$Li-$^{8}$B and $^{9}$Be-$^{9}$B mirror systems have been in the spotlight regarding “missing” states: In the $^{9}$Be-$^{9}$B system, there is the well-known controversy about the first-excited $1/2^{+}$ state (see [10] and refs. therein), which appears at 1.684 MeV above the $^{9}$Be ground state [5] and for which the corresponding state in $^{9}$B has never been positively identified. There is also a proposed low-lying first-excited $0^{+}$ level in $^{8}$B [11], which has not been observed in $^{8}$Li [5].

In order to model weakly-bound nuclei, one must access both compact nuclear configurations and extended distributions. In this endeavor the dominant problem is having an adequate Hilbert space (one that accesses all relevant behaviour without being intractably-large). For this, Fermionic Molecular Dynamics (FMD) [12] is ideally-suited. Not only is it capable of accessing both cluster structures and shell-model type structures within a tractable model space, but it also allows for consistent treatment of these different extremes of structure, without having to make recourse to different models or approaches for modeling the external region.

The aim of this project is to determine the structure of the ground state and excited states for the $A$=8 isomultiplet ($^{8}$Li, $^{8}$Be and $^{8}$B), and the $A$=9 isodoublet ($^{9}$Be and $^{9}$B) in the FMD model. As is discussed in more detail later, FMD offers an extraordinarily flexible basis, and can access both halo and cluster structures [13]. In this model, it is not necessary to make *a priori* assumptions of cluster structure, but both clustering and shell-model type states can be treated equally-well [13]. This is exemplified by its treatment of the first excited $0^{+}$ state (Hoyle state) of $^{12}$C [14] or the charge radii of the Be isotopes [15]. As $^{8}$Be is one of the nuclei in this work, this ability to access both shell model and clustering states becomes particularly useful, since $^{8}$Be is an unusual nucleus in that the ground state is just above the two-alpha threshold and hence a two $\alpha$ cluster configuration, [5], while the higher-lying $T=1$ states can be expected to have a “shell-model like” character, given that the $\alpha$-clusters must break to access $T=1$ states.

Since $^{8,9}$B are both included in this study, $^{10}$B will also be modeled, both for comparison to calculations of a stable nucleus, and to investigate structural trends in the Boron isotopic chain. A model of the structure of nuclear ground- and excited-states allows evaluation of observables like root mean square (rms) radii and transition strengths, for comparison to experiment.

Particular areas of interest and challenges here include modeling the structure of $^{8}$Be, given the shell-model like and alpha-clustering states: a challenge for any model. Investigating the change in structure along the Boron isotopic chain, and the reproduction of the “missing” $0^{+}$ and $1/2^{+}$ states, respectively, in $^{8}$Li and $^{9}$B, are also interesting regions of study.

This thesis is structured as follows: In Sections 1.4 to 2.1, background information on clusters, haloes and the nuclei $^{8}$B, $^{8}$Be, $^{8}$Li, $^{9}$Be and $^{9}$B is discussed, to put this study in context. Section 5 discusses FMD in more detail, and Section 6.5 discusses the calculations and presents the results.The results are discussed in Section 7.

## 1.2 Coupling to the Continuum

### 1.2.1 Coupling to the continuum in the sense of interaction

The term "coupling to the continuum" should be discussed at this point, since it is often used with reference to asymptotic structure near particle-decay thresholds, but its meaning may be unclear.

The usual definition of "coupling" is that two states ($|\phi\rangle$ and $|\psi\rangle$, say) have a non-vanishing matrix element under an interaction $\hat{V}$, or $\langle\phi|\hat{V}|\psi\rangle \neq 0$: the states $|\phi\rangle$ and $|\psi\rangle$ are coupled by $\hat{V}$. Likewise one defines the coupling of subspaces of the Hilbert spaces $\mathscr{H}_1$ and $\mathscr{H}_2$, where $|\phi\rangle \in \mathscr{H}_1$ and $|\psi\rangle \in \mathscr{H}_2$. Already at this point the question arises as to what is meant by the term interaction $\hat{V}$. One often tacitly-assumed picture is the decomposition of the system's Hamiltonian

$$\hat{H} = \hat{H}_0 + \hat{V} \tag{1.1}$$

into an $\hat{H}_0$ part that has a known or easy-to-solve eigenrepresentation

$$\hat{H}_0|\Phi_i\rangle = E_i^0|\Phi_i\rangle \tag{1.2}$$

like the kinetic energy or a one-body mean field Hamiltonian.

The (remaining) interaction $\hat{V}$ couples the $\hat{H}_0$ eigenstates $|\Phi_i\rangle$ in the sense $\langle\Phi_i|\hat{V}|\Phi_j\rangle \neq 0$.

For the case of a typical nuclear one-body mean field (Wood-Saxon or Hartree-Fock), the single-particle eigenstates $|\psi_i\rangle$ consist of a finite number of bound states and not-normalisable scattering states. As the nuclear interaction between a nucleon and the mean field generated by the remaining nucleons that form the core ceases at large distances, one sets the energy scale such that the $\epsilon_i < 0$ correspond to localised bound states and the $\epsilon_j(k) \geq 0$ to scattering states. Note that the discrete quantum number $i$ turns into a continuous one labelled $k$ and a discrete one $j$ (the discrete part denoting spin and isospin). The single-particle energy

$$\epsilon_j(k) = \frac{k^2}{2\mu} \tag{1.3}$$

is usually written in terms of the asymptotic wavenumber $k = \frac{2\pi}{\lambda}$ of the scattering state with wavelength $\lambda$.

The many-body eigenstates of $\hat{H}_0$ are Slater determinants specified by occupation numbers

$$n^a = \left\{n_1^a, n_2^a ...\right\}, n_i^a = 0 \text{ or } 1, \sum_{i=1}^{\infty} n_i^a = A \tag{1.4}$$

and

$$\hat{H}_0|\Phi^a\rangle = E_0^a|\Phi^a\rangle \tag{1.5}$$

where the eigenenergy is the sum over single-particle energies of the occupied states

$$E_0^a = \sum_{i=1}^{\infty} n_i^a \epsilon_i \tag{1.6}$$

In the mean field picture it is quite conceivable that for the bound many-body ground state of an exotic nucleus the corresponding lowest mean field eigenstates cannot accomodate all nucleons in bound states ($\epsilon_i < 0$), but one or more nucleons (usually neutrons) have to be put in continuum single-particle particle states. But due to the residual interaction $\hat{V}$ the ground state of the total Hamiltonian $\hat{H} = \hat{H}_0 + \hat{V}$ is spatially-localised, with the last neutron or neutrons in a kind of halo that extends far out.

This situation describes the meaning of "coupling to the continuum": The residual interaction couples two- or many-body states made from bound single-particle states to those where at least one single-particle state $\hat{H}_0$ is in the continuum.

### 1.2.2 Coupling to the continuum in the sense of overlap with continuum states

Any eigenstate of the Hamiltonian $\hat{H} = \hat{H}_0 + \hat{V}$ can be expanded in terms of the $\hat{H}_0$ eigenstates

$$\begin{aligned} \hat{H}|\Psi_n\rangle &= E_n|\Psi_n\rangle, \\ \text{where} \quad |\Psi_n\rangle &= \sum_{n^a} |\Phi^a\rangle\langle\Phi^a|\Psi_n\rangle \end{aligned} \tag{1.7}$$

and $\sum_{n^a}$ refers to the sum over all Slater determinants specified by the set of occupation numbers $n^a$ (Eq.(1.4)).

It is obvious that a sum that includes continuum states $|\Phi^a\rangle$, *i.e.* $\langle\Phi^a|\Psi_n\rangle \neq 0$ for $|\Phi^a\rangle$ in which single-particle scattering states are occupied, has to superimpose the $\hat{H}_0$ scattering states such that they form a many-body wavepacket with finite extension. With that in mind, one sometimes simplifies the discussion by calling a non-vanishing overlap $\langle\Phi^a|\Psi_n\rangle \neq 0$ for $|\Phi^a\rangle$ containing unbound scattering states "coupling to the continuum".

When making such a simplification, one should however keep in mind that when speaking about "coupling to the continuum", one should also specify *which* $\hat{H}_0$ is being discussed. For example, taking $\hat{H}_0 = \hat{T}$ ($\hat{T}$ being the kinetic energy) implies at once that all states, even well-bound ones, couple to the continuum, as $\hat{T}$ has only continuum eigenstates.

On the other hand, one can choose a mean field Hamiltonian $\hat{H}_0$ such that even the last nucleon occupies, in the Slater determinant with lowest $\hat{H}_0$ energy, a bound single-particle state. The residual interaction $\hat{V}$ will admix scattering states $|\Phi^a\rangle$ in order to get the correct asymptotic properties of $|\Psi_n\rangle$ at large separations from the centre of mass.

### 1.2.3 Coupling to the many-body continuum

In the previous subsections, the single-particle continuum states were discussed. These become relevant when the energy is close to one-neutron or one-proton breakup thresholds. In light nuclei, one often encounters energetically low-lying thresholds for the break up into clusters, $A \rightarrow B + C$, for example $^8$Be $\rightarrow ^4$He + $^4$He or $^{10}$B $\rightarrow ^6$Li + $^4$He. Eigenstates of the compound system $A$ at energies close to the threshold are expected to behave asymptotically as two clusters, $B$ and $C$, with small overlap, with exponentially-decaying relative wavefunctions, or, if the energy is just above the threshold, as resonances that match to scattering states in the relative motion of $B$ and $C$.

All discussions of Subsections 1.2.1 and 1.2.2 which considered $A \rightarrow (A-1) +$ nucleon apply in an analogous (but more complex) way if we consider the many-body continuum.

As a result of the above considerations, in place of the term "coupling to the continuum" we shall therefore refer either to accurate reproduction of the asymptotics of weakly-bound nucleons, or explicitly to threshold effects.

## 1.3 Coulomb interaction and mirror nuclei

As protons and neutrons differ both in their charge and their isospin projection $t_3$, the Coulomb interaction $\hat{V}_C$ may be described using the isospin operators (see *e.g.* [16]):

$$\hat{V}_C = \sum_{i<j}^{A} \frac{e^2}{|\hat{\vec{r}}_i - \hat{\vec{r}}_j|} \left(\frac{1}{2} + \hat{t}_3(i)\right) \left(\frac{1}{2} + \hat{t}_3(j)\right), \tag{1.8}$$

where $|\vec{r}_i - \vec{r}_j|$ is the distance between nucleon $i$ and $j$, $(\frac{1}{2} + \hat{t}_3(i))$ selects on protons. This operator $\hat{V}_C$ may be written out with isospin-scalar, -vector and -tensor parts [16]:

$$\hat{V}_C = e^2 \sum_{i<j} \left\{ \underbrace{\left[\frac{1}{4} + \frac{\hat{\vec{t}}(i)\hat{\vec{t}}(j)}{3}\right]}_{\text{isoscalar}} + \underbrace{\left[\frac{\hat{t}_3(i) + \hat{t}_3(j)}{2}\right]}_{\text{isovector}} + \underbrace{\left[\hat{t}_3(i)\hat{t}_3(j) - \frac{\hat{\vec{t}}(i)\hat{\vec{t}}(j)}{3}\right]}_{\text{isotensor}} \right\} \cdot \frac{1}{|\vec{r}_i - \vec{r}_j|}. \tag{1.9}$$

The interaction would be called “charge symmetric” if the isovector term were zero, and would only be “charge independent” if both the isovector and the isotensor term were zero [16].

The Coulomb energy $E_C$ is the expectation value of $\hat{V}_C$, or

$$E_C = \langle \Psi | \hat{V}_C | \Psi \rangle, \tag{1.10}$$

where $|\Psi\rangle$ is the nuclear state for which one is calculating $E_C$.

Historically, for example in the Semi-Empirical Mass Formula of Bethe and Weizäcker, $E_C$ was calculated by assuming the nucleus is a uniformly-charged sphere of radius $R = R_0 A^{1/3}$ or:

$$E_C = \frac{3}{5} \frac{Z^2 e^2}{R_0 A^{1/3}}. \tag{1.11}$$

This assumption is rather a gross approximation, since, firstly, not all nuclei are spherical in their ground state; and secondly, one or more of the protons may have an extended distribution if the proton-to-neutron ratio is skewed towards protons, as a means of reducing the Coulomb repulsion. Both issues give the nucleus a charge radius of greater than $R_0 A^{1/3}$, and make the calculations assuming a uniformly-charged sphere slightly overestimate the Coulomb energy $E_C$. This is discussed by Nolen and Schiffer as “Coulomb perturbation” [17]. If it is not possible to treat these differences in structure when calculating the Coulomb energy, then the calculated Coulomb energy will not be sufficient to subtract out all the non-degeneracy of the analogous energy levels in the mirror-pair.

As was already mentioned, the special case of difference of level-energies in mirror nuclei in which one mirror nucleus is bound and one unbound with respect to a neutron- or proton-emission threshold is called the Thomas-Ehrman shift [18], since R.G. Thomas and J. B. Ehrman were the first to propose a way to calculate it.

## 1.4 Clustering

Clusters within nuclei (*e.g.* as in Fig. 1.1) are defined as “spatially-localised subsystems of strongly correlated nucleons” [19]. When one speaks of “clusters”, one usually means $\alpha$ clusters, because these are the most common. An $\alpha$ particle is energetically-favourable because it is the lowest energy combination of four nucleons: Two protons and two neutrons can occupy the lowest s-wave state, being four fermions in different spin or isospin states. Clustering may, however, also refer to other groupings, especially those that occur near a threshold; or even to a “core plus valence nucleons” type structure. Clusters are fairly rigid structures, so the intrinsic shape of a nucleus which exhibits clustering may be quite deformed [20]. Clustering is a result of long-range correlations [19].

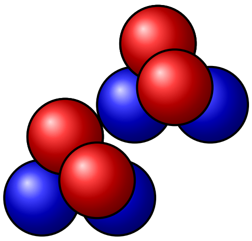

**Figure 1.1:** A schematic diagram showing a “snapshot” of $^8$Be as two alpha-clusters. The red spheres represent protons, the blue neutrons, and a possible arrangement of the two spatially-localised subsystems of nucleons — the clusters — is illustrated.

There is immediate difficulty in modelling cluster nuclei microscopically when starting with single-particle states arising from a spherically-symmetric potential well. In clustering one may consider that the system is described by nucleons in (at least) two harmonic oscillator potentials *A* and *B* — one for each cluster — with the one potential shifted from the other, as shown in in Fig. 1.2. To describe a wave function of a nucleon in potential well *B* in terms of the coordinate system which has well *A* at the origin requires a model-space that soon becomes intractably large.

As has already been discussed in Section 1.2, the origin of these clusters is in the formation of the nucleus. Until the nucleons are sufficiently close together for the average attraction between them to begin to form a single mean-field and thus to form a compound nuclear system, each smaller nucleus (or cluster) will maintain its structural integrity.

To model clustering, one must choose the appropriate degrees of freedom: those of either the nucleons or the clusters. Both approaches are valid, depending on the information in which one is interested. The first model based on the cluster degrees of freedom was developed by Hafstad and Teller in 1938 [21]. Since then, many more such have been introduced, showing much success; particularly for light nuclei [22]. Cluster models are divided into two major groups: potential cluster models (in which the nucleus is reduced to a two-body problem of one nucleon or cluster in an optical potential generated by the other cluster); or microscopic cluster models, in which all *A* nucleons are involved explicitly and arrangement into clusters is imposed. In the latter, the single nucleon degrees of freedom are used, despite it being called a cluster model.

There are also microscopic models that can access clustering. These include No-Core Shell model plus RGM (NCSM-RGM) [23] where the basis is large enough, or FMD, which does not need to impose clustering, but in which it may arise naturally. These models are more successful in describing light nuclei than the potential cluster models, since they allow also contributions from unclustered structures and so have a more complete basis.

Nuclei in the Li-B region have been studied with cluster models for the last fifty years (see [19] and refs. therein). Clustering certainly plays a role in five of the six nuclei in this study: It has been shown that configurations $^7$Be($3/2^-$) + p and $^7$Be($1/2^-$) + p both contribute to the ground state structure of $^8$B [24], while for $^8$Li, the lowest-lying threshold is $^7$Li+n, which lies 2.032 MeV above the ground state (see Fig. 2.6). In $^9$Be the threshold for $^8$Be+n lies 1.665 MeV above the ground state and directly below the first-excited $1/2^+$, and for $^9$B the lowest-lying threshold is $^8$Be+p, which is just below the ground

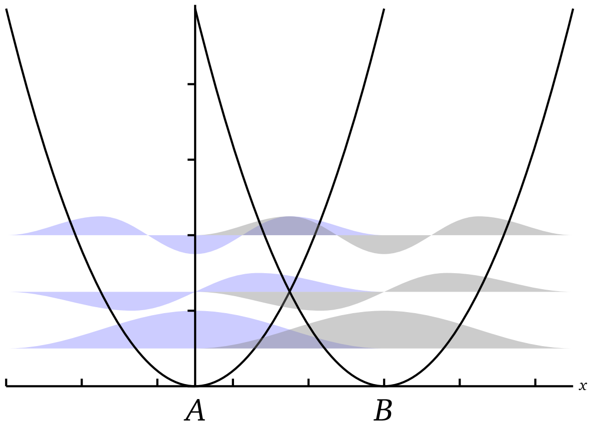

**Figure 1.2:** A two-potential-well system, such as displayed, may describe two $\alpha$ clusters. The colour-shaded areas indicate the first three single-particle eigenfunctions for each potential well. In order to describe the eigenfunctions in potential well $B$ (shown in grey) with respect to the coordinate system at the origin of potential well $A$, one would need to superpose many configurations to reproduce the displacement of the distributions off to the right.

state by 0.185 MeV. One can expect only a very small contribution of clustering in $^{10}$B, where the closest threshold to the ground-state is $\alpha$+$^{6}$Li, and lies 4.460 MeV higher in energy.

## 1.5 Haloes

A halo nucleon is properly-defined as “a nucleon which has more than fifty percent of its probability density outside the range of the core potential” [25]. This arises when one or more of the nucleons is sufficiently weakly bound to tunnel out of the potential well and into the classically forbidden region. Figure 1.3 gives a schematic illustration of a light halo nucleus, indicating the extended distribution of the halo nucleon.

Halo physics began in 1987 with the discovery and description of the 2-nucleon halo of $^{11}$Li [26]. It has certainly flourished with the advent of radioactive ion beams, with which it is possible to produce all manner of short-lived nuclei. A good review of the field of haloes since 1987 is provided by Jonson [27]. More recent ideas consider halo nuclei simply as systems with large scattering length (*e.g.* [28]). As such they share properties with all such systems.

Haloes occur predominantly in the ground states of nuclei with exotic p:n ratios, but may also occur in excited states, such as the first excited $1/2^{+}$ state of $^{17}$F, which is considered a 1-proton halo state. In order for such structures to occur, one expects first of all that the centrifugal barrier felt by the halo nucleon vanishes or is small — *i.e.* the (halo) nucleons must be in an s- or p-wave state (see Section 1.2, and *e.g.* [29]). Deformation of the nuclear core can enhance halo formation in a ground state or excited state, as it may lower the energy of s- or p-states, increasing the probability of their occupancy by a valence nucleon.

Haloes may comprise more than one nucleon. Dinucleon haloes are usually “Borromean” structures. In order to be classified as a “Borromean” system, it is required that the three-body system is bound while any pair of two of the three constituents is unbound [30]. There are also non-halo Borromean systems, like $^{9}$Be. One mechanism driving the formation of Borromean nuclei is that the magnitude of the three-body potential for the particular three bodies in question is large enough to create a bound state, but the potential arising between any of the two consitituents is weaker, such that any of the two-body systems is unbound [30]. This was first observed by L.H. Thomas in [31], in work on $^{3}$H.

Being able to model nucleon haloes theoretically is important, primarily since haloes change the reaction rates both for Coulomb dissociation and radiative capture [32].

The experimental signatures of a nucleon halo are [32]: An enhanced reaction cross-section for high-energy nuclear reactions with the nucleus in question (the greater the extent of the asymptotic part of the wave function, the greater the nuclear reaction cross-section, since it is proportional to square of interaction radius); a narrow momentum distribution of the core or "halo" nucleon following breakup (the more extended the spatial distribution, the narrower the momentum distribution), and enhanced cross-sections for Coulomb dissociation or radiative capture (a halo increases interaction radius). It is also observed that the $B(E1)$ strength at low energies is increased [29] compared to what one would predict for the nucleus without the halo nucleon(s). This occurs because the system of weakly-bound halo nucleon(s) and core makes a less-stiff oscillator than the strongly-bound nuclear system, allowing dipole excitations to occur at lower energies.

When modelling halo nuclei, the chief issue is the asymptotics of the wave function, which must decay exponentially, due to tunnelling of the halo nucleon. There are many models currently used to treat nucleon haloes: FMD, NCSM or Shell model embedded in the continuum (SMEC), to name a few.

The FMD can describe haloes well, since it allows very extended nucleon distributions with correct asymptotics, and the explicit imposition of clustering allows better reproduction of states near a threshold, improving the asymptotics of the nuclear wave function [13, 33] .

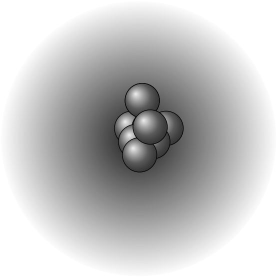

**Figure 1.3:** Artist's impression of a halo nucleus (*e.g.* $^{8}$B), showing extended distribution of the halo proton (the shaded area).

The system of $^8$Li, $^8$Be and $^8$B is very important in astrophysics, as $^8$B and $^8$Be occur in the third branch of the proton-proton chain (Fig. 2.4), which is responsible for the entire high-energy solar neutrino flux [34]. The energy-level diagram for $^8$Li, $^8$Be and $^8$B is shown in Fig. 2.1. The $T = 1$ states (indicated with a (1) in Fig. 2.1) form the $A$=8 isotriplet.

One should note in Fig. 2.1 that the thresholds for particle emission, particularly the $^7$Be+n threshold in $^8$Li and the $^7$Be+p threshold in $^8$B, are in proximity to different states (the $3^+$ and ground-state respectively), meaning that the ground states and $1^+$ states in these nuclei will have rather different asymptotic structure. This could lead to differences in the Coulomb energy in $^8$B as compared to $^8$Li for these levels, as was argued in the section on Coulomb energy (Chapter 1.3). The structure of all low-lying states in $^8$Be will have a strong 2-$\alpha$ contribution (the ground state is only 0.092 MeV above the 2-$\alpha$ threshold (Fig. 2.1)), so comparison of analogous levels in the $T = 1$ isomultiplet would certainly require a rigorous treatment of the Coulomb energy.

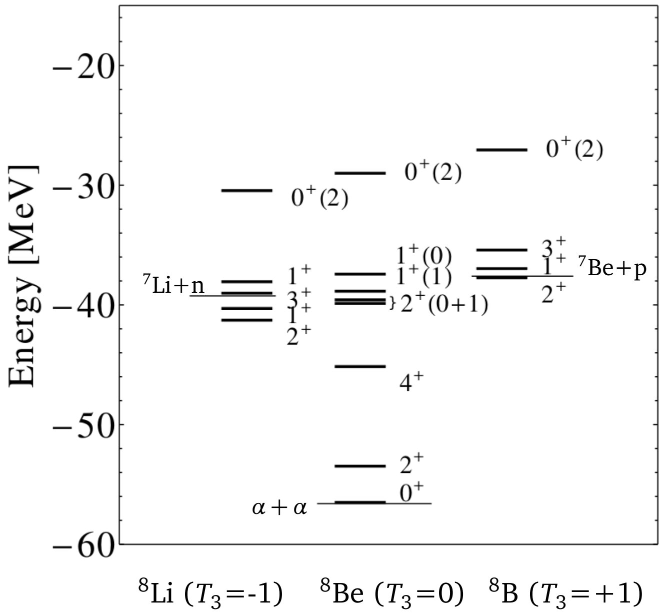

**Figure 2.1:** Level schemes for the $A$=8 isotriplet, showing levels in all three nuclei (adapted from [5]). Thin lines indicate thresholds for particle emission or breakup. Numbers in brackets denote isospin and "(0+1)" denotes a state of mixed isospin.

These three nuclei have been the subjects of many theoretical studies in the past, with approaches ranging from the Resonating Group method [35] through to No-Core Shell Model calculations [36], with the most recent work including the no-core shell model calculations of Navratil *et al.* for the whole isotriplet, halo effective field theory calculations for $^7$Li$(n,\gamma)^8$Li [6], and calculations for $^8$Be in the "tensor optimised" shell model [37]. In the next three sections, $^8$B, $^8$Be and $^8$Li are discussed in more detail, to provide some background and highlight topics of interest in all three nuclei.

## 2.1 $^8$B

### 2.1.1 General properties

Some known properties of the $^8$B ground state are given in Table 2.1. All 8 known excited states are resonances [11], and these are shown in Fig. 2.2 [5, 38]. The width of the first $1^+$ state is 35.6±0.6 keV [5].

The rms matter radius (point radius) $R_{rms}$ = 2.38(4) fm for $^8$B has been extracted from total interaction and scattering cross-sections of high-energy beams off a stable Cu target (see [39] for experimental particulars). This was done via a Glauber model analysis within the optical-limit approximation [40]. The same paper reports that al Khalili and Tostevin extended the Glauber model to include the fact that, for $^8$B and other halo nuclei, the scattering cross-section should be modelled as the scattering cross-section for the projectile scattering off the core, plus the cross section for its scattering off the halo nucleon [41]. They deduced an $R_{rms}$ of 0.2 fm larger than the one reported by [40], in this model.

The confirmation of the proton halo in the ground state of $^8$B has been mentioned in the Introduction as a *fait accompli*. However, it was at one time highly controversial, with at least one paper coming out every year in the 90's, either confirming or contradicting the idea. Studies of the $^8$B proton halo are summarised in Table 2.2. The definitive study was performed in 1999, when measurements of the longitudinal momentum distribution of $^7$Be following the breakup of $^8$B were performed [4]; confirming a proton halo. The longitudinal momentum distribution of fragments following breakup demonstrates the spatial distribution of the fragments: When a particle occupies a large spatial extension, the momentum distribution of this particle relative to the core will be narrow, due to the uncertainty principle.

**Table 2.1:** Ground state properties of $^8$B and studies where measured.

| Property | Label | | Ref. |
|---|---|---|---|
| Spin and parity | $J^\pi$ | $2^+$ | [5] |
| Isospin | $T$ | 1 | [5] |
| Lifetime | $t_{1/2}$ | 770(3) ms | [5] |
| RMS matter radius | $R_{rms}$ | 2.38(4) fm | [40] |
| Electric quadrupole moment | $Q$ | 6.83(21) efm$^2$ | [38] |
| Magnetic dipole moment | $\mu$ | 1.0355(3) $\mu_N$ | [42] |

### 2.1.2 The $S$-factor

The value of the $S$ factor $S_{17}$ for formation of $^8$B from $^7$Be + p is one of the greatest sources of uncertainty for the Standard Solar Model (SSM) (see *e.g.* [49, 50]). It seems necessary to provide some background and information on the subject, and on similar stellar nucleosynthetic reactions, as the reaction rate for $^7$Be(p,$\gamma$)$^8$B is the most important astrophysical application for $^8$B structure calculations.

The reaction rate $r_{12}$ for a charged particle-induced nonresonant nuclear reaction is given as [51]:

$$r_{12} = \frac{n_1 n_2}{1+\delta_{12}} \sqrt{\frac{8}{\pi\mu[kT]^3}} \int_0^\infty dE\, E\sigma(E) \exp\{\frac{-E}{kT}\}. \tag{2.1}$$

The subscripts "1" and "2" refer to the two particles involved in the reaction (the projectile and target). The $n_1$ and $n_2$ are the number densities of the interacting nuclei, $\mu$ is the reduced mass of the two nuclei, and $k$ is the Boltzmann constant. The value $\sigma(E)$ is the cross-section for the reaction to occur at the

**Table 2.2:** Studies on the $^{8}$B halo and their findings

| Study | Findings | Ref. | Year |
|---|---|---|---|
| Measurement of $^{8}$B quadrupole moment $Q$ using $\beta$-NMR of $^{8}$B. | $\|Q\| = 6.83 \pm 0.21$ fm$^{2}$. | [38] | 1992. |
| 3-cluster RGM (clusters $\alpha+^{3}$He+p) used to calculate $S_{17}(0)$. | Suggest that large $\|Q\|$ of $^{8}$B is a result of highly-deformed $^{7}$Be core, not a halo. | [43] | 1993. |
| Glauber model calculations to extract $^{8}$B radii from experimental interaction cross-section for proton-separation. | Conclude that the tail of the $^{8}$B wave function is significant. | [44] | 1993 |
| 3-cluster GCM calculations for $^{8}$B; using $(\alpha+^{3}\text{He})+\text{p}$ and $(\alpha+\text{p})+^{3}\text{He}$ clusters. | Find that $\|Q\|$ can be well-reproduced in their model without a proton halo. | [35] | 1994 |
| Shell model calculations in a $2\hbar\omega$ model space. | Find that $\|Q\|$ is well-reproduced in their model without a proton halo. | [45] | 1994 |
| Measurement of longitudinal momentum distribution of $^{7}$Be fragments following breakup of $^{8}$B. | Compared results to QRPA calculations; concluded a proton halo is necessary to explain the momentum distribution of $^{7}$Be fragments. | [46] | 1995. |
| Measurement of total reaction cross-section ($\sigma_R$) of $^{8}$B on natural Si at 20 - 60 Mev/nucleon. | Comparison to calculations of $\sigma_R$ shows that an extended proton density distribution is needed to reproduce $\sigma_R$. Conclude the existence of a proton halo. | [47] | 1995 |
| Glauber model calculations to extract $^{8}$B (rms) radii from interaction cross-section measurements at 790 $A$ MeV. | Conclude that longitudinal momentum distribution of $^{7}$Be can be reproduced without needing a long tail for the $^{8}$B wave function, in contradiction of the conclusions of [46]. | [48] | 1996 |
| Measurement of longitudinal momentum distributions of $^{7}$Be fragments from collision of an $^{8}$B beam on stable C and Pb targets. | A one-proton halo is deduced. | [4] | 1999 |

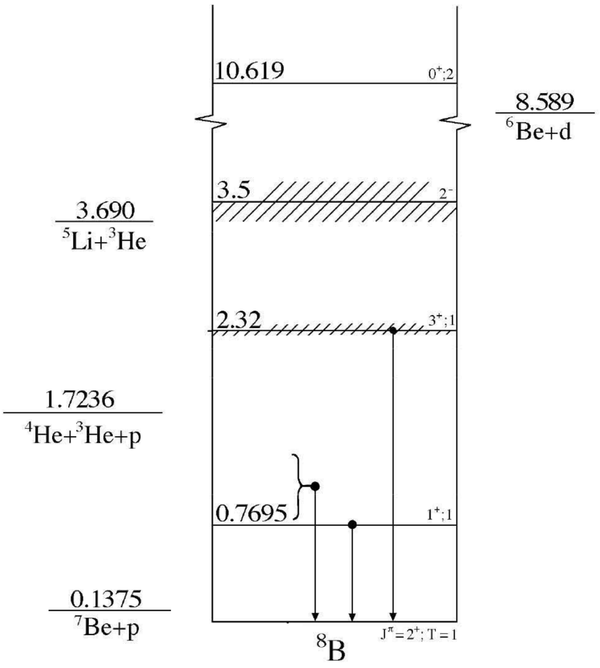

**Figure 2.2:** Level scheme of $^{8}$B (taken from [5]). Shading indicates width of the levels, and labelled lines outside of the scheme indicate thresholds and are labelled for the emitted particles. Labelling of the levels is given as $J^{\pi}; T$ to the right of each level. Brackets around a spin or isospin indicate that the value is not confirmed.

energy $E$. The Kronecker delta $\delta_{12}$ between the two species excludes double counting when both species (1 and 2) are the same.

Fusion of a projectile and target ion to form a compound nucleus is limited by the height of the Coulomb barrier between the two charged ions [52]. Relevant for stellar nucleosynthesis are fusion reactions at energies below the Coulomb barrier, which can, however, occur by tunnelling [52]. Since the cross-section for these tunnelling processes drops exponentially for small energies, one multiplies the cross-section $\sigma(E)$ with the Gamow penetration factor (the probability for the system in an s-wave to penetrate the Coulomb barrier). This is done to obtain a more slowly-varying quantity, called the $S$-factor; *i.e.* [1]:

$$S(E) = E\sigma(E)\left[e^{2\pi\eta}\right] \tag{2.2}$$

Here, $\eta$ is the Sommerfeld parameter (defined as $\eta = (Z_1 Z_2 e^2)/(\hbar v)$ where $v$ is the relative velocity between the projectile and target nuclei) [1].

Equation (2.2) gives the definition of $S(E)$ as a function of $E$, but since $S(E)$ (for nonresonant processes) varies only slowly with $E$; its value at thermal energies occuring in stars is taken to be the one at $E = 0$, which is referred to as "the $S$-factor". An $S$-factor is usually labelled in subscript for the $A$ of the nuclei involved in the reaction; so for example the $S$-factor for the reaction $^{7}$Be+p is labelled $S_{17}(0)$.

There are many experimental values of $S_{17}(0)$ supplied in the literature, dating from between 1966 and 2009 (see Table 2.3 and [53–59])). The diagram from [60], given here as Fig. 2.3, plots experimental values of $S_{17}$(E) in comparison to a prediction for $S_{17}(0)$ from NCSM-RGM calculations [60] (red line).

The existence of a proton halo in $^{8}$B is associated with an enhanced $S_{17}(0)$ (enhanced compared to what one would expect without a proton halo) [61]. This is because $S_{17}(0)$ grows with the interaction radius of $^7$Be+p [61]. If there is a proton halo in $^8$B, this means that the interaction radius of $^7$Be and p is quite large, which means that $^7$Be(p,$\gamma$)$^8$B is favoured. In a study by Csoto and Langanke [61], it was noted that "$S_{17}(0)$ decreases with decreasing $^8$B radius".

The experimental measurement of $S_{17}(0)$ is complicated, given that the target of choice, $^7$Be, is not stable. The preferred method was measuring $\beta^+$-delayed $\alpha$ particles from the break up of the $^8$Be into which $^8$B beta-decays [53]. Recently, with the introduction of radioactive ion beams, it has become possible to measure the $^7$Be(p,$\gamma$)$^8$B reaction rate directly by scattering a $^7$Be beam from a Hydrogen target; as was done by Bardayan *et al.* in 2009 [62]. The old $\beta$-delayed $\alpha$ experiments were beset with error (losses due to "sputtering", poor detector efficiency, nonuniform targets [51]), and so the pre-2001 measurements may be discounted. Of the post-2001 results, the current accepted experimental results are those of Strieder *et al.* (18.4 ± 1.6 eVb) [58] and Schümann *et al.* (20.6 ± 2.0 eVb) [59].

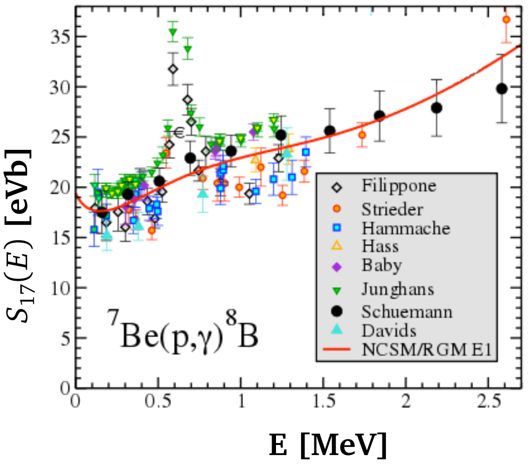

**Figure 2.3:** Values of $S_{17}(0)$ from experiment and theory, dating from 1986 to 2006. Plot from [36, 60]).

**Table 2.3:** Selected measurements of $S_{17}(0)$ and the reactions used.

| Study | Date | Reaction | $S_{17}(0)$ [eVb] | Ref. |
|---|---|---|---|---|
| Parker *et al.* | 1966 | $\beta^+$-delayed $\alpha$'s | 28.0 ± 3.0 | [53] |
| Kavanagh *et al.* | 1969 | $\beta^+$-delayed $\alpha$'s | 27.3 ± 2.4 | [54] |
| Vaughn *et al.* | 1970 | $\beta^+$-delayed $\alpha$'s | 21.4 ± 2.2 | [55] |
| Fillipone *et al.* | 1986 | $\beta^+$-delayed $\alpha$'s | 24.0 ± 2.0 | [56] |
| Motobayashi *et al.* | 1994 | $^{208}$Pb($^8$B, $^7$Be, $p$)$^{208}$Pb | 16.7 ± 3.2 | [57] |
| Strieder *et al.* | 2001 | Scattering of $^1$H from $^7$Be | 18.4 ± 1.6 | [58] |
| Bardayan *et al.* | 2009 | Scattering of $^7$Li/$^7$Be from $^1$H | 26.8 ± 6.5 | [62] |
| Schümann *et al.* | 2006 | Coulomb Dissociation<br>of $^8$B at 254$A$ MeV | 20.6±2.0 | [59] |

The theoretical value of $S_{17}(0) = 24.69$ eVb supplied in the review by Adelberger *et al.* [51] is from [63]. However, recent NCSM-RGM calculations by Navrátil give an $S$ factor of $S_{17}(0) = 19.4(7)$ eVb [36]. This new result is in agreement with the accepted experimental values [58, 59], and is possibly the most reliable theoretical value thus far.

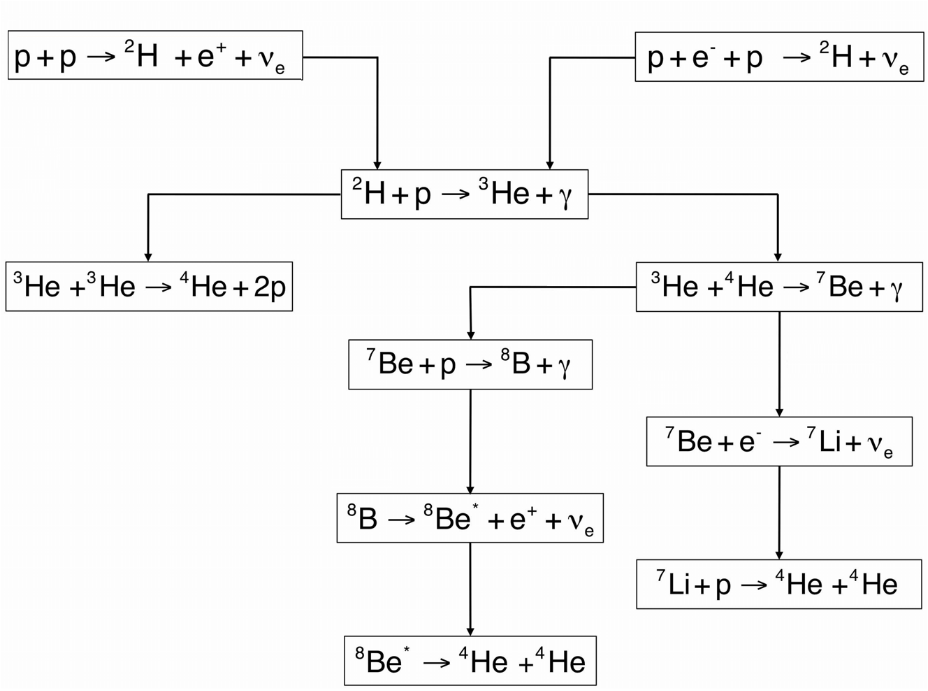

**Figure 2.4:** Schematic of the proton-proton (pp) chain of stellar nucleosynthesis, as occurs in solar-mass stars. Taken from [66].

### 2.1.3 $^8$ B and the solar neutrino problem

Since the $\beta^+$ decay of $^8$B is responsible for the high-energy solar electron-neutrino flux and $\approx 75\%$ of observable solar neutrinos [34] (see Fig 2.4, showing the proton-proton chain), much of the original work on $^8$B was done in connection to the "solar neutrino problem". The problem and its resolution (in 2001) thus feature heavily in $^8$B literature, and need a brief mention here.

The "solar neutrino problem" refers to the fact that, in the measurements of solar neutrino flux, the flux was observed to be a third of the predicted one (see [64] or [65]). This was at first thought to be due to a low $S$-factor for $^7$Be(p, $\gamma$)$^8$B, and much work on $^8$B structure was carried out to find out why $S_{17}(0)$ would be small enough to account for this low neutrino flux. The "missing flux" was later determined to be due to neutrino oscillation [65]. Now that this problem has been solved, interest in calculating the $^7$Be(p,$\gamma$)$^8$B $S$-factor continues with the hopes of reducing theoretical uncertainty in the Standard Solar Model [49, 50].

### 2.1.4 The $^8$B ground state structure and ground state spin

Since $^8$B has a $2^+$ ground state, the possible configurations for the odd proton plus $^7$Be core are [67–69]:

$$\begin{aligned}
&{}^7\mathrm{Be}(3/2^-) \otimes \mathrm{p}(3/2^-)\\
&{}^7\mathrm{Be}(3/2^-) \otimes \mathrm{p}(1/2^-)\\
&{}^7\mathrm{Be}(1/2^-) \otimes \mathrm{p}(3/2^-).
\end{aligned} \tag{2.3}$$

Which structures contribute, and with what overlap? A recent experiment by Cortina-Gil *et al.* [24] measured the total one-proton removal cross-section for relativistic $^8$B nuclei on carbon, and compared this to the cross-section for the same reaction occurring in coincidence with a 429 kev $\gamma$-ray (this latter cross-section occurs when $^7$Be is in its first excited state, which decays via this transition). The ratio of the two cross-sections was determined as 13±3%, from which it was concluded that overlap of the $^7\mathrm{Be}(1/2^-) \otimes \mathrm{p}(3/2^-)$ state with the $^8$B ground-state is 13±3% [24]. The configurations $^7\mathrm{Be}(3/2^-) \otimes \mathrm{p}(1/2^-)$ and $^7\mathrm{Be}(1/2^-) \otimes \mathrm{p}(3/2^-)$ are thus both significant in the $^8$B ground state.

How the ground state spin $J = 2$ comes about is worth consideration. In a naïve shell-model picture, with three protons and one neutron in the p(3/2) orbitals, one would expect any integer ground state spin $J$ from 3 to 0. The Nilsson model can be used to give a heuristic argument for the ground state of $^8$B having $J^\pi = 2^+$. In the Nilsson model, in the case of deformed odd-odd nuclei, the ground state spin is given by the Gallagher-Moszkowski rule [70]:

$$\begin{aligned} J &= \Omega_p + \Omega_n \quad \text{if } \Omega_p = \Lambda_p \pm \tfrac{1}{2} \text{ and } \Omega_n = \Lambda_n \pm \tfrac{1}{2}, \\ J &= |\Omega_p - \Omega_n| \quad \text{if } \Omega_p = \Lambda_p \pm \tfrac{1}{2} \text{ and } \Omega_n = \Lambda_n \mp \tfrac{1}{2}, \end{aligned} \tag{2.4}$$

where the Nilsson quantum numbers $\Omega$, $N, n_3$ and $\Lambda$ are defined in Appendix 1 and the Nilsson orbitals are labelled as $[N, n_3, \Lambda, \Omega]$. If the deformation parameter $\beta$ for the $^7$Be core of $^8$B lies anywhere between $\beta$ = -0.6 and $\beta$ = 0 (studies exist which suggest an oblate-deformed $^7$Be [71, 72], even though its deformation parameter is not well-known), then the odd proton in $^8$B is in Nilsson orbital [110 1/2] and the odd neutron is in Nilsson orbital [101 3/2](see Fig. 2.5). This gives the first case of the Gallagher-Moszkowski rule (Eq.(2.4)), and thus gives a $J$ of $\Omega_p + \Omega_n$ = 1/2 + 3/2 = 2.

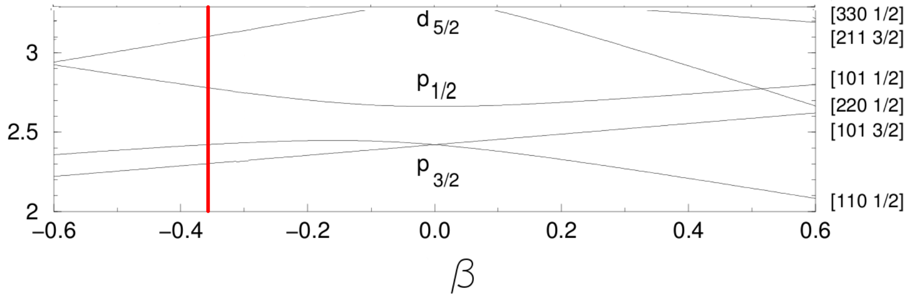

**Figure 2.5:** Nilsson diagram for highly-deformed light nuclei [73]. The vertical line is at $\beta$ = -0.35; the deformation of the $^7$Be core of $^8$B. The labels for the Nilsson orbitals are provided on the right. Note the arrangement of the [110 1/2] and [101 3/2] orbitals at the deformation of $-0.6 < \beta < 0$.

### 2.2.1 General Properties

The nucleus $^{8}$Li has a lifetime of 839±9 ms, and $\beta^{-}$ decays to the first $2^{+}$ state of $^{8}$Be. Many of its ground state properties have been measured, and these are provided in Table 2.4. The known energy levels are provided in Figure 2.6. The excited states are also resonances, with the first $1^{+}$ state being extremely broad, (a lifetime of 12±4 fs), and the $3^{+}$ state having a width of 33±6 keV [5].

The rms point matter radius of $^{8}$Li is 2.37(2) fm [40]. The electric quadrupole moment has been measured as 3.27(6) efm$^{2}$ [5]. This quadrupole deformation likely arises from strong contribution of a cluster structure $^{4}$He+$^{3}$H+n, to the ground state, as suggested by [74].

**Table 2.4:** Ground state properties of $^{8}$Li and studies where measured.

| Property | Label | | Ref. |
|---|---|---|---|
| Spin and parity | $J^{\pi}$ | $2^{+}$ | [5] |
| Isospin | $T$ | 1 | [5] |
| Lifetime | $t_{1/2}$ | 839.9±9 ms | [5] |
| RMS matter radius (point) | $R_{rms}$ | 2.37(2) | [40] |
| Charge radius | $R_{ch}$ | 2.29(8) fm | [75] |
| Quadrupole moment | $Q$ | 3.27(6) efm$^{2}$ | [5] |
| Magnetic dipole moment | $\mu$ | 1.653560(18) $\mu_N$ | [5] |

The radiative capture $^{7}$Li(n,$\gamma$)$^{8}$Li is the first reaction in the chain $^{7}$Li(n,$\gamma$)$^{8}$Li($^{4}$He,n)$^{11}$B(n,$\gamma$)$^{12}$B($\beta$)$^{12}$C that can connect Hydrogen burning to the Carbon cycle (see [76] and refs. therein). The rate of the reaction $^{7}$Li(n,$\gamma$)$^{8}$Li (and the predicted yield of $^{8}$Li) was thus important information when considering inhomogeneous models of the Big Bang: This chain is the entry point to nucleosynthesis of heavier elements in inhomogeneous big-bang models [76]. Inhomogeneous models are, however, currently disfavoured, because they were found to overproduce several light nuclides (see *e.g.* [6] and refs. therein).

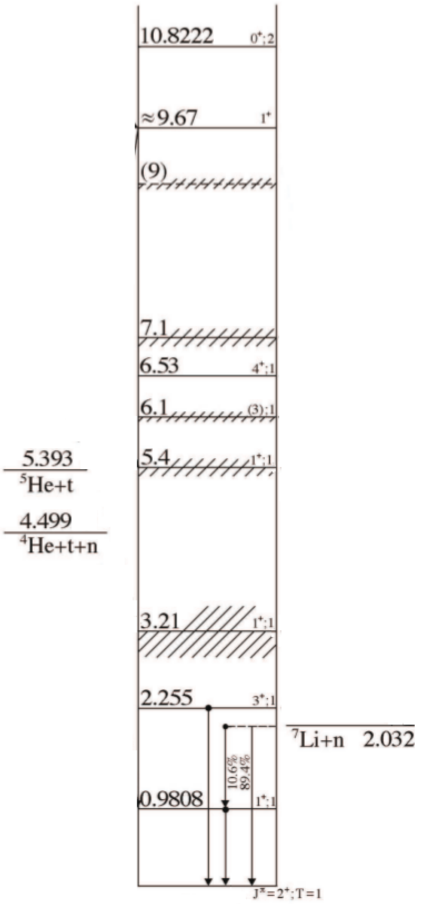

**Figure 2.6:** The $^8$Li level-scheme (taken from [5]). Notation as in Figure 2.2.

## 2.3 $^8$Be

### 2.3.1 General Properties

The ground state of $^8$Be is a two-alpha resonance of width $\Gamma$=5.57±0.25 eV. Only a few of the properties of the $^8$Be ground state have been measured, and these are provided in Table 2.5. The known energy levels are provided in Figure 2.7. These too are resonances, with the first $2^+$ state rather broad (width 1513(15) keV), and the $4^+$ state even broader (width ≈3500 keV) [5]. Of the higher-lying states, the $T$=1 $1^+$ state at 17.640 MeV has width 10.7±0.5 keV [5].

Astrophysically, modelling the structure of $^8$Be is as important as modelling $^8$B for determining solar core temperature from solar neutrino flux, since $^8$B $\beta$-decays to $^8$Be+p, emitting high-energy solar neutrinos.

**Table 2.5:** Ground state properties of $^8$Be and studies where measured.

| Property | Label | | Ref. |
|---|---|---|---|
| Spin and parity | $J^\pi$ | $0^+$ | [5] |
| Isospin | $T$ | 0 | [5] |
| Lifetime | $t_{1/2}$ | 3.71x$10^{-16}$s | [5] |

### 2.3.2 The $T$=1 states

The nucleus $^8$Be has the intriguing property that the low-lying states are alpha-clustering states, since the 2-$\alpha$ threshold is 92 keV below the ground-state (see Fig 2.7). The higher-lying states ($T$=1 states), have a more shell-model like structure, as the $\alpha$ clusters must have been “broken” in order for $T$=1 states to form.

This nucleus is thus quite a challenge to model, since not only do both clustering and shell-model type states appear; they also “switch places” compared to most nuclei, which tend to have shell-model type ground-states with cluster structure forming at higher energies near the particle emission thresholds. The occurrence of both shell-like states and $\alpha$-cluster states in $^8$Be has been discussed by Myo *et al.* [37] in a 2014 paper, in which they discuss the role of the tensor force in the production of these states. Reproduction of these higher-lying levels is a test of a model’s ability to reproduce both clustering and shell-model states consistently.

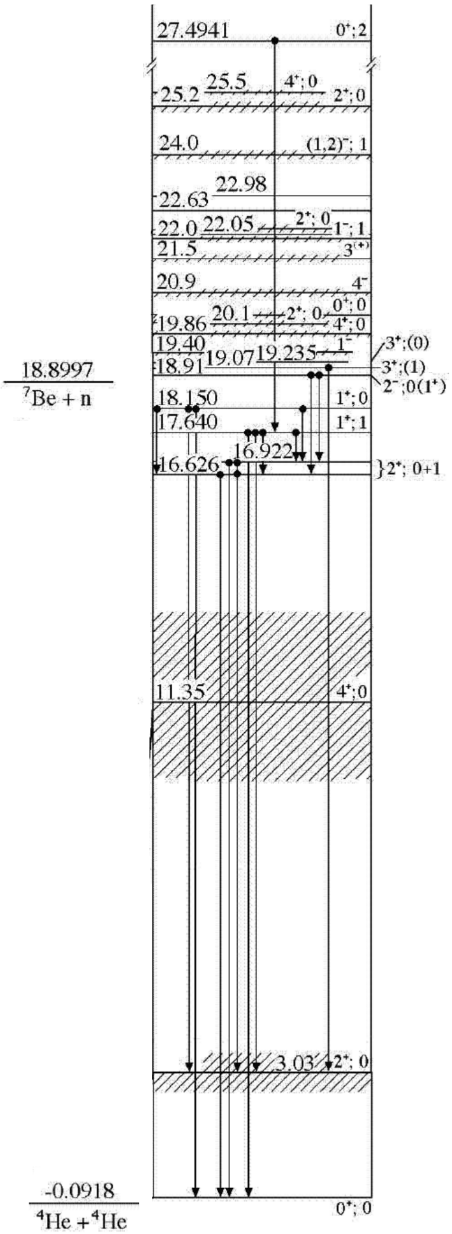

**Figure 2.7:** The $^{8}$Be level-scheme (taken from [5]). Notation as in Figure 2.2.

The $A$=9 isodoublet is of interest primarily because of the “missing” $1/2^+$ state in $^9$B compared to $^9$Be, and for the fact that $^9$B is unbound while $^9$Be is stable (Fig. 3.1). This latter makes these mirror nuclei a good candidate for the Thomas-Ehrman shift, since every state in $^9$B is unbound with respect to the threshold for proton emission.

It is interesting to note that the “missing” $1/2^+$ state is close to the threshold for breakup into $^8$Be+n in $^9$Be, but if it lies at this energy in $^9$B, it is close to the threshold for $^5$Li+$\alpha$ in $^9$B (Fig. 3.1, Figs. 3.2 and 3.3). The fact that the purported $1/2^+$ state in $^9$B has so far not been characterised is because it is very short-lived (the lifetime has not been measured either, but it lies within a few tens of keV below the $^5$Li+$\alpha$ threshold [5]). The paper by Sherr and Bertsch [77] details most of the investigations around the $1/2^+$ state.

Other interest in the $A$=9 isodoublet is the astrophysical role of $^9$Be, both as part of an alternative pathway for $^{12}$C production, and as a stable nucleus produced by spallation of cosmic rays on heavy nuclei. This means that $^9$Be is a “stable witness” to all events involving heavy nuclei and cosmic rays, such as the birth of galaxies, and its abundance can tell us about the regularity of such events, provided that we know the relevant reaction rates [78].

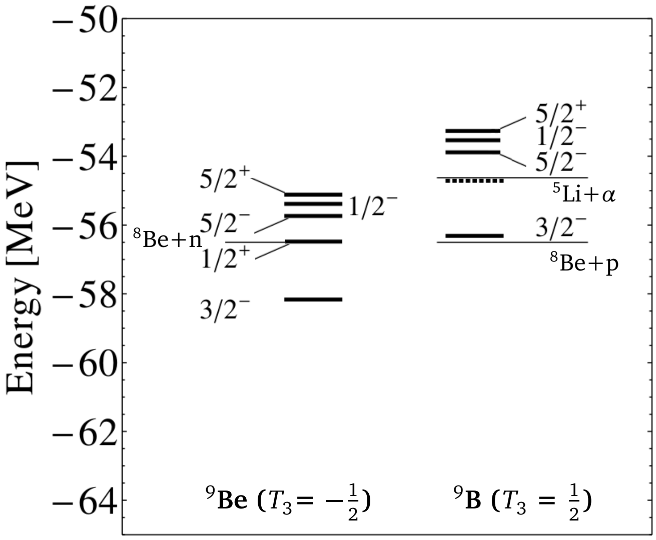

**Figure 3.1:** The level schemes of the $A$=9 isodoublet (adapted from [5]). The dot-dashed line in the level-scheme for $^9$B indicates the level of unknown spin and parity that is thought to be the missing $1/2^+$ state. Thin lines indicate thresholds for particle emission (labelled for the emitted particles).

## 3.1 $^{9}$Be

### 3.1.1 General properties

The nuclei $^{9}$Be and $^{10}$B are the only stable nuclei in this thesis. The ground-state properties of $^{9}$Be are provided in Table 3.1, and a level-scheme is provided as Fig. 3.2. Note that the threshold for $^{8}$Be+n lies only 19 keV below the first excited $1/2^{+}$ state, suggesting that $^{8}$Be+n clustering configurations will contribute strongly to the structure of this state. The width of this resonance is 217±10 keV [5]. The $5/2^{-}$ state is much narrower, with width 0.78±0.13 keV [5].

The astrophysical importance of $^{9}$Be lies in the reactions $^{8}$Be(n,$\gamma$)$^{9}$Be($\alpha$,n)$^{12}$C, which provide an alternative to the triple-alpha process for the formation of $^{12}$C. This chain of reactions occurs in explosive nucleosynthesis, such as in core-collapse supernovae, so knowing the reaction rate for $^{8}$Be(n,$\gamma$)$^{9}$Be would be useful to understanding the percentage of explosive nucleosynthesis producing $^{12}$C [79].

**Table 3.1:** Ground state properties of $^{9}$Be and studies where measured.

| Property | | | Ref. |
|---|---|---|---|
| Spin and parity | $J^{\pi}$ | $3/2^{-}$ | [5] |
| Isospin | $T$ | 1/2 | [5] |
| Lifetime | $t_{1/2}$ | stable | [5] |
| RMS matter radius (point) | $R_{rms}$ | 2.38(1) fm | [40] |
| Charge radius | $R_{c}$ | 2.519(12) fm | [80] |
| Quadrupole moment | $Q$ | 5.288(38) efm$^{2}$ | [5] |
| Magnetic dipole moment | $\mu$ | -1.1778(9) $\mu_N$ | [5] |

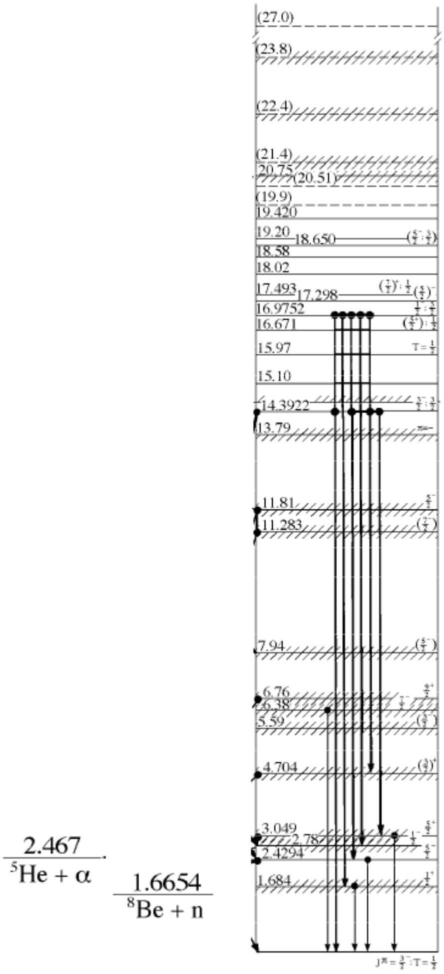

**Figure 3.2:** Measured $^9$Be level-scheme (taken from [5]). Notation as in Figure 2.2.

## 3.2 $^{9}$B

### 3.2.1 General Properties

The nucleus $^{9}$B exists only as a three-body resonance with a width of 0.54(21) keV [5], which corresponds to a lifetime of $8(3)\times10^{-10}$ ns. The $^{8}$Be+p threshold lies 0.184 MeV below the $^{9}$B ground-state. Known ground-state properties are listed in Table 3.2. A level-scheme is provided as Fig. 3.3. The width for the candidate $1/2^{+}$ state at 1.6 MeV is not known, and the width for the lowest $5/2^{-}$ state is 81±5 keV [5].

Another important threshold in $^{9}$B is $^{5}$Li$+\alpha$, which lies at 1.689 MeV above the ground-state. The candidate $1/2^{+}$ state at $\approx$ 1.6 MeV is close to this energy. One can expect that $^{5}$Li$+\alpha$ clustering configurations would play a role in the asymptotics of this state.

### 3.2.2 The $1/2^{+}$ state

When comparing the $^{9}$Be and $^{9}$B level schemes, we can conclude that there should occur a $1/2^{+}$ in $^{9}$B state at approximately 1.6 MeV above the ground-state. In [5], which is the most recent compilation of data on $^{9}$B, this state had not yet been observed, although they do list a state of unknown spin and parity at $\approx$ 1.6 MeV. The assignment of spin and parity to this state has not as yet been carried out conclusively because the width of this level is greater than 400 keV [77], meaning that it is too short-lived for any properties thereof to be determined. Even the energy of this state is not well known, with values ranging from 1.2 to 1.7 MeV experimentally [77], and theoretical predictions ranging from $\approx$ 0.9 MeV to $\approx$ 1.6 MeV [77,81]. A prediction of energy and width of a $1/2^{+}$ resonance in $^{9}$B in a realistic model would thus be valuable.

**Table 3.2:** Ground state properties of $^{9}$B and studies where measured.

| Property | | | Ref. |
|---|---|---|---|
| Spin and parity | $J^{\pi}$ | $3/2^{-}$ | [5] |
| Isospin | $T$ | 1/2 | [5] |
| Lifetime | $t_{1/2}$ | $8(3)\times10^{-10}$ ns | [5] |

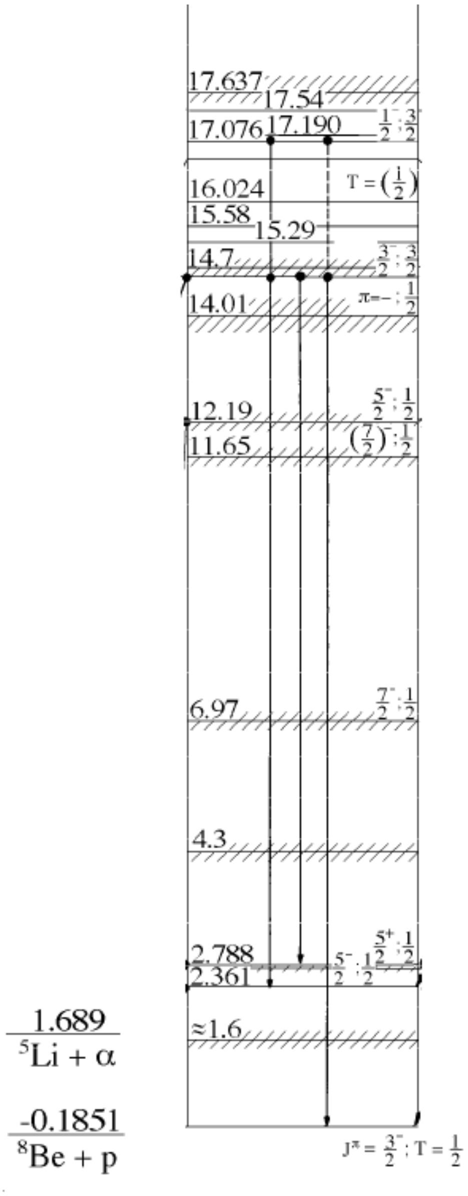

**Figure 3.3:** Measured $^9$B level-scheme (taken from [5]). Notation as in Figure 2.2.

The nucleus $^{10}$B is stable, with the ground-state properties provided in Table 4.1. The $^{10}$B level scheme is provided as Fig. 4.1. The first excited $1^+$ state is very broad, with a lifetime of 1.020±0.005 ns. The first $0^+$ state is even broader, with a lifetime of 7±3 fs [5]. The lowest-lying threshold for decay by particle emission is $^6$Li+$\alpha$, at 4.460 MeV above the ground state. Clustering configurations are thus unlikely to play a major role in $^{10}$B ground state structure.

$^{10}$B is thought to be well-described in a $1\hbar\omega$ shell model description, as all $T=0$ levels up to 7 MeV were found to be well-reproduced in such a shell-model calculation with a phenomenological potential by Van Hees and Glaudemans [82]. Cluster approaches do exist, with a $2\alpha$+d description having been done in the framework of the "three-cluster orthogonality condition model (OCM)" (a version of the Resonating Group Method) [83].

Like $^9$Be, $^{10}$B is formed in spallation of interstellar protons and heavy nuclei, and therefore it also plays the role of a "stable witness" to events like the birth of galaxies. Its abundance is thus also an indicator of the regularity of these events, if we know the reaction rates for its production and decay [78].

**Table 4.1:** Ground state properties of $^{10}$B and studies where measured.

| Property | | | Ref. |
|---|---|---|---|
| Spin and parity | $J^\pi$ | $3^+$ | [5] |
| Isospin | $T$ | 0 | [5] |
| Lifetime | $t_{1/2}$ | stable | [5] |
| RMS matter radius (point) | $R_{rms}$ | 2.20(6) fm | [40] |
| Quadrupole moment | $Q$ | 8.472(56) efm$^2$ | [5] |
| Magnetic dipole moment | $\mu$ | 1.80064475(57) $\mu_N$ | [5] |

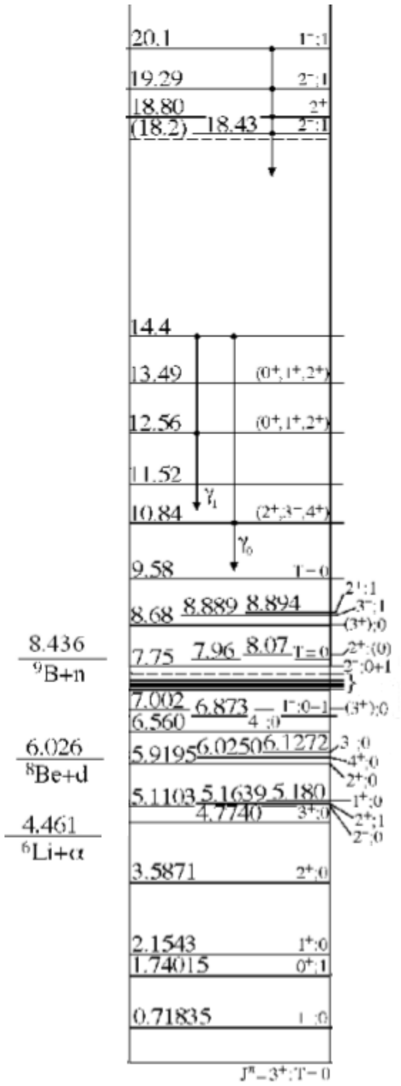

**Figure 4.1:** Measured $^{10}$B level-scheme (taken from [5]). Notation as in Figure 2.2.

# 5 Fermionic Molecular Dynamics

## 5.1 History and context

Fermionic Molecular Dynamics (FMD) [12] is a microscopic nuclear model, which was originally developed as a quantum dynamical model for heavy-ion collisions. Later, it was successfully applied to low-lying states of nuclei and low-energy nuclear reactions by invoking configuration-mixing.

The many successes of FMD arise mainly from the fact that it can build a Hilbert space capable of incorporating a wide range of nuclear behaviours [33]. Among the highlights of the model were describing the structure of the $^{12}$C Hoyle state [14], and the calculation of $^3\mathrm{He}(\alpha,\gamma)^7\mathrm{Be}$ and $^3\mathrm{H}(\alpha,\gamma)^7\mathrm{Li}$ capture cross sections [84].

## 5.2 Method

Overviews of the model are in [12, 13, 85–87]. A summary is provided here.

Starting with protons and neutrons as basic constituents of a nuclear system, we choose intrinsic many-body configurations $|Q\rangle$ that are Slater determinants of single-particle states $|q\rangle$, or [85]:

$$|Q\rangle = \hat{\mathscr{A}}\left\{|q_1\rangle \otimes \ldots \otimes |q_A\rangle\right\} \tag{5.1}$$

where $\hat{\mathscr{A}}$ is the antisymmetrisation operator and $Q = \{q_1, ..., q_A\}$ denotes the set of single-particle parameters. The single-particle states corresponding to the protons and neutrons are:

$$|q\rangle = \sum_i |a_i, \vec{b}_i\rangle \otimes |\chi_i^{\uparrow}, \chi_i^{\downarrow}\rangle \otimes |\xi\rangle c_i, \tag{5.2}$$

where a superposition of wave-packets $|a_i, \vec{b}_i\rangle$ in the spatial part can be used to describe extended distributions (*e.g.* haloes). Complex parameters $\vec{b}$ relate to the mean position and mean momentum of the wave-packets and complex parameters $a$ to the width of the wave-packets [86]. The ket $|\chi^{\uparrow}, \chi^{\downarrow}\rangle$ is the most general spinor, allowing all possible orientations of the nucleon spin. The isospin part $|\xi\rangle$ defines whether the particle is a proton or neutron, and no superpositions of the two are allowed.

In co-ordinate space one has:

$$\langle \vec{x}|a, \vec{b}\rangle = \exp\left\{-\frac{(\vec{x}-\vec{b})^2}{2a}\right\}. \tag{5.3}$$

The FMD basis is general-enough to describe both shell-model like many-body states as well as clustering states [13]. This is shown in the following diagram (Figure 5.1), which illustrates how shell-model like single-nucleon wave functions can be obtained from Gaussian wave functions.
Slater determinants $|Q\rangle$ like that in Eq.(5.1) are in general not eigenstates of the angular momentum or parity operators, so these need to be projected out. The Hamiltonian commutes with the angular momentum and parity operators, so should share eigenstates with the angular momentum and parity operators. The projection operators are given by [86]:

$$\hat{P}^{\pi} = \frac{1}{2}(1 + \pi\hat{\Pi}) \tag{5.4a}$$

$$\hat{P}^{J}_{MK} = \frac{2J+1}{8\pi^2}\int d\Omega\, D^{J}_{MK}(\Omega)^{*}\hat{R}(\Omega), \tag{5.4b}$$

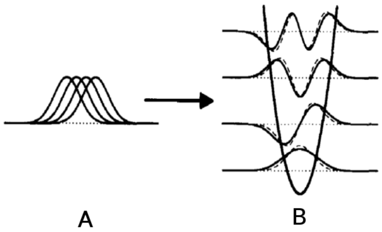

**Figure 5.1:** Illustration of how shell-model states may be obtained from Gaussian states. Antisymmetrisation of the four Gaussians in (A) leads to the four states indicated with unbroken lines in the potential well in (B). The dashed lines in (B) indicate the exact eigenstates of the oscillator. Figure from [87].

where $D^J_{MK}(\alpha,\beta,\gamma)$ is the Wigner $D$-matrix, $\hat{R}(\alpha,\beta,\gamma) = e^{-i\alpha\hat{J}_z}e^{-i\beta\hat{J}_y}e^{-i\gamma\hat{J}_z}$ is the rotation operator and $\hat{\Pi}$ is the parity operator. The $\Omega = \{\alpha,\beta,\gamma\}$ symbolises the three Euler angles. The action of the projection operators $\hat{P}^\pi$ and $\hat{P}^J_{MK}$ is to project states $|Q;J^\pi MK\rangle$ from intrinsic states $|Q\rangle$ by superimposing rotated Slater determinants with the amplitudes $D^J_{MK}(\Omega)^*$ which are constructed such that the result is a many-body state with quantum numbers $J,K,M$. There may be $2J+1$ different $K$ states for every state of good $J$, depending on the symmetries of the intrinsic state. By diagonalising the Hamiltonian in the set of $K$-projected states, we obtain the basis states

$$|Q;J^\pi M\alpha\rangle = \sum_K |Q;J^\pi MK\rangle c_K^{J^\pi\alpha}. \tag{5.5}$$

The angular momentum projection operator $\hat{P}^J_{MK}$ is not a true projection operator in that, instead of the property $\hat{P}^\dagger\hat{P} = \hat{P}$, it has the property $(\hat{P}^J_{MK})^\dagger\hat{P}^J_{M'K'} = \delta_{M,M'}\hat{P}^J_{KK'}$. The fact that $\hat{P}^J_{MK}$ commutes with the (rotationally-invariant) Hamiltonian means that one only needs to apply $\hat{P}^J_{MK}$ to the ket, and needs not act with both $(\hat{P}^J_{MK})^\dagger$ and $\hat{P}^J_{MK}$ in a matrix element. The action of $\hat{P}^J_{MK}$ on a Slater determinant intrinsic state is to rotate each single-particle state through some angles $\Omega$ by rotating the parameters $\vec{b}$ and the spinor $|\chi^\uparrow\chi^\downarrow\rangle$ of each single-particle wave-packet and to superimpose these rotated determinants with amplitudes $D^J_{MK}(\alpha,\beta,\gamma)$ for a particular overall angular momentum.

Integration over $\Omega$ as in Eq.(5.4b) is done by discretising and summing over a grid of angles $\alpha,\beta$ and $\gamma$. The number of grid points sensible for use with a given nucleus is dictated by how deformed that nucleus is: *i.e.* typically one uses 20 grid points for $\beta$ and 10 each for $\alpha$ and $\gamma$ [86], though one may use less if the nucleus is only slightly deformed. One needs only to sum over $\beta$ when a nucleus is axially-symmetric about the $z$-axis, because $\hat{R}(\Omega)$ acting on the state reduces to a rotation through $\beta$ in this case, and gives only phases for $\alpha$ and $\gamma$.

The first step to obtain an approximation to the nuclear ground state is to invoke Ritz's variational principle and minimise the energy by varying $Q = \{q_1,...,q_A\}$ which describe the intrinsic basis states $|Q\rangle$, or:

$$\min_{\{Q\}} \frac{\langle Q|\hat{H} - \hat{T}_{cm}|Q\rangle}{\langle Q|Q\rangle}. \tag{5.6}$$

$\hat{T}_{cm}$, the operator for the centre-of-mass kinetic energy, is subtracted to reduce the influence of the spurious centre-of-mass energy inherent in a Slater determinant. After that, one projects out states with spin-parity $J^\pi$. This is called Projection after Variation (PAV), as the variational principle is applied and then projection operators act on the minimised state.

An improved state, increasing the numerical effort only by a factor of two, is obtained by projecting first on parity, with the help of Eq.(5.4a), *i.e.*

$$|Q;\pi\rangle = \frac{1}{2}(1+\pi\hat{\Pi})|Q\rangle \ ; \quad \pi = \pm 1, \tag{5.7}$$

and then minimise

$$\frac{\langle Q;\pi|\hat{H}-\hat{T}_{cm}|Q;\pi\rangle}{\langle Q;\pi|Q;\pi\rangle} = \frac{\langle Q|\hat{H}-\hat{T}_{cm}|Q\rangle + \pi\langle Q|\left(\hat{H}-\hat{T}_{cm}\right)\hat{\Pi}|Q\rangle}{\langle Q|Q\rangle + \pi\langle Q|\hat{\Pi}|Q\rangle} \tag{5.8}$$

with respect to $Q$. As $\hat{H}$ and $\hat{T}_{cm}$ commute with the parity operation $\hat{\Pi}$ and $\hat{\Pi}|Q\rangle$ is again an FMD state with the parity operation acting on each single-particle state $|q_i\rangle$, the additional effort is to calculate one more many-body matrix element and overlap. After minimisation one again projects on total spin $J$.

The best results are however obtained by doing a so-called VAP (Variation After Projection) minimisation

$$\underset{\{Q;c\}}{\min} \quad \frac{\langle Q;J^\pi M\alpha|\hat{H}-\hat{T}_{cm}|Q;J^\pi M\alpha\rangle}{\langle Q;J^\pi M\alpha|Q;J^\pi M\alpha\rangle}, \tag{5.9}$$

where the parameters $Q$ and the coefficients $c_k^{J^\pi\alpha}$ of the $K$-mixed state given in Eq.(5.5) are minimised simultaneously.

These VAP states $|Q;J^\pi M\alpha\rangle$ provide a good first approximation for the description of the nucleus. To improve the description, additional basis states can be generated by performing minimisation (Eq.(5.8)) subject to constraints. These constraints could be on *e.g.* radii, moments or deformation parameters [13].

What to constrain may seem fairly arbitrary, as one may arrive at one property by constraining the other (*e.g.* configurations with large radius may also have large electromagnetic moments, say). It can be chosen according to what is known experimentally: if the nucleus is known to have a large radius, constraints on the matter radius seem a good first choice; if it is known to be deformed, one might instead constrain the matter or electric quadrupole moments. The joy of the current status of FMD, in which one has many constraints to choose from, is that one can make quite extensive basis sets simply by choosing several constraints. This gives a slightly-reduced likelihood of creating overcomplete basis sets, since it could be that different constraints generate a different set of configurations. The Hamiltonian may then be diagonalised in this basis of constrained states, and the eigenstate energies may be compared to experiment. The diagonalisation process is discussed in Section 5.3.

Minimisation subject to constraints is implemented numerically using a sequential quadratic programming method based on that developed by [88]. This is discussed further in Appendix 2.

## 5.3 Diagonalising the Hamiltonian

In FMD, one diagonalises the Hamiltonian in the set of many-body basis states $|Q;J^\pi M\alpha\rangle$ ($\alpha$ stands in for quantum numbers besides spin and parity), to obtain the eigenstates and eigenenergies for the nucleus.

This set of basis states, which are generated by the methods discussed in the previous sections, may or may not be over-complete: that is, a set of twenty such basis states, say, may actually only represent a fifteen-dimensional Hilbert space. This means there will only be information enough to generate fifteen different eigenstates of the Hamiltonian, although our Hamiltonian matrix will be twenty-by-twenty. Thus, we will unavoidably generate some linearly-dependent eigenstates when we diagonalise the Hamiltonian in this space, simply because we do not know how “over-complete” our basis set is. To overcome this problem one applies the Singular Value Decomposition (see also [13, 89]).

The solution of the eigenvalue problem

$$\hat{H}|\Psi\rangle = E|\Psi\rangle \tag{5.10}$$

boils down to finding the coefficients $c_k^\alpha$ of the configurations $|Q_k; J^\pi M\alpha\rangle$

$$|\Psi\rangle = \sum_{k,\alpha} |Q_k; J^\pi M\alpha\rangle c_k^\alpha \tag{5.11}$$

$$\hat{H}|\Psi\rangle = E|\Psi\rangle, \tag{5.12}$$

where $|\Psi\rangle$ are the eigenstates for $\hat{H}$, which are generally superpositions of basis states $|Q; J^\pi M\alpha\rangle$ and $Q$ stands for the intrinsic state.

With the expansion of $|\Psi\rangle$ in Eq.(5.11), one can write the eigenvalue equation (Eq.(5.12)) in the form:

$$\sum_{k,\alpha} \hat{H}|Q_k; J^\pi M\alpha\rangle c_k^\alpha = E \sum_{k,\alpha} |Q_k; J^\pi M\alpha\rangle c_k^\alpha. \tag{5.13}$$

For implementation on the computer, one requires matrices. For this reason one multiplies both sides of Eq.(5.13) with a bra $\langle Q_{k'}; J^\pi M\alpha'|$ to obtain the form:

$$\sum_{k,\alpha} \langle Q_{k'}; J^\pi M\alpha'|\hat{H}|Q_k; J^\pi M\alpha\rangle c_k^\alpha = E \sum_{k,\alpha} \langle Q_{k'}; J^\pi M\alpha'|Q_k; J^\pi M\alpha\rangle c_k^\alpha. \tag{5.14}$$

This can be written more compactly as:

$$\mathbf{H}c = E\mathbf{N}c, \tag{5.15}$$

where the bold-face letters represent matrices

$$\mathbf{H} = \left\{\langle Q_{k'}; J^\pi M\alpha'|\hat{H}|Q_k; J^\pi M\alpha\rangle\right\}$$
$$\mathbf{N} = \left\{\langle Q_{k'}; J^\pi M\alpha'|Q_k; J^\pi M\alpha\rangle\right\}$$

In the case that the matrix **N** is invertible, one may multiply both sides by $\mathbf{N}^{-1/2}$, which gives:

$$\mathbf{N}^{-1/2}\mathbf{H}c = E\mathbf{N}^{-1/2}\mathbf{N}c = E\mathbf{N}^{1/2}c. \tag{5.16}$$

When one inserts on the left-hand side the term $\mathbf{N}^{-1/2}\mathbf{N}^{1/2}$ one obtains

$$\mathbf{N}^{-1/2}\mathbf{H}\mathbf{N}^{-1/2}\mathbf{N}^{1/2}c = E\mathbf{N}^{1/2}c. \tag{5.17}$$

The term $\mathbf{N}^{-1/2}\mathbf{H}\mathbf{N}^{-1/2}$ may be written as $\tilde{\mathbf{H}}$, and $\mathbf{N}^{1/2}c$ may be written as $\tilde{c}$, which gives:

$$\tilde{\mathbf{H}}\tilde{c} = E\tilde{c}. \tag{5.18}$$

Eq.(5.18) can be solved for the coefficients $c$, which allows one to determine the eigenvectors $|\Psi\rangle$ via Eq.(5.11).

There is still an inherent problem: this method works only if **N** (the matrix of overlaps of the projected states $|Q_k; JM\alpha\rangle$ can be inverted. So in order to implement this diagonalisation, one needs to ensure that the matrix **N** is invertible.

In the Singular Value Decomposition (SVD), the matrix **N** can be written as [89]:

$$\mathbf{N} = \mathbf{U} \cdot \mathbf{D} \cdot \mathbf{V}^\dagger \tag{5.19}$$

where **U** and **V** are unitary matrices containing the eigenvectors of **N**, and **D** contains the eigenvalues of **N**. Thus, $\mathbf{N}^{-1}$ can be written as:

$$\mathbf{N}^{-1} = \mathbf{U}^\dagger \cdot \mathbf{D}^{-1}\mathbf{V}, \tag{5.20}$$

The idea is that one may select to replace eigenvalues in $\mathbf{D}^{-1}$ which are very large, let us say larger than some value $\eta^{-1}$, by zero.

This same process, *i.e.* solving the eigenvalue equation (Eq.(5.12)) in the small subspace of states spanned by $|Q_k; J^\pi MK\rangle$ for each $k$, is used to create states of good $J$ and $M$ that are eigenstates of the Hamiltonian, since [13]:

$$\sum_{K'} \mathbf{H}^{J^\pi}_{K,K'} C^{J^\pi\alpha}_{K'} = E^{J^\pi\alpha} \sum_{K'} \mathbf{N}^{J^\pi}_{K,K'} C^{J^\pi\alpha}_{K'} \tag{5.21}$$

This removes possible linear dependence among $|Q_k; J^\pi MK\rangle$, and is referred to as $K$-mixing. One uses then only states $|Q_k; J^\pi M\alpha\rangle = \sum_{K'} |Q_k; J^\pi MK'\rangle C^{J^\pi\alpha}_{K'}$ as basis states for the lowest energies $E^{J^\pi\alpha}$.

## 5.4 Cluster configurations

One may create basis states in which one explicitly imposes that the nucleus is composed of clusters. In principle, one could implement this using 2 or 3 clusters. For ease of writing, the discussion below will focus on the two-cluster situation.

The “cluster” configurations $|Q_{c1+c2}\rangle$ are expressed as antisymmetrised products of the configurations $|Q_{ci}\rangle$ describing each cluster, or [33]:

$$|Q_{c1+c2}\rangle = \hat{\mathscr{A}} \left\{ |Q_{c1}\rangle \otimes |Q_{c2}\rangle \right\}. \tag{5.22}$$

The FMD representation allows the placement of cluster $|Q_{c2}\rangle$ ar a relative position $\vec{r}$ with respect to cluster $|Q_{c1}\rangle$.

In choosing the values of $|\vec{r}|$, one needs to find an optimal grid for $\vec{r}$, not too closely packed, to avoid overcompleteness, and not too sparse, to fill the Hilbert space smoothly. The minimum distance — let us call it $|\vec{r}| = r_{min}$ — should be chosen such that the relative wave function of the clusters overlaps at 0.7 of its height the relative wave function were $\vec{r} = 0$, as illustrated in Fig. 5.2. This boils down to the requirement that:

$$r_{min} = 2\sqrt{-\ln(0.7) \times 2(A\, a_{mean}/(A_1 A_2))}. \tag{5.23}$$

The expression (Eq.(5.23)) contains the mean width $a_{mean}$ of all the wavepackets, because, if all packets had the same width, one could separate exactly the relative motion of the clusters as a Gaussian with width $a_{mean}/\frac{(A_1+A_2)}{A_1 A_2}$. The maximum relative distance sensible for inclusion depends somewhat on the binding energy of the nucleus of interest, but as a general rule it should not exceed 10 fm [13].

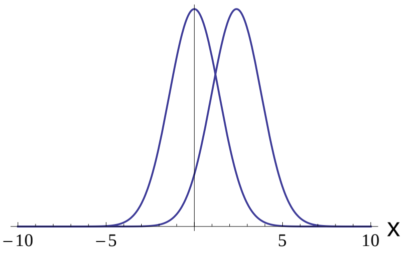

**Figure 5.2:** The two Gaussians represent the relative wave function of the clusters, both when they are situated at $\vec{r} = 0$ and at $|\vec{r}| = r_{min}$, with $r_{min}$ chosen such that the relative wave function in the two scenarios overlaps itself at 0.7 of their heights.

Fig. 5.3 shows a possible choice for the displacement of the cluster 2 with respect to cluster 1. The value $\theta$, describing the orientation, is defined in Figure 5.3, and is the minimum angle required for a given $n$, where $|\vec{r}| = nr_{min}$. One then considers configurations where the clusters are placed at relative orientations in "steps" of $\theta$ (from 0 to $2\pi$). This is also clarified in Fig. 5.3. The requirement that clusters should be at least $r_{min}$ apart can help us choose values of $\theta$: if we consider the setup shown in Fig. 5.3, we choose steps of angle $\theta$ (which describes the relative orientation of the clusters) to be at most 60 degrees, with the magnitude of $\theta$ is most generally given by:

$$\theta = 2\arcsin\left(\frac{1}{2n}\right) \tag{5.24}$$

where $n$ is defined in $|\vec{r}| = nr_{min}$. In the case of an axially-symmetric cluster 1, one need only consider changes in angle $\beta$.

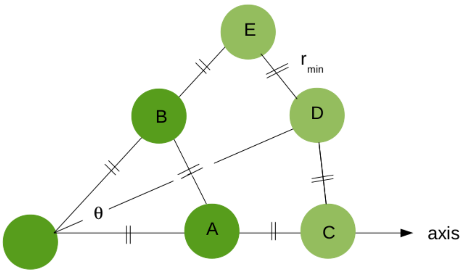

**Figure 5.3:** Relative position of clusters, defining $\theta$. The diagram shows five possible positions (A, B, C, D and E) of a cluster 2 relative to cluster 1, located at the origin. The dark green circles A and B represent clusters a distance $|\vec{r}| = r_{min}$ apart. The paler circles (C, D and E) show clusters displaced by $|\vec{r}| = 2r_{min}$. Each line marked with a strikethrough is equal to $r_{min}$ in length. The angle $\theta$ is defined as the angle between the $x$-axis and the position of the cluster. For the diagram shown, $\theta$ marks the angle between the $x$ axis and cluster B, but if we are calculating the angle $\theta$ for the cluster at D, then it is the angle between the $x$ axis and the line joining the origin to D. From this diagram, we can see that for the cluster at B, the angle $\theta$ is $\pi/3$, while for the cluster at D, a distance $r = 2r_{min}$ from the origin, $\theta$ is $2\arcsin 0.25$.

## 5.5 Matrix elements

The matrix elements of one- and two-body operators for FMD basis states $|Q\rangle$ can be expressed analytically [90]. The matrix elements for many-body states $|Q\rangle$ can be expressed in terms of the single-particle matrix elements, or [90]:

$$\frac{\langle Q|\hat{O}^{[1]}|Q\rangle}{\langle Q|Q\rangle} = \sum_{kl} \langle q_k|\,\hat{O}^{[1]}\,|q_l\rangle \mathbf{o}_{lk} \tag{5.25}$$

for a one-body operator $\hat{O}^{[1]}$ defined as:

$$\hat{O}^{[1]} = \sum_{i=1}^{A} \hat{O}_i. \tag{5.26}$$

In Eq.(5.25), $\mathbf{o}$ is the inverse of the overlap matrix $\mathbf{n}$ for the single-particle states $|q_i\rangle$, or $\mathbf{o} = \mathbf{n}^{-1}$, where [90]:

$$\mathbf{n}_{kl} = \langle q_k|q_l\rangle \tag{5.27}$$

In the case of a two-body operator $\hat{O}^{[2]}$ we will have [90]:

$$\frac{\langle Q|\hat{O}^{[2]}|Q\rangle}{\langle Q|Q\rangle} = \frac{1}{2}\sum_{klmn} \langle q_k q_l|\,\hat{O}^{[2]}\,|q_m q_n\rangle \left(\mathbf{o}_{mk}\mathbf{o}_{nl} - \mathbf{o}_{nk}\mathbf{o}_{ml}\right) \tag{5.28}$$

for a two-body operator $\hat{O}^{[2]}$ defined as:

$$\hat{O}^{[2]} = \sum_{i<j} \hat{O}_{i,j} \tag{5.29}$$

By choosing the appropriate observable $\hat{O}$ one may extract a range of structural information from the states $|Q\rangle$ and from the final FMD states, like spatial densities, momentum distributions, differential cross-section, binding energy and radii.

## 5.6 Coulomb energy

This section describes how Coulomb energy is calculated in FMD.

The operator $\hat{V}_C$ that describes the Coulomb interaction in nuclei is written in terms of the 3-component of the isospin operator $\hat{t}_3$ *i.e.* [16]:

$$\hat{V}_C = \sum_{i<j}^{A} \frac{e^2}{|\vec{r}_i - \vec{r}_j|} \left\{ \frac{1}{2} + \hat{t}_3(i) \right\} \left\{ \frac{1}{2} + \hat{t}_3(j) \right\} \tag{5.30}$$

where the indices $i$ and $j$ count nucleons. This description uses the convention that $t_3 = +\frac{1}{2}$ for the proton.

In the FMD, $\frac{1}{|\vec{r}_i - \vec{r}_j|}$ is written as an integral over Gaussian potentials of different width $\gamma$, or [13]:

$$\frac{1}{|\vec{r}_i - \vec{r}_j|} = \frac{2}{\sqrt{\pi}} \int_0^\infty d\gamma \frac{1}{(2\gamma^{3/2})} exp \left\{ -\frac{(\vec{r}_i - \vec{r}_j)^2}{2\gamma} \right\} \tag{5.31}$$

The matrix elements for a two-body Gaussian potential

$$\hat{G}(\vec{x}_1 - \vec{x}_2) = exp \left\{ -\frac{(\hat{\vec{x}}_1 - \hat{\vec{x}}_2)^2}{2\gamma} \right\} \tag{5.32}$$

are given analytically as (see [13] and refs. therein):

$$\langle a_\kappa \vec{b}_\kappa, a_\lambda \vec{b}_\lambda | \hat{G} | a_\mu \vec{b}_\mu, \alpha_\nu \vec{b}_\nu \rangle = R_{\kappa\mu} R_{\lambda\nu} \left\{ \frac{\gamma}{\alpha_{\kappa\lambda\mu\nu} + \gamma} \right\}^{3/2} exp \left\{ -\frac{\hat{\rho}^2_{\kappa\lambda\mu\nu}}{2(\alpha_{\kappa\lambda\mu\nu} + \gamma)} \right\} \tag{5.33}$$

Here $|a_\mu \vec{b}_\mu, a_\nu \vec{b}_\nu\rangle$ denotes the two-body state $|a_\mu \vec{b}_\mu \otimes |a_\nu \vec{b}_\nu\rangle$; $\alpha_{\kappa\lambda\mu\nu}$ is the mean width of the relative wave function for the pair and $\rho_{\kappa\lambda\mu\nu}$ is the mean distance between the wave-packets. The $R_{kl}$ denote the overlap $\langle a_k, \vec{b}_k | a_l, \vec{b}_l\rangle$. This means that we can relate the Coulomb energy back to the relative wave functions of all the pairs of nucleons in the nucleus. The matrix elements for a two-body $\frac{1}{r}$ potential like the Coulomb potential are then [13]:

$$\langle a_\kappa \vec{b}_\kappa, a_\lambda \vec{b}_\lambda | \frac{1}{r} | a_\mu \vec{b}_\mu, \alpha_\nu \vec{b}_\nu \rangle = R_{\kappa\mu} R_{\lambda\nu} \frac{1}{\sqrt{\rho^2_{\kappa\lambda\mu\nu}}} \text{erf} \left\{ \sqrt{\frac{\rho^2_{\kappa\lambda\mu\nu}}{2\alpha_{\kappa\lambda\mu\nu}}} \right\}. \tag{5.34}$$

where all the terms are as defined in [13], and “erf” is the Error Function.

## 5.7 Interaction

Using realistic[a] interactions, such as the phenomenological Argonne $v18$ interaction (AV18) [91], brings with it the issue of dealing with the short-range repulsion in a tractable model-space. The strong short-range repulsion of a realistic $NN$ interaction means that a pair of nucleons that come into contact will

---

[a] “Realistic” interactions are interactions that reproduce nucleon-nucleon scattering data.

both be scattered to high-momentum states [92]. This scattering shows up as matrix elements of the Hamiltonian in which low-momentum initial states are coupled to high-momentum final states — that is, matrix elements that lie far off the diagonal. In order to use such a hard-core interaction, it must be softened, so that the effect of the scattering to high-momentum modes can be incorporated without having to have an intractably large model-space. In order to incorporate configuration mixing of low- and high-momentum states in even $^4$He, when using Slater Determinants of simple-harmonic oscillator single particle states, one would need $10^8$ Slater Determinants to include all correlations and get a converged ground state with the AV18 interaction [93]. Clearly, some softening of the interaction is necessary for calculations to proceed.

The FMD requires that the interaction is written in an operator format in order to be implemented in the FMD calculations. Transforming the interaction to soften it is thus less straightforward, as the Renormalization Group (RG) method is designed for interactions written in a matrix-element format (*e.g.* [94]). Therefore in FMD one uses the Unitary Correlation Operator Method (UCOM) (see *e.g.* [93, 95, 96]), which results in an explicit operator form for the softened interaction.

A UCOM-transformed Argonne $v$18 (AV18) interaction [97] was used throughout this study. The AV18 interaction is designed to be local, with the necessary momentum-dependence incorporated in the terms $L^2$ and $LS$ [98]. The interaction is realistic, since it reproduces phase-shifts [91], and is usually the "interaction of choice" for calculation of light mass nuclei. The UCOM is summarised in the next section (Section 5.8) and some important features of the UCOM-transformed AV18 are mentioned.

## 5.8 Unitary Correlation Operator Method (UCOM) and UCOM-transformed AV18

This overview is based on references [93, 95, 96].

One can consider the effect of short-range repulsion on the nuclear configuration as a displacement of nucleons out of the repulsive core to create the so-called "correlation hole" [98]. UCOM starts from the central idea of transforming the many-body states to incorporate these short-range correlations on a shell-model like uncorrelated state $|\Psi\rangle$. This can be done by applying a "correlation operator" $\hat{C}$ to the states $|\Psi\rangle$:

$$\hat{C}|\Psi\rangle = |\tilde{\Psi}\rangle. \tag{5.35}$$

However, incorporating the correlations in $|\Psi\rangle$ is equivalent to applying the correlation operator on either side of the Hamiltonian, since [93]:

$$\langle\tilde{\Psi}|\hat{H}|\tilde{\Psi}\rangle = \langle\Psi|\hat{C^{\dagger}}\hat{H}\hat{C}|\Psi\rangle. \tag{5.36}$$

This gives a new Hamiltonian $\hat{H}_{eff} = \hat{C^{\dagger}}\hat{H}\hat{C}$.

The unitary correlation operator $\hat{C}$ has the form [93]:

$$\hat{C} = e^{-i\hat{G}}, \tag{5.37}$$

where $\hat{G} = \sum_{i<j}^{A} \hat{g_{ij}}$ is the generator of the correlations, and the $\hat{g_{ij}}$'s are two-body operators acting between a pair of particles. They are defined differently depending on the kind of short range correlations they represent [98]: short-range central correlations, which shift nucleon density out of the nuclear centre, are defined as shifts that depend on relative distance of a pair of nucleons. Tensor correlations are induced by moving a $T=0$ nucleon pair such that their distance vector is aligned with the total spin $\vec{S}$. The strength of each shift depends on which potential one is transforming, and on $|\Psi\rangle$ itself and whether or not it already incorporates some correlations [98].

The actual means of applying $\hat{C}$ to $\hat{H}$ is discussed in [93] or [98]. Suffice to say that, since the generator $\hat{G}$ of the correlations is two-body; many-body terms $\hat{H}_{eff}^{[i]}$ are induced in the Hamiltonian $\hat{H}_{eff}$, *i.e.* [93]:

$$\hat{H}_{eff} = \hat{H}_{eff}^{[1]} + \hat{H}_{eff}^{[2]} + \hat{H}_{eff}^{[3]} + \cdots . \tag{5.38}$$

When the range of the two-body correlations is small compared to the inter-particle distance, one may restrict oneself to the two-body part of this transformed Hamiltonian [20]. The transformed Hamiltonian up to two-body is therefore what one calls the UCOM Hamiltonian.

This method has been tested and shown to produce the correct phase-shifts [98], and No-core shell-model calculations using a UCOM-transformed Argonne $v18$ (AV18) interaction [91] have shown that the two-body UCOM interaction gives a good description of light $p$-shell nuclei [93].

In this study, the UCOM is used to transform the Argonne $v18$ interaction (AV18). In order to incorporate the effects of the missing three- and higher-body terms, one may change the strength of the spin-orbit term ($LS$ term). We start by multiplying with 2, but vary the factor to see which value best reproduces the experimental properties of the nuclei in question. The magnitude of the spin-orbit term has a rather noticeable effect on transition strengths, since it favours the occupation of states with orbital angular momentum and spin aligned, and this can “falsely boost” transition strengths if the strength of the $LS$ term is too strong. We therefore use transition strengths as a guide for adjusting this coefficient.

# 6 Calculations and Results

Here the calculations, including the choice of basis and strength of the $LS$ term, are discussed for all six nuclei. The results for each nucleus (*i.e.* the calculated observables) are provided and compared to experiment and results from comparable models.

## 6.1 $^8$Li

The first trial basis set for $^8$Li consists of unconstrained VAP states with angular momenta and parities of $0^+$, $1^+$, $2^+$ and $3^+$. With a $^7$Li core (spin and parity $3/2^-$) and a neutron in the p-shell, configurations with these spins and parities are possible. Each proton and neutron was described spatially by a single Gaussian wave-packet.

The proton- and neutron-density plots of the intrinsic state $|Q\rangle$ for each of these unconstrained VAP configurations are provided as Fig. 6.1. One can note the formation of clusters, and an extended distribution for the loosely-bound neutron in the $0^+$ configuration. Energies of the states of $^8$Li can be obtained by diagonalising the Hamiltonian in this basis of 4 unconstrained VAP states. These are provided in the Figure 6.3. One must note first of all that the $0^+$ state with isospin 2 (which lies at 10.822 MeV above the ground state) is not reproduced in this basis, as the $0^+$ VAP basis state has isospin 1. One can also note under-binding. It is clear that there is a need for more configurations.

Constraints on matter radius $R$ were chosen to create new basis configurations. Matter radius constraints are suitable for $^8$Li, $^8$Be and $^8$B as well, as all are characterised by unusually-large matter radius for the number of nucleons involved. Using the same set of constraints for all nuclei in the $T=1$ isomultiplet seems a good policy for consistency among the basis sets.

The radius-constrained basis states were created with constraint $R = \sqrt{\langle r^2\rangle}$ varying between 2.1 and 3.9 fm in steps of 0.2 fm, and states of angular momentum and parity $J^\pi = 1^+$ to $3^+$. This gives a total of 30 states.

Fig. 6.2 shows the energies of the low-lying states of $^8$Li as a function of basis size when including larger values in the grid of $R$-values. When the low-lying energies start to show convergence behaviour, this means that inclusion of further basis states will not improve the structure of the low-lying eigenstates further. The energies of the first three excited states show convergence behaviour with a basis of 27 states, or $R$ values up to 3.7 fm.

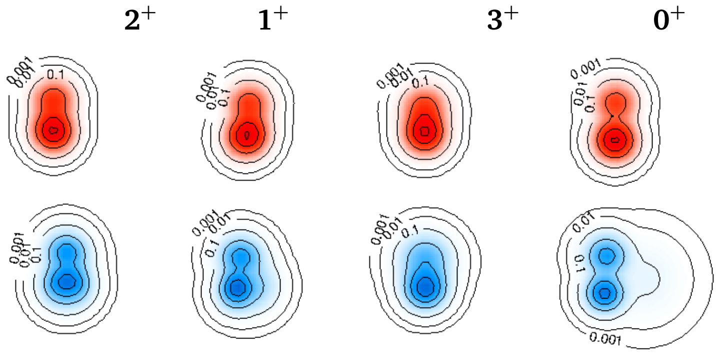

**Figure 6.1:** Intrinsic proton- (red) and neutron-densities (blue) for the VAP basis configurations for $^8$Li. These are densities for the intrinsic configurations. The numbers on the contour lines give density in units of the saturation density $\rho_0$=0.17 fm$^{-1}$. Numbers to the right of the configurations show angular momentum and parity. Compare to the densities for the same projected states in $^8$B (Fig. 6.12). In the $^8$Li case, there is only an extended neutron-distribution in the $0^+$ state.

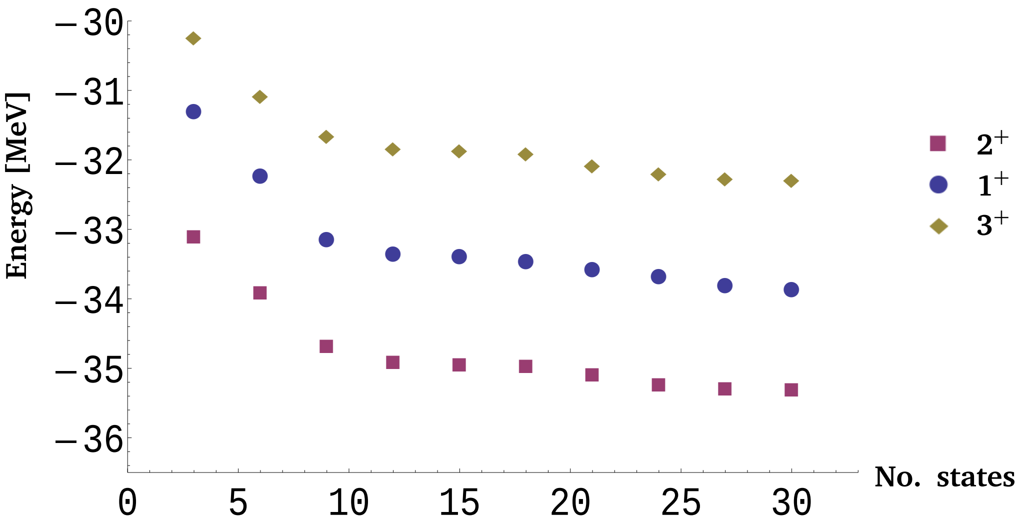

**Figure 6.2:** Energies of $^8$Li states, plotted with basis size of the $R$-constrained basis set, by including VAP states with increasing $R$-constraint from $R$=2.1 fm to 3.9 fm in steps of 0.2 fm.

In order to compare calculated energy levels for $^8$Li with those for the mirror nucleus $^8$B, it was decided to add to the $^8$Li basis the configurations of $^8$B, with neutrons "swapped" for protons (that is, the $^8$B Slater determinants, but with neutrons in the single-particle proton states and *vice versa*).

Without the inclusion of such mirror configurations in both bases, one cannot know whether shifts in the energies of the mirror states are due to the absence of some configurations in one of the bases. Adding the isospin-mirrored states from $^8$B to the $^8$Li basis and *vice-versa* adds 18 states to our set of 27 basis states (the converged radius-constrained basis set for $^8$B consists of 18 states); giving a total of 45 basis states for $^8$Li. The energy levels calculated in this basis are supplied in Figure 6.3. We call this basis $R_{ext}$, since it is "extended" with the mirror configurations.

To model the asymptotic part of the wave functions, one may include explicit clustering configurations. The relevant ones for (especially the low-lying states) in $^8$Li are $^7$Li+n states, as the threshold for decay of $^8$Li into $^7$Li+n lies 2.032 MeV above the ground state (see [5] and Fig. 2.6). The minimum separation $r_{min}$ for the $^7$Li+n clusters ($r_{min}$ is defined in Eq.(5.23)) was calculated to be 2.5 fm. Cluster

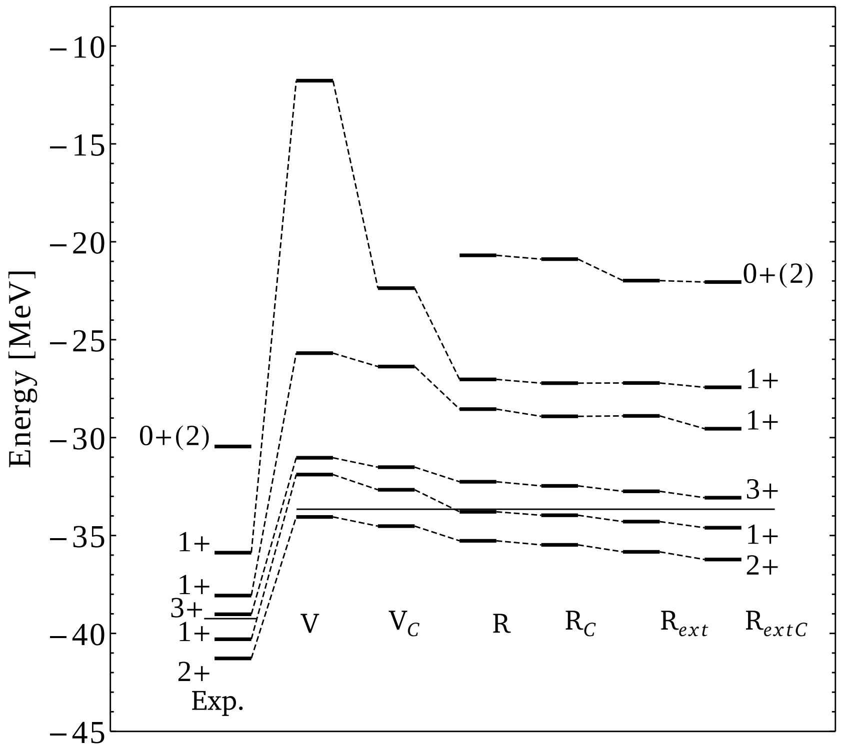

**Figure 6.3:** Level-scheme of $^8$Li. See Table 6.4 for labels. Thin lines are experimental and calculated $^7$Li+n thresholds (Section 6.2).

configurations with a separation of 5.0 fm between the $^7$Li core and the neutron were also included. This gives a total of 11 cluster basis states, because for the clusters separated by 2.5 fm there are five possible orientations of the neutron relative to the $^7$Li core, and 6 such possibilities for their placement 5.0 fm apart (see also Fig. 5.3 for additional clarification). Mirrors of the core-plus-proton configurations for $^8$B were added to this subset of $^8$Li basis states. Plots for the proton- and neutron-densities of the $^8$B and $^8$Li cluster configurations are provided in Table 37 and 38 in Appendix 4. These cluster configurations were added to the $R$-constrained basis sets, and the Hamiltonian was diagonalised in this Hilbert space.

Eigenstate energies obtained in $^8$Li in all the basis sets are supplied in Fig. 6.3, and radii, moments and transition probabilities are provided in Tables 6.1-6.3. Two different coefficients of the spin-orbit term (values of 1.5 and 2.0) were used in the Hamiltonian for the "R$_{ext}$" and "R$_{ext}$+C" bases (Table 6.4 is an index of what configurations are included in each basis). The eigenstate energies for $^8$Li are compared to those for $^8$B in Section 7.7.

The NCSM calculations of [99] used an interaction obtained from chiral effective field theory, which is different from our interaction. We compare to the energies they calculated with up to two body terms included. It was decided to compare our results to those calculated using only up to to two-body terms, since the UCOM-transformed AV18 is truncated at two-body, with the additional three- and higher-body terms included by means of increasing the strength of the spin-orbit term, as discussed. In order to compare to their calculations using two-body forces, we performed calculations using the UCOM-transformed AV18 with an $LS$ term with factor 1. Our calculations compare relatively well with theirs, especially as regards binding relative to threshold. The model-space of [99] is an $8\hbar\Omega$ space.

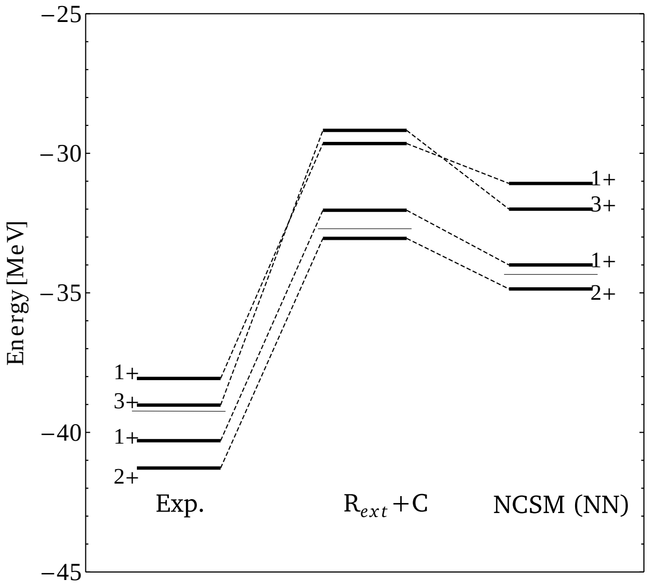

**Figure 6.4:** Comparing our $^8$Li energy results (calculated in the largest basis set R$_{extC}$) to NCSM calculations of [99] (NCSM) calculated with 2-body forces (labelled here as NCSM (NN)). The thin lines indicate the experimental and calculated $^7$Li+n thresholds. In order to compare to their calculations using two-body forces, we performed calculations using the UCOM-transformed AV18 with an $LS$ term with strength factor 1. The threshold energy was also recalculated with the same interaction.

**Table 6.1:** Calculated rms matter, charge, proton and neutron radii for the $^8$Li ground state, for various basis sets. Labels as in Table 6.4. References for experimental values provided in square brackets beside the values.

| | $R_{matter}$ [fm] | $R_p$ [fm] | $R_n$ [fm] | $R_{charge}$ [fm] |
|---|---|---|---|---|
| Exp. | 2.37(2) [40] | | | 2.29(8) fm [75] |
| V | 2.147 | 2.007 | 2.226 | 2.152 |
| V$_C$ | 2.177 | 2.017 | 2.267 | 2.161 |
| $R$ | 2.265 | 2.098 | 2.359 | 2.237 |
| $R_C$ | 2.263 | 2.089 | 2.362 | 2.228 |
| $R_{ext}$ (2) | 2.242 | 2.079 | 2.334 | 2.219 |
| $R_{extC}$ (2) | 2.243 | 2.070 | 2.341 | 2.211 |
| $R_{ext}$ (1.5) | 2.323 | 2.130 | 2.431 | 2.267 |
| $R_{extC}$ (1.5) | 2.318 | 2.118 | 2.430 | 2.255 |

**Table 6.2:** Calculated magnetic dipole moment $\mu$ and quadrupole moment $Q$ for $^8$Li the ground state, for various basis sets. The first column indicates the basis set. Labels as Table 6.4. The numbers in brackets give the the strength factor of the $LS$ term in the interaction.

| | $\mu$ [$\mu_N$] | $Q$ [fm$^2$] |
|---|---|---|
| Exp. | 1.653560(18) [5] | 3.27(6) [5] |
| V (2.0) | 1.579 | 2.580 |
| V$_C$ (2.0) | 1.585 | 2.516 |
| $R$ (2.0) | 1.535 | 2.755 |
| $R_C$ (2.0) | 1.531 | 2.692 |
| $R_{ext}$ (2.0) | 1.480 | 2.930 |
| $R_{extC}$ (2.0) | 1.477 | 2.888 |
| $R_{ext}$ (1.5) | 1.299 | 3.157 |
| $R_{extC}$ (1.5) | 1.296 | 3.095 |

**Table 6.3:** Transition strengths $B(M1)$ calculated in $^8$Li in different bases. Labels of the basis states are as in Table 6.4. Measured values from [5] and [99].

| States | Basis | Experimental energy [MeV] | Calculated Energy [MeV] (2.0) | Calculated Energy [MeV] (1.5) | Experimental $B(M1)$ [$\mu_N^2$] | Calculated $B(M1)$ [$\mu_N^2$] (2.0) | Calculated $B(M1)$ [$\mu_N^2$](1.5) |
|---|---|---|---|---|---|---|---|
| $1^+ \rightarrow 2^+$ | V | 0.980 | 2.164 | 1.785 | 5.00(16) | 4.926 | 4.354 |
| | V$_C$ | | 1.857 | 1.447 | | 5.039 | 4.539 |
| | R$_{ext}$ | | 1.545 | 1.161 | | 5.353 | 5.133 |
| | R$_{extC}$ | | 1.622 | 1.261 | | 5.317 | 5.080 |
| $3^+ \rightarrow 2^+$ | V | 2.255 | 3.022 | 3.638 | | 0.216 | 0.092 |
| | V$_C$ | | 3.011 | 3.573 | | 0.246 | 0.119 |
| | R$_{ext}$ | | 3.092 | 3.553 | | 0.228 | 0.093 |
| | R$_{extC}$ | | 3.155 | 3.611 | | 0.231 | 0.097 |

**Table 6.4:** Table of different basis sets, defining the abbreviations used.

| | |
|---|---|
| V | Set of 3 VAP configurations (one projected on each of the three lowest-lying angular momenta). |
| V$_C$ | Same set as above, with cluster configurations added. |
| R | Radius-constrained VAP basis states for each angular momentum. |
| R$_C$ | Same set as above, with cluster configurations added. |
| R$_{ext}$ | Radius-constrained VAP basis states for each angular momentum, plus the isospin-partner or “mirror” configurations. |
| R$_{extC}$ | Same set as above, with cluster configurations added. |
| R+T+S | Radius-constrained VAP basis states for each angular momentum, plus VAP basis states with constraints simultaneously placed on $\langle\hat{\vec{T}}^2\rangle$ and $\langle\hat{\vec{S}}^2\rangle$. |
| R+T+S$_C$ | Same set as above, with cluster configurations added. |
| R+Q | Radius-constrained VAP basis states for each angular momentum, plus VAP basis states with constraints on $\langle\hat{Q}\rangle$ included. |
| R+Q$_C$ | Same set as above, with cluster configurations added. |
| T | Isospin- and spin-constrained VAP basis states for each angular momentum, plus VAP basis states with constraints on $\langle\hat{Q}\rangle$ included. |
| T$_C$ | Same set as above, with cluster configurations added. |

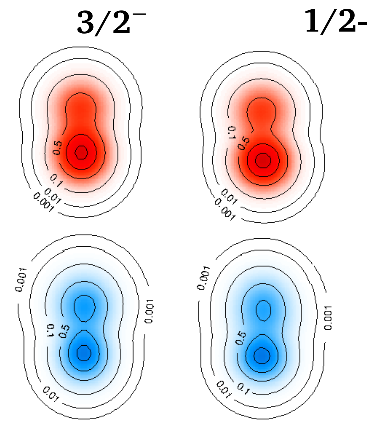

**Figure 6.6:** Proton- and neutron-densities of $^7$Li unconstrained VAP basis states. Numbers on the contour lines and to the right as in Fig. 6.1.

## 6.2 $^7$Li core and threshold

When making the $^8$Li cluster configurations, the $^7$Li core was modelled by a single unconstrained VAP state projected on $3/2^-$. The proton- and neutron-density for the intrinsic configuration is shown in Fig. 6.6.

In order to obtain a calculated $^7$Li threshold, one needs also an FMD basis set for $^7$Li. This consisted of 14 radius-constrained VAP states ($R$ ranging from 2.1 to 3.3 in steps of 0.2 fm, giving 7 intrinsic states each for the projected angular momenta and parities $3/2^-$ and $1/2^-$). The basis size was chosen by checking convergence behaviour of the energies of the $3/2^-$ and $1/2^-$ states. After inclusion of radius-constrained states beyond a set of 14 basis states (7 for each of the 2 angular momenta considered), one obtains convergence behaviour (Fig. 6.5). The proton- and neutron-density plots for the intrinsic state of the $1/2^-$ VAP configuration is also shown in Fig. 6.6.

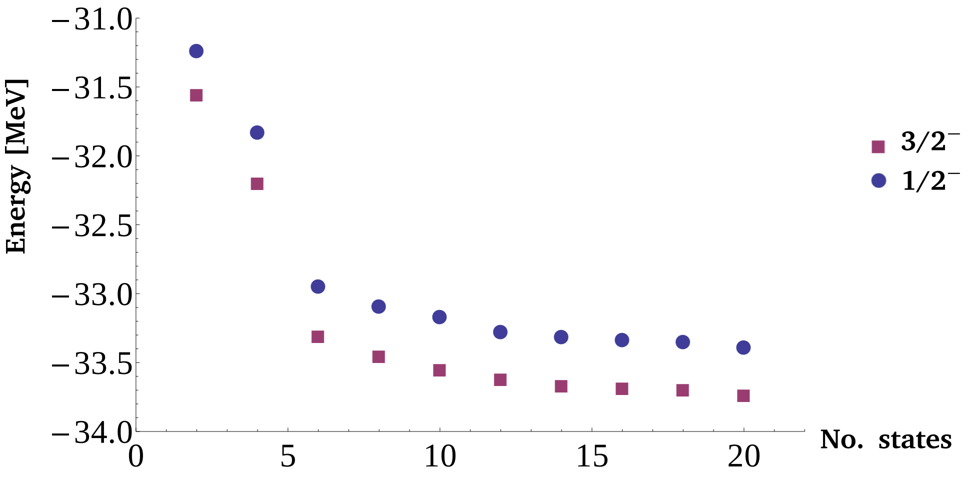

**Figure 6.5:** Energies of $^7$Li states, plotted with basis size for increasing radius constraint $R$=2.1 fm to 3.9 fm in steps of 0.2 fm. Convergence behaviour occurs near a basis of 14 basis states, or $R$ up to 3.3 fm.

For $^8$Be, as for $^8$Li, the starting basis is unconstrained VAP states. For $^8$Be, states with angular momenta and parities of $0^+$, $2^+$ and $4^+$ were projected out. The ground state is $0^+$, and the introduction of a relative angular momentum between the two $\alpha$ particles making up that ground state gives rise to the $2^+$ and $4^+$ states. Each proton and neutron was described spatially by a single Gaussian wave-packet.

The proton- and neutron-density plots for the $0^+$ and $2^+$ unconstrained VAP states are provided as Fig. 6.7. One can note the clear formation of clusters. Note that, in these intrinsic distributions, the two clusters are not identical. Note also that the energy of the $4^+$ state (and in principle also the $2^+$ state) would be minimised when the two $\alpha$ clusters are infinitely-far apart; but that such a configuration cannot be realised within a finite number of iterations of the minimisation process. The density plot for the $4^+$ state is thus not shown, since the configuration will depend purely on the number of iterations performed in the minimisation, making any density distribution somewhat arbitrary. The Hamiltonian was diagonalised in the basis of these three configurations. The energies for the ground- and excited-states are provided in Figure 6.10. Here again, one notes under-binding and the need for more configurations.

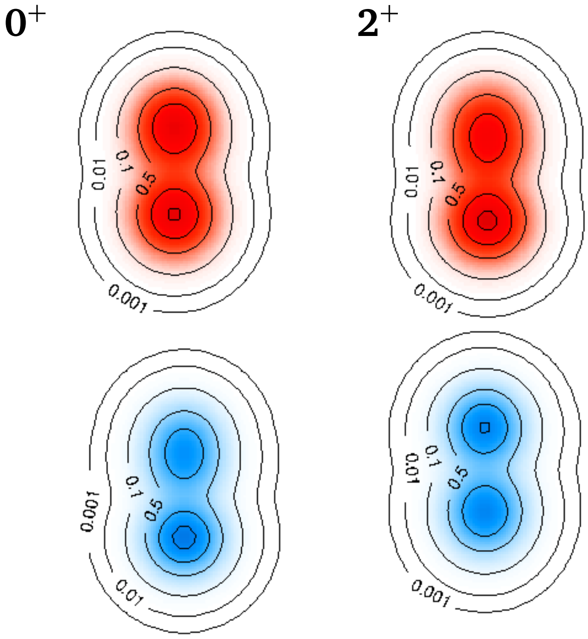

**Figure 6.7:** Proton- (red) and neutron-densities (blue) for the VAP basis configurations for $^8$Be. Numbers on the contour lines and to the left as in Table 6.4. Compare to the densities for the same projected states in $^8$Li (Fig. 6.1), or $^8$B (Fig. 6.12).

Constraints on matter radius $R$ were used to extend the basis, as in $^8$Li. The maximum constraint value ($R$=3.5 fm) was chosen according to convergence of the ground state energies, as in the previous case: Figure 6.8 shows the that the ground- and low-lying excited state energies show convergence behaviour after a basis set of 24 basis states (or 8 for each angular momentum and parity $0^+$, $2^+$ and $4^+$). The Hamiltonian was diagonalised in this basis, and energies of the eigenstates are given in Fig 6.10, labelled with $R$.

The explicit clustering configurations relevant for $^8$Be are the 2-$\alpha$ configurations. The value of of $r_{min}$ (as defined in Eq.(5.23) was 1.6 fm, and so separations of 1.6 fm and 2.3 fm were both used. Plots of the proton- and neutron-densities for these clustering configurations are provided in Table 39 of Appendix 4. The mirrors of the $^8$Li, $^8$B cluster configurations were added to this subset of basis states. Radii and transition probabilities for all basis sets are provided in Tables 6.5- 6.6.

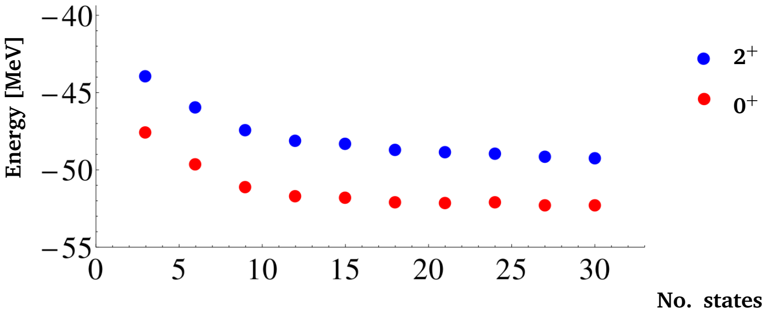

**Figure 6.8:** Calculated ground state and first excited state energy of $^8$Be, plotted with basis size of the $R$-constrained basis set, showing convergence behaviour near a basis of 27 basis states (9 for each angular momentum).

## 6.4 The $T$=1 states

There are two possible ways to obtain a basis that can accurately model the higher lying ($T=1$ or 2) states. These are: Start with intrinsic (antisymmetrised product) states $|Q\rangle$ of $^8$Li ($T=1$,$T_3$=-1) and $^8$B ($T=1$,$T_3$=-1), and raise (or lower) the isospin in order to create states of isospin $T=1$, with projection $T_3=0$. Mathematically, this raising and lowering is done by the isospin raising and lowering operators:

$$\hat{\vec{T}}_+|Q;T_3=-1\rangle=\sum_{i=1}^{A}\hat{t}_+(i)|Q;T_3=-1\rangle \tag{6.1}$$

for moving from states in $^8$Li ($T=1$,$T_3$=-1) to states in $^8$Be, and

$$\hat{\vec{T}}_-|Q;T_3=1\rangle=\sum_{i=1}^{A}\hat{t}_-(i)|Q;T_3=1\rangle \tag{6.2}$$

when moving from states in $^8$B ($T=1$, $T_3=1$) to states in $^8$Be.

In practise, moving from the $^8$Li and $^8$B basis states to those in $^8$Be is not done by using the single superposed states given in Eqs.(6.1) and (6.2), but by successively changing each one of the five protons to a neutron in each radius-constrained $^8$B basis state and thus creating 5 new $^8$Be basis states for each $|Q\rangle$ of $^8$B or $^8$Li. As the Hamiltonian is to good approximation isospin-invariant, its eigenstates will consist of the appropriate linear combinations for $T$ and $T_3$.

While it would be wise for the sake of consistent treatment of the $A=8$ isotriplet nuclei to use the basis set that contains all such $^8$B and $^8$Li isospin-partner states, it was not possible to do so. The transition strengths could not be calculated in such a large basis set (260 states). It was thus necessary to restrict the basis until it was of a size that allowed for calculation of transition strengths. This was done by removing $^8$Li and $^8$B isospin-partner states successively from the basis set until the maximum basis in which transition strengths could be calculated was achieved. This led to a restricted set of 104 basis states (set $R_{ext}$).

The second way to improve the modeling of $T=1$ states for $^8$Be is to create $^8$Be basis states with a constraint on $\langle\hat{\vec{T}}^2\rangle$ and $\langle\hat{\vec{S}}^2\rangle$ simultaneously. These states can then be added to the set of $^8$Be basis states with constraints on $R$. Constraining $\langle\hat{\vec{T}}^2\rangle$ and $\langle\hat{\vec{S}}^2\rangle$ simultaneously forces the minimisation process to access the compact configurations, because the alpha particles are “broken” by placing constraints that require values for $\langle\hat{\vec{T}}^2\rangle$ and $\langle\hat{\vec{S}}^2\rangle$ not equal to zero.

The states with constraints on $\langle\hat{\vec{T}}^2\rangle$ and $\langle\hat{\vec{S}}^2\rangle$ were projected on angular momenta and parity $0^+$, $1^+$ and $2^+$ (instead of $0^+$, $2^+$ and $4^+$, like for the radius constrained states), simply because there are no $4^+$ states with $T=1$ known in $^8$Be. The constraints on $\langle\hat{\vec{T}}^2\rangle$ and $\langle\hat{\vec{S}}^2\rangle$ themselves were varied between 0 and 3 for states with $\langle\hat{\vec{T}}^2\rangle = T(T+1)$. To select members of the basis set (referred to as the "T" basis set (Table 6.4), basis states with constraint on $\langle\hat{\vec{T}}^2\rangle$ and $\langle\hat{\vec{S}}^2\rangle$ were added sequentially to the basis set of radius-constrained basis states, and the energies of the low-lying states obtained in these different bases are plotted with basis size in Fig. 6.9. The figure shows that one only needs to add basis states with constraints up to $\langle\hat{\vec{T}}^2\rangle$ =2 and $\langle\hat{\vec{S}}^2\rangle = 2$: energies are minimised equally-well if $\langle\hat{\vec{T}}^2\rangle$ or $\langle\hat{\vec{S}}^2\rangle = 3$, but not any better, so these states with $\langle\hat{\vec{T}}^2\rangle$ and $\langle\hat{\vec{S}}^2\rangle = 3$ were omitted from the set.

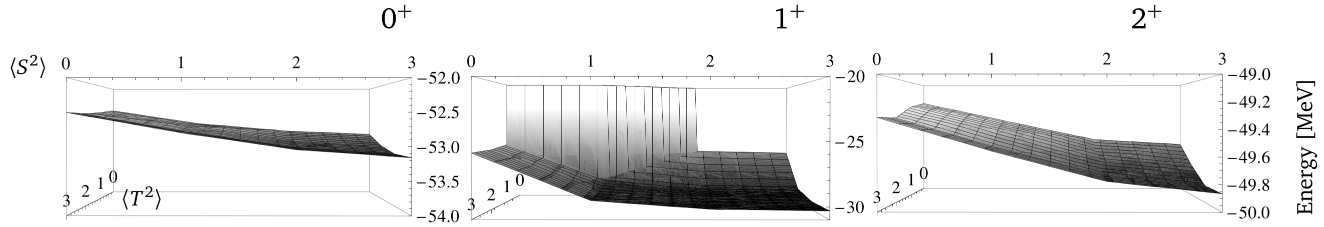

**Figure 6.9:** Calculated energies for the low-lying states of $^8$Be, plotted with basis size as described. The plots show convergence behaviour for a basis set including states with constraint values up to $\langle\hat{\vec{T}}^2\rangle$=2 and $\langle\hat{\vec{S}}^2\rangle$=2. The spin, parity and isospin $J^\pi(T)$ is provided in the top right corner of each plot. Note that the $1^+$ state is $T=1$ state, and that it is understandably very sensitive to the inclusion of greater magnitudes of isospin.

It could be argued that, to obtain the $T=1$ states of $^8$Be one could simply project on isospin $T=1$ as one does for the spin. However, in our FMD calculations we use nucleons of pure isospin projection ($t_3$ is either 1/2 or -1/2; the nucleons are either protons or neutrons). As projecting on good total isospin for the many-body wave function would require one to rotate the isospins of the nucleons to some orientation that is neither $t_3$=1/2 nor $t_3$=-1/2, performing such a projection is not possible.

Our results, calculated in the full ($R_{ext}$) space, are compared to the most recent NCSM results [99] in Fig. 6.11. The calculation of [99] for $^8$Be was carried out using the same interaction and model space as that which they performed for $^8$Li (to which we compare out $^8$Li results in Fig. 6.4). Our results compare very favourably with theirs, especially for the ground state and low-lying levels. When the $T=1$ states are calculated with a spin-orbit term $LS$ of coefficient 1, they can be seen to be rather-poorly reproduced. This can be understood through the fact that these states are compact, and so will suffer more from the exclusion of three- and higher-body forces; which the increased magnitude of the spin-orbit term replaces in our interaction.

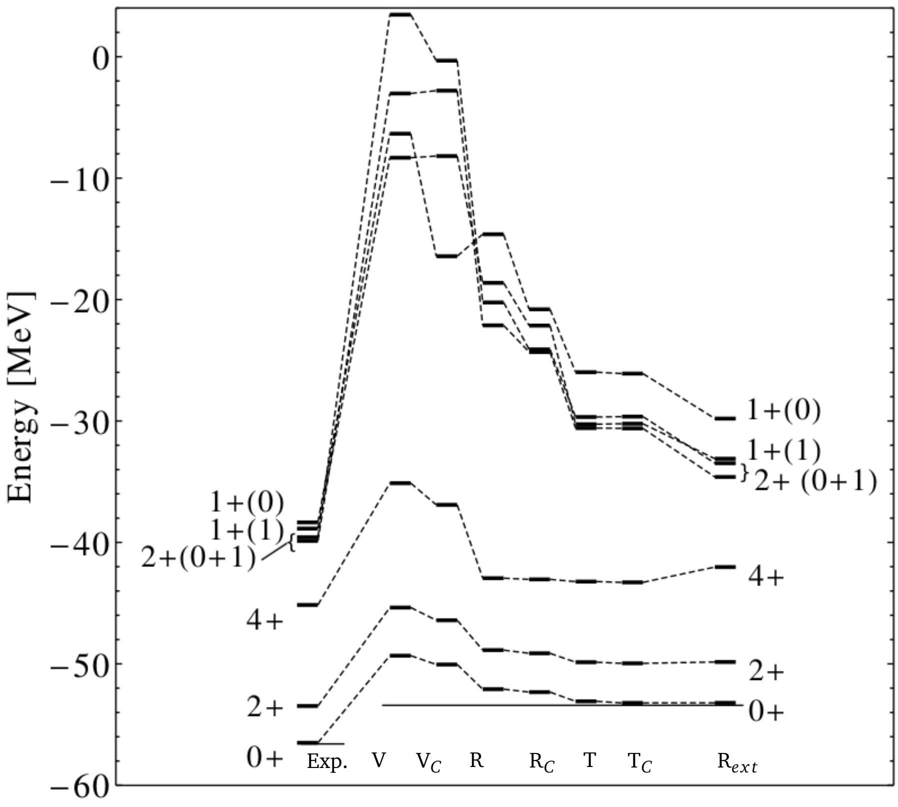

**Figure 6.10:** Level-scheme of $^8$Be comparing experimental and calculated ground and excited state energies in different basis sets. Labels for the basis sets are in Table 6.4. Numbers in parentheses give the isospin of the levels. The thin lines indicate the experimental and calculated two-$\alpha$ thresholds. The two-$\alpha$ threshold in this case is simply twice the energy obtained for a single $0^+$ VAP state for $^4$He.

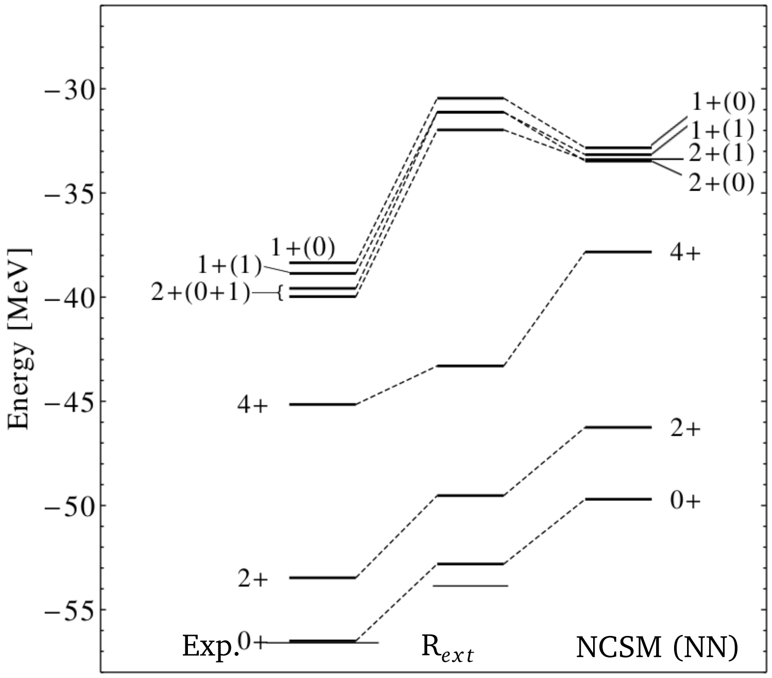

**Figure 6.11:** Level-scheme of $^8$Be comparing our results (calculated in the basis set R$_{ext}$) to NCSM calculations of [99] (NCSM (NN)). As in Fig. 6.4 for $^8$Li, results are calculated without an amplification factor of the $LS$ term. The thin lines indicate the experimental and calculated 2-alpha thresholds.

**Table 6.5:** Calculated rms matter, charge, proton and neutron radii for the $^8$Be ground state, calculated in various basis sets. Labels for the basis sets as in Table 6.4.

| | $R_{matter}$ [fm] | $R_p$ [fm] | $R_n$ [fm] | $R_{charge}$ [fm] |
|---|---|---|---|---|
| Exp. | - | | | |
| V | 2.282 | 2.286 | 2.277 | 2.431 |
| V$_C$ | 2.229 | 2.234 | 2.224 | 2.381 |
| $R_{ext}$ | 2.404 | 2.408 | 2.400 | 2.545 |
| $T$ | 2.523 | 2.530 | 2.516 | 2.661 |
| $T_C$ | 2.500 | 2.507 | 2.493 | 2.639 |

**Table 6.6:** Transition strengths $B(\Lambda M)$ calculated for $^{8}$Be in different bases. Labels as in Table 6.4. Measured values from [100].

| States | Basis | Experimental energy [MeV] | Calculated Energy [MeV] (2.0) | Calculated Energy [MeV] (3.0) | Experimental $B(E2)$ [$e^2fm^4$] | Calculated $B(E2)$ [$e^2fm^4$] (2.0) | Calculated $B(E2)$ [$e^2fm^4$](3.0) |
|---|---|---|---|---|---|---|---|
| $2^+ \rightarrow 0^+$ | V | 3.03 | 3.962 | 3.958 | | 12.485 | 12.396 |
| | $V_C$ | | 3.645 | 3.343 | | 10.390 | 9.287 |
| | $R_{ext}$ | | 3.367 | 3.117 | | 18.515 | 12.281 |
| | T | | 3.220 | 3.269 | | 26.940 | 10.177 |
| | $T_C$ | | 3.267 | 3.235 | | 25.791 | 10.480 |
| $4^+ \rightarrow 2^+$ | V | 8.047 | 14.204 | 14.183 | 25(8) | 18.543 | 18.402 |
| | $V_C$ | | 13.150 | 11.992 | | 13.879 | 10.751 |
| | $R_{ext}$ | | 7.891 | 7.628 | | 33.877 | 15.229 |
| | T | | 9.134 | 12.101 | | 66.830 | 12.536 |
| | $T_C$ | | 9.815 | 11.610 | | 62.776 | 21.820 |

## 6.5 $^{8}$B

As in the case of $^{8}$Li and $^{8}$Be, the first trial basis set consists of unconstrained VAP configurations, projected on $J^{\pi} = 0^+$, $1^+$, $2^+$ and $3^+$. These spins and parities were chosen because, with a $^{7}$Be core with $3/2^-$ ground state and first excited 1/2- state, plus a p3/2 proton, positive-parity states of total angular momentum 0 to 3 can be formed. One Gaussian wave-packet was used to describe each of the neutrons and four of the protons in phase-space, while the fifth proton was described spatially by a superposition of two Gaussians, to allow for the proton halo of $^{8}$B. Plots of the proton- and neutron-density distributions for these three intrinsic VAP states are shown in Figure 6.12. One can note in this figure the appearance of clustering and of an extended distribution for a proton, even in the $2^+$ ground state.

The energies of the eigenstates obtained in this basis are provided in the level scheme (Fig 6.14). As before, one may note under-binding of the ground state in this basis with respect to the calculated $^{7}$Be+p threshold, and the need for more configurations.

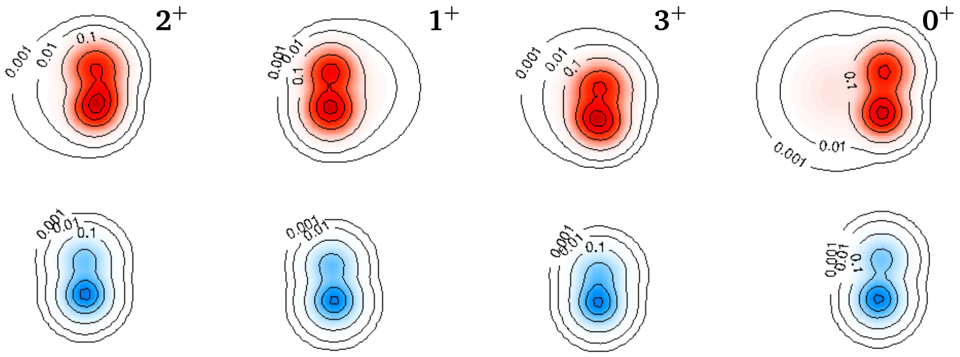

**Figure 6.12:** Proton- (red) and neutron-densities (blue) of intrinsic configurations for $^{8}$B. The numbers on the contour lines give nucleon density in units of the saturation density $\rho_0 = 0.17\text{fm}^{-1}$. Numbers to the right show spin and parity used in the VAP calculation.

The basis set was extended by performing minimisation (Eq.(5.6)) subject to constraints on matter radius, set to $R$= 2.1, 2.3... fm increasing in steps of 0.2 fm. A plot of the low-lying energies with basis size (Fig. 6.13) shows convergence behaviour after a basis set of only 18 basis states, or $R$ up to 3.1 fm. The 27 $^8$Li "mirror" states were added to this basis set, and the Hamiltonian was diagonalised in this set of 45 basis states (basis set R$_{ext}$).

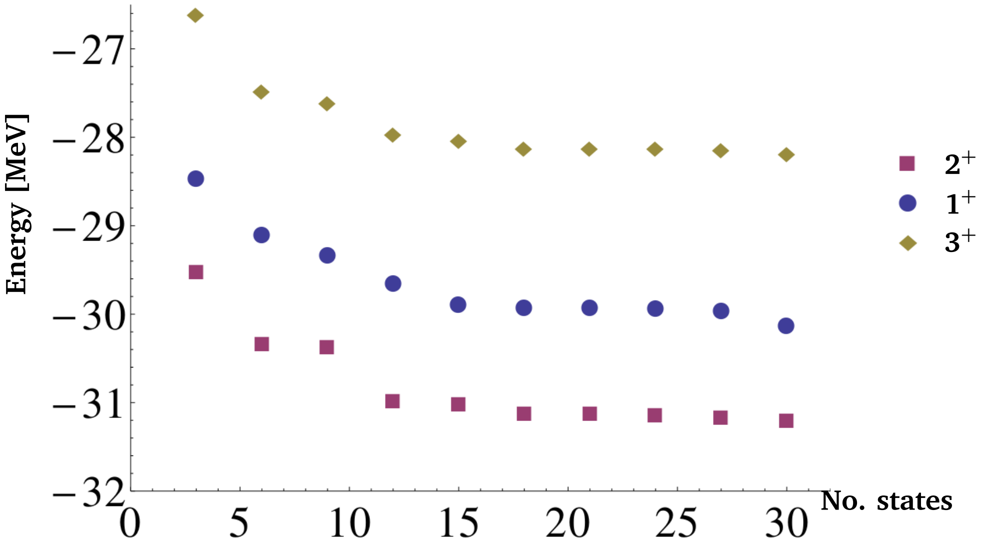

**Figure 6.13:** Calculated ground state energy of $^8$B plotted with basis size of the $R$-constrained basis set, showing convergence behaviour near 18 basis states. The slight downward tilt of the $1^+$ energies at a basis size of 30 states is possibly caused by over-completeness of the basis.

The cluster configurations relevant to $^8$B are $^7$Be+p states, as the threshold for decay of $^8$B into $^7$Be+p is only 0.137 MeV above the ground state (see [5] and Fig. 2.2). The $r_{min}$ value for our $^7$Be+p configurations (see Eq.(5.23)) is 2.6 fm. Cluster configurations with $r_{min}$ = 5.2 fm were also included, to take into account extended distributions of the odd proton. This gives a total of 11 cluster basis states. Density plots for the proton- and neutron-densities of the $^8$B core-plus-proton configurations are provided in Table 37 in Appendix 4. The mirror configurations of the $^8$Li cluster states were added to the $^8$B cluster states, giving 22 cluster configurations. These 22 cluster configurations were added to the $R$-constrained basis sets, and the Hamiltonian was diagonalised in this Hilbert space.

Energy levels obtained in each of the basis sets for $^8$B are provided in Fig. 6.14. The radii are provided in Table 6.7 and transition strengths and moments are supplied in Tables 6.8 and 6.9.

Our results for $^8$B are compared to the NCSM results of [99] in Fig. 6.15. The energy levels being compared here were obtained using a UCOM-transformed AV18 interaction with spin-orbit amplification factor 1. This is because we compare to the NCSM results obtained using an interaction (from chiral effective field theory) which is truncated at the two-body level [99]. Our results compare rather favourably, especially with regard to binding relative to the $^7$Be+p threshold.

**Table 6.7:** Calculated rms matter, charge, proton and neutron radii for the $^8$B ground state, from various basis sets. Labels as in Table 6.4.

| | $R_{matter}$ [fm] | $R_p$ [fm] | $R_n$ [fm] | $R_{charge}$[fm] |
|---|---|---|---|---|
| Exp. | 2.38(4) [40] | | | |
| V | 2.262 | 2.374 | 2.062 | 2.523 |
| V$_C$ | 2.298 | 2.420 | 2.078 | 2.567 |
| $R$ | 2.272 | 2.387 | 2.064 | 2.535 |
| $R_C$ | 2.269 | 2.386 | 2.060 | 2.534 |
| $R_{ext}$ | 2.285 | 2.387 | 2.102 | 2.536 |
| $R_{extC}$ | 2.282 | 2.389 | 2.091 | 2.537 |

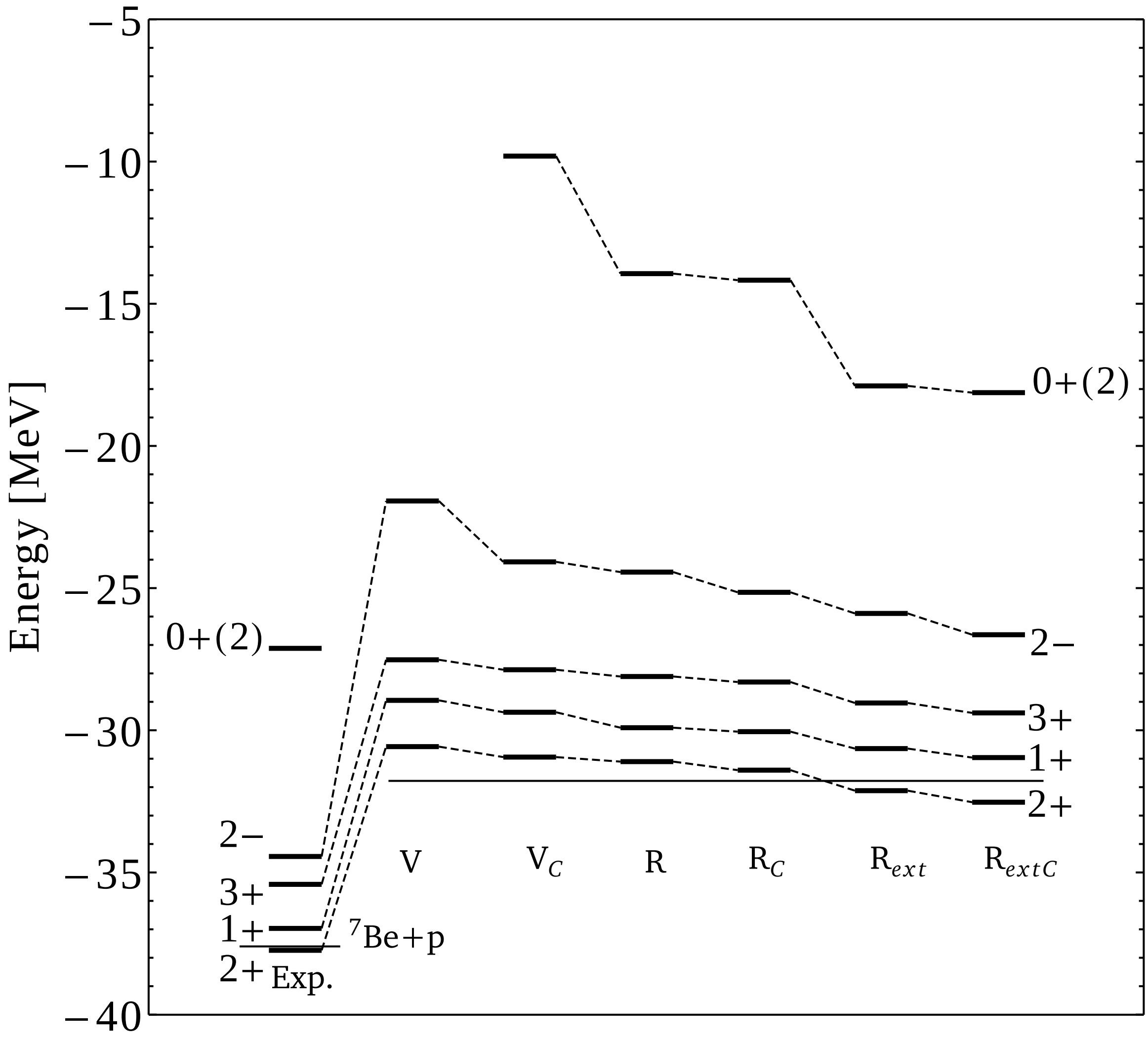

**Figure 6.14:** Level-scheme of $^8$B, comparing experimental and calculated ground and excited state energies for different FMD basis sets. Labels for the basis state are as in Table 6.4. The thin lines indicate the $^7$Be+p threshold in the experimental and calculated case.

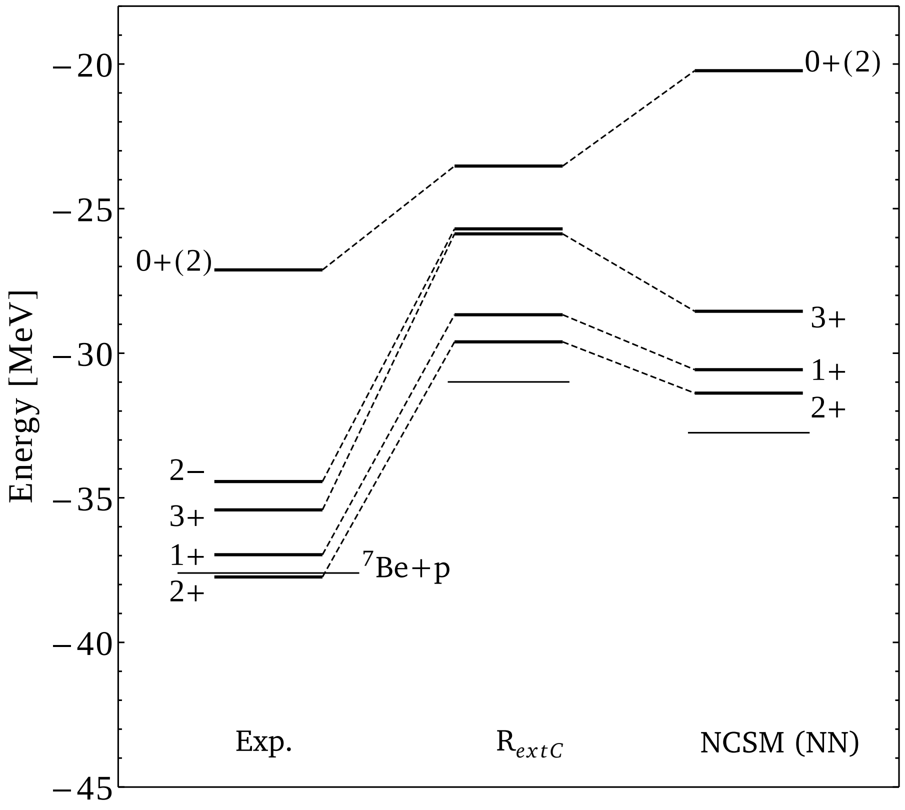

**Figure 6.15:** Level-scheme of $^8$B comparing our results ($R_{extC}$) to NCSM calculations of [99] (NCSM (NN)). The thin lines indicate the experimental and calculated $^7$Be+p thresholds. In order to compare to their calculations using two-body forces, we performed calculations using the UCOM-transformed AV18 with an *LS* term with an amplification of the *LS* term of 1. Note that [99] do not report a $2^-$ state.

**Table 6.8:** Calculated magnetic dipole moment $\mu$ and electric quadrupole moment $Q$ for the $^8$B ground state, from various basis sets. Labels as in Table 6.4. The numbers in brackets give the strength factor of the *LS* term in the interaction.

| | $\mu$ [$\mu_N$] | $Q$ [efm$^2$] |
|---|---|---|
| Exp. | 1.0355(3) [42] | 6.83(21) [38] |
| V (2.0) | 1.228 | 4.863 |
| $V_C$ (2.0) | 1.233 | 5.223 |
| $R_{ext}$ (2) | 1.194 | 5.064 |
| $R_{extC}$ (2) | 1.195 | 5.268 |
| $R_{ext}$ (1.5) | 1.392 | 5.739 |
| $R_{extC}$ (1.5) | 1.363 | 5.492 |

**Table 6.9:** Transition strengths calculated in $^8$B in different bases. Labels as in Table 6.4. Measured values from [99].

| States | Basis | Experimental energy [MeV] | Calculated Energy [MeV] (2.0) | Calculated Energy [MeV] (1.5) | Experimental $B(M1)$ [$\mu_N^2$] | Calculated $B(M1)$ [$\mu_N^2$] (2.0) | Calculated $B(M1)$ [$\mu_N^2$](1.5) |
|---|---|---|---|---|---|---|---|
| $1^+ \rightarrow 2^+$ | V | 0.77 | 1.627 | 1.470 | 4.71(21) | 3.992 | 3.451 |
| | $\mathrm{V}_C$ | | 1.577 | 1.401 | | 4.277 | 3.915 |
| | $\mathrm{R}_{ext}$ | | 1.480 | 1.098 | | 4.417 | 4.246 |
| | $\mathrm{R}_{ext}C$ | | 1.570 | 1.207 | | 4.385 | 4.267 |
| $3^+ \rightarrow 2^+$ | V | 2.32 | 3.054 | 3.683 | | 0.274 | 0.156 |
| | $\mathrm{V}_C$ | | 3.072 | 3.676 | | 0.272 | 0.152 |
| | $\mathrm{R}_{ext}$ | | 3.084 | 3.505 | | 0.322 | 0.158 |
| | $\mathrm{R}_{extC}$ | | 3.141 | 3.563 | | 0.323 | 0.172 |

## 6.6 $^7$Be core and threshold

For the cluster configurations, the $^7$Be nucleus, which comprised the core, was modelled with an unconstrained VAP state projected on $3/2^-$. The proton- and neutron-density for this configuration, and for the $^7$Be $1/2^-$ configuration, are shown in Fig. 6.16. Both the $3/2^-$ and $1/2^-$ states play a role as a core of $^8$B [24].

For calculating the $^7$Be threshold to which our $^8$B energies are compared in Fig. 6.14, a basis of matter-radius constrained $^7$Be states was created. It consisted of 14 radius-constrained VAP states (7 for each of the angular momenta considered) The basis size was chosen from convergence behaviour of the low-lying state energies after inclusion of radius-constrained states beyond $R = 3.3$ fm (as in Fig. 6.17).

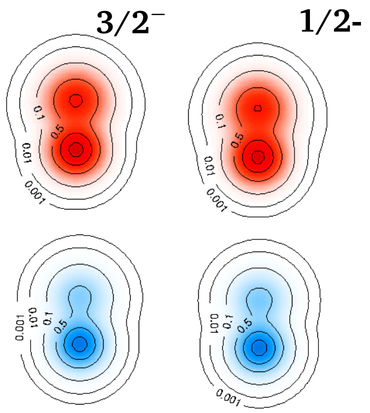

**Figure 6.16:** Proton- and neutron-densities of $^7$Be unconstrained VAP states. Numbers on the contour lines and to the right as in Fig. 6.16

.

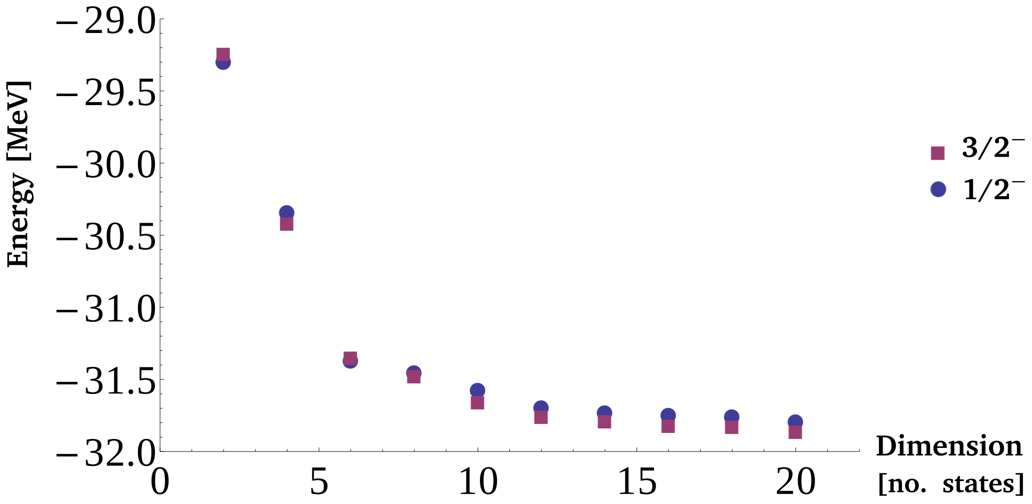

**Figure 6.17:** Energies of $^7$Be states, plotted with basis size, showing convergence behaviour near a basis of 14 basis states. The slight decrease in energy with 20 states is indicative of over-completeness of the basis.

## 6.7 $^9$Be

As in the preceding nuclei, the starting point is to make unconstrained VAP states. In the case of $^9$Be, states of angular momenta and parities $1/2^-$, $3/2^-$, $5/2^-$ and$1/2^+$ were projected out, since with an $^8$Be core (in a $0^+$ or $2^+$ state) and an odd neutron in the p-shell, $1/2^-$, $3/2^-$, $5/2^-$ states are all possible. In principle so is $7/2^-$, but experimentally this state lies rather high in energy and so basis states were not projected onto $7/2^-$. The $1/2^+$ state is the “missing” state in the $^9$Be-$^9$B pair, making it important to include configurations with $J^\pi = 1/2^+$ as well. Each proton and neutron was described spatially by a single Gaussian wave-packet. Proton- and neutron-densities for these four states are supplied in Fig. 6.18. Note that the structure appears to be $^5$He+$^4$He for the lower-lying states ($3/2^-$, $1/2^+$ and $5/2^-$), and for the $1/2^-$ state (which is only 38 keV below the $^5$He+$^4$He threshold [5]), the structure resembles $^8$Be+n. Diagonalising the Hamiltonian in this space gives energy levels provided in Fig. 6.20.

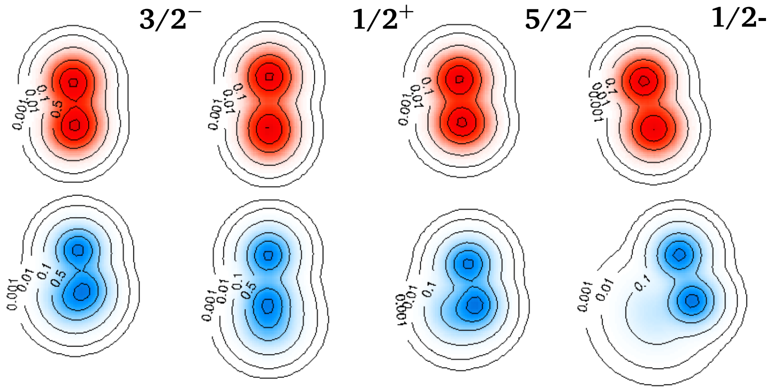

**Figure 6.18:** Proton- (red) and neutron-densities (blue) for the VAP basis configurations in $^9$Be. Numbers on the contour lines and to the right are as in Fig. 6.14. Note the configuration for the $1/2^+$ state, for comparison to that in mirror nucleus $^9$B (Figure 6.21).

To extend the basis, VAP states with constraints on matter radius between 2.1 and 3.3 fm (in steps of 0.2 fm) were used. As before, a basis size was chosen according to convergence behaviour of the energies of the low-lying states (Fig. 6.19). This gives 21 basis states (7 states each for angular momenta and parities

3/2⁻, 5/2⁻ and 1/2⁺). The Hamiltonian was diagonalised in this basis and the energies for the resulting eigenstates are shown in Fig. 6.20. Mirror configurations of the $^9$B basis states were then included, giving a basis set $R_{ext}$ of 42 basis states.

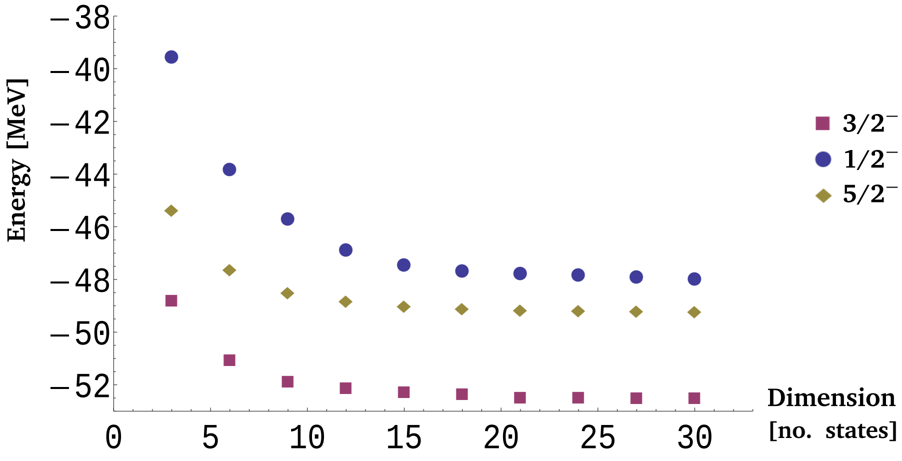

**Figure 6.19:** Energies of $^9$Be states, plotted with basis size, plotted with basis size of the *R*-constrained basis set, showing convergence behaviour near a basis set of 21 basis states.

Cluster basis states were made using an $^8$Be core in its $0^+$ state, plus a neutron. This represents the second-lowest threshold for decay by particle emission in $^9$Be, (with the lowest being $\alpha$+$\alpha$+n). The value of $r_{min}$ (defined in Equation (5.23)) was 2.5 fm, and so a separation of 5 fm was also used, giving 11 cluster basis states. The proton-and neutron densities of these configurations are provided in Table 40 in Appendix 4. The mirror configurations of the $^9$B clusters were added to this subset of cluster basis states. This was then added to the basis set of radius-constrained states, and the Hamiltonian was diagonalised therein. Energy levels are provided in Fig. 6.20, and radii, moments and transition strengths in all the bases are provided in Tables 6.10 to 6.12.

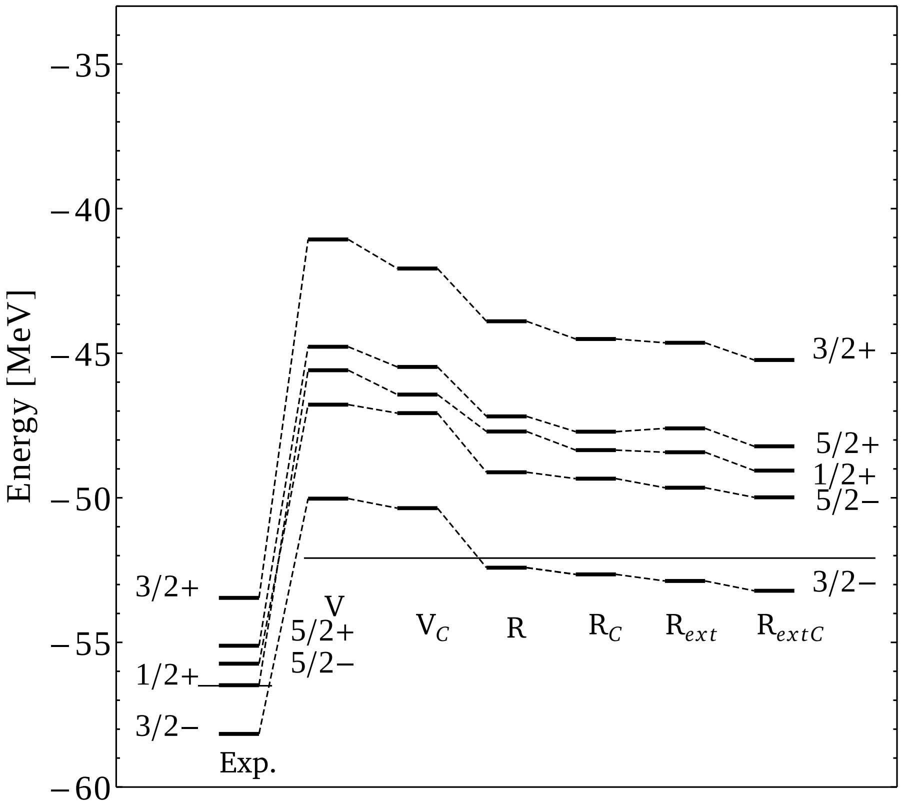

**Figure 6.20:** Level-scheme of $^9$Be, comparing experimental and calculated ground- and excited-state energies. The thin lines indicate the experimental and calculated $^8$Be+n threshold.

**Table 6.10:** Calculated rms matter, charge, proton and neutron radii for the $^9$Be ground state, from various basis sets. Labels as in Table 6.4.

| | $R_{matter}$ [fm] | $R_p$ [fm] | $R_n$ [fm] | $R_{charge}$ [fm] |
|---|---|---|---|---|
| Exp. | 2.38(1) [40] | | | 2.519(12) [80] |
| V | 2.291 | 2.236 | 2.334 | 2.377 |
| V$_C$ | 2.298 | 2.239 | 2.344 | 2.380 |
| R | 2.349 | 2.289 | 2.396 | 2.427 |
| R+C | 2.349 | 2.287 | 2.397 | 2.425 |
| R$_{ext}$ | 2.336 | 2.278 | 2.382 | 2.417 |
| R$_{extC}$ | 2.338 | 2.279 | 2.384 | 2.417 |

**Table 6.11:** Calculated magnetic dipole moment $\mu$ and electric quadrupole moment $Q$ for the $^9$Be ground state, in various basis sets. Labels as Table 6.7. The numbers in brackets give the strength factor of the $LS$ term in the interaction. Experimental value from [5] and [80].

| | $\mu$ $[\mu_N]$ | $Q$ [efm$^2$] |
|---|---|---|
| Exp. | -1.177432(3) | 5.288(38) |
| V (2.0) | -1.081 | 4.387 |
| V$_C$ (2.0) | -1.078 | 4.430 |
| $R_{ext}$ (2.0) | -1.026 | 4.788 |
| $R_{extC}$ (2.0) | -1.030 | 4.794 |
| $R_{ext}$ (1.5) | -1.119 | 5.055 |
| $R_{extC}$ (1.5) | -1.128 | 5.047 |

**Table 6.12:** Transition strengths $B(\Lambda M)$ calculated in $^9$Be in different bases. Labels as in Table 6.4. Measured values from [5].

| States | Basis | Experimental energy [MeV] | Calculated Energy [MeV] (2.0) | Calculated Energy [MeV] (1.5) | Experimental $B(E1)$ $[e^2]$ | Calculated $B(E1)$ $[e^2]$ (2.0) | Calculated $B(M1)$ $[e^2]$(1.5) |
|---|---|---|---|---|---|---|---|
| $1/2^+ \rightarrow 3/2^-$ | V | 1.684 | 4.440 | 4.043 | 0.21(9) | 0.018 | 0.026 |
| | V$_C$ | | 3.928 | 3.414 | | 0.015 | 0.022 |
| | R$_{ext}$ | | 4.451 | 3.621 | | 0.013 | 0.021 |
| | R$_{extC}$ | | 4.156 | 3.323 | | 0.012 | 0.020 |
| | | | | | Experimental $B(E1)$ $[e^2]$ | Calculated $B(E1)$ $[e^2]$ (2.0) | Calculated $B(E1)$ $[e^2]$(1.5) |
| $5/2^+ \rightarrow 3/2^-$ | V | 3.048 | 5.252 | 5.028 | 0.036(30) | 0.005 | 0.006 |
| | VC | | 4.884 | 4.582 | | 0.005 | 0.006 |
| | R$_{ext}$ | | 5.277 | 4.619 | | 0.007 | 0.009 |
| | R$_{extC}$ | | 5.005 | 4.342 | | 0.006 | 0.009 |
| | | | | | Experimental $B(E2)$ $[e^2fm^4]$ | Calculated $B(E2)$ $[e^2fm^4]$ (2.0) | Calculated $B(E2)$ $[e^2fm^4]$(1.5) |
| $7/2^- \rightarrow 3/2^-$ | V | 6.388 | 9.309 | 9.098 | 8.5(36) | 7.474 | 7.749 |
| | V$_C$ | | 9.349 | 9.136 | | 7.569 | 7.860 |
| | R$_{ext}$ | | 8.731 | 8.296 | | 9.473 | 11.182 |
| | R$_{extC}$ | | 8.786 | 8.365 | | 9.489 | 11.132 |

## 6.8 $^8$Be core and threshold

The core used in the $^9$Be cluster configurations was the $^8$Be nucleus, modelled with a single $0^+$ unconstrained VAP state. The proton- and neutron-density for this configuration is shown in Fig. 6.7. The value used for the $^8$Be threshold is the “full” $^8$Be ground-state energy (that is, the ground state energy as calculated for $^8$Be in the basis set $R_{ext}$). Comparison to threshold is rather unfavourable for $^9$B, therefore, since this basis set for $^8$Be consists of 104 basis states compared to only 42 for $^9$Be.

## 6.9 $^9$B

As in all the preceding nuclei, the first basis set consists of unconstrained VAP states, in this case, as in $^9$Be, projecting on angular momenta and parities $1/2^-$, $3/2^-$, $1/2^+$ and $5/2^-$. The reasoning here is the same as for $^9$Be: with a proton in a p-wave, and an $^8$Be core in a $0^+$ or $2^+$ state, $1/2^-$, $3/2^-$ and $5/2^-$ are all possible configurations, and we need the $1/2^+$ states to model the “missing” $1/2^+$ state. Each proton and neutron was described spatially by a single Gaussian wave-packet. Intrinsic proton- and neutron-densities for these configurations are supplied in Fig. 6.21. Diagonalising the Hamiltonian in this space gives energy levels provided in Fig. 6.23.

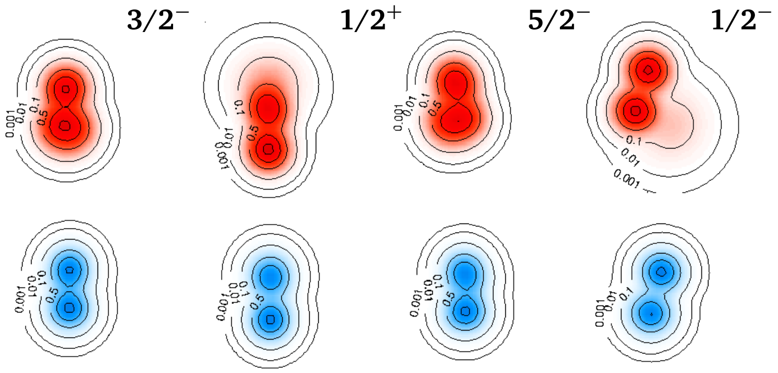

**Figure 6.21:** Intrinsic proton- (red) and neutron-densities (blue) for the VAP calculations for $^9$B. Numbers on the contour lines and to the right are as in Fig. 6.1. Note the intrinsic configuration for the $1/2^+$ state, which does not look like the proton-neutron mirrored configuration in $^9$Be (Figure 6.18).

The basis was extended with radius-constrained basis states. Constraints on matter radius were between 2.1 and 3.9 fm (in steps of 0.2 fm), and states with angular momenta and parities $3/2^-$, $5/2^-$ and $1/2^+$ were projected out. A basis set of 21 of such basis states was chosen according to convergence behaviour with basis size for the energies of the low-lying states (see Fig. 6.22). The mirror states of the $^9$Be radius-constrained configurations were added to this basis set, giving a set of 42 $R$-constrained basis states.

The cluster states were composed of an $^8$Be($0^+$) core plus a proton. The values of $r_{min}$ (defined in Eq.(5.23)) are also 2.5 fm and 5 fm, since the same core is used as in $^9$Be. The mirrors of the $^8$Be+n configurations were also added to this subset of states. Densities of these states are shown in Table 41 of Appendix 4. The Hamiltonian was diagonalised in all basis sets, and radii and electromagnetic moments are provided in Tables 6.13- 6.14. The only known transitions in $^9$B come from the high-lying $T=3/2$ levels, which were not included in our Hilbert space.

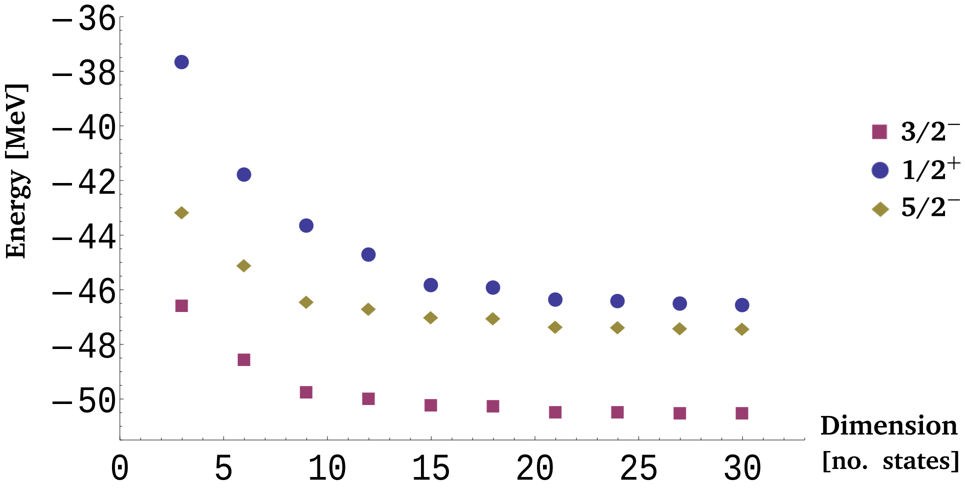

**Figure 6.22:** Calculated ground state energy of $^9$B states, plotted with basis size of the $R$-constrained basis set, showing convergence behaviour near a basis set of 21 basis states.

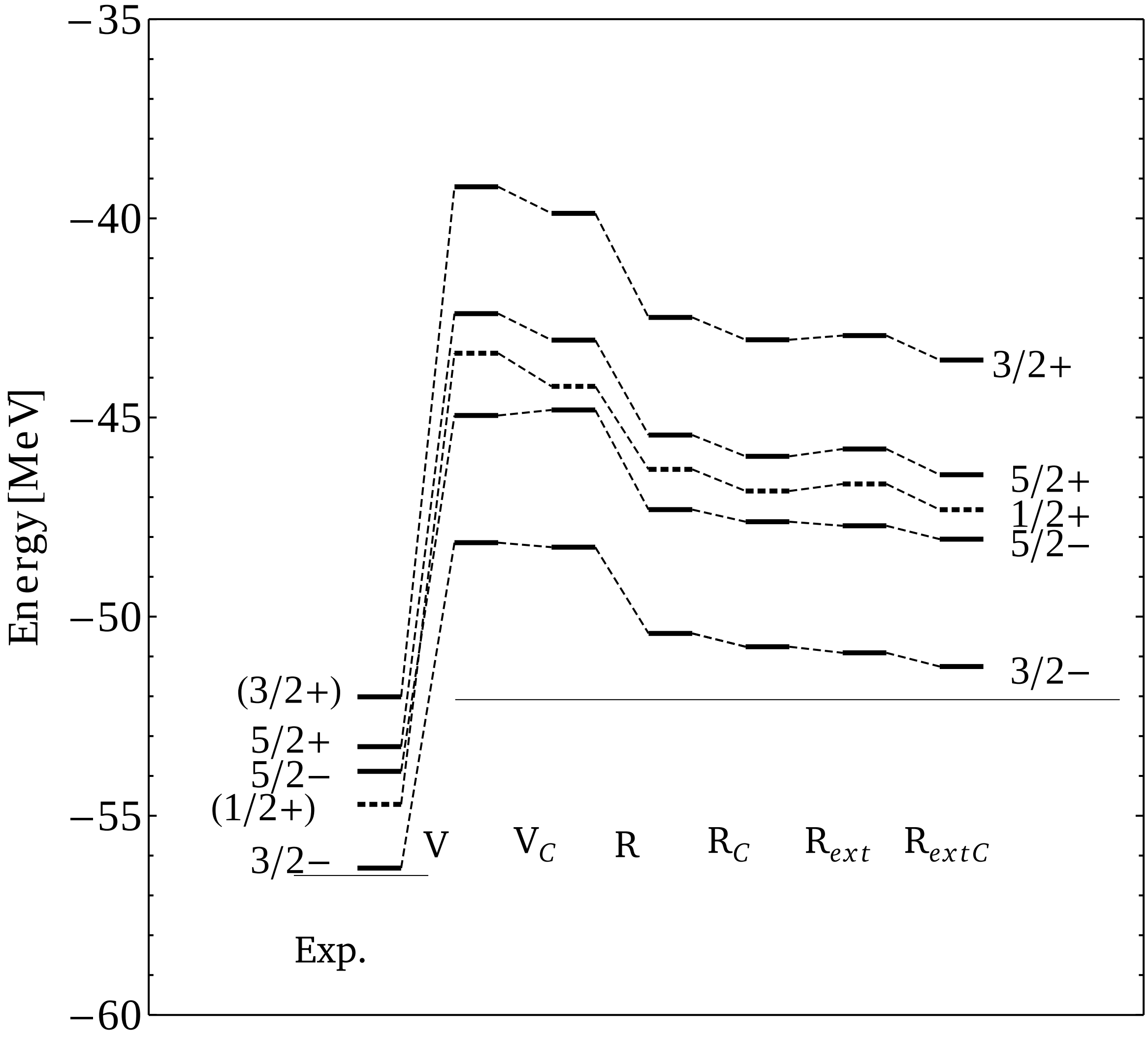

**Figure 6.23:** Level-scheme of $^9$B comparing experimental and calculated ground and excited state energies. Round brackets indicate that the spin and parity of the states is not well-known. Labels for the basis sets are as in Table 6.4. The thin line indicates the experimental and calculated $^8$Be+p threshold.

**Table 6.13:** Calculated rms matter, charge, proton and neutron radii for the $^9$B ground state, from various basis sets. Labels for the basis sets as in Table 6.4.

| | $R_{matter}$ [fm] | $R_p$ [fm] | $R_n$ [fm] | $R_{charge}$ [fm] |
|---|---|---|---|---|
| Exp. | - | | | |
| V | 2.304 | 2.362 | 2.230 | 2.507 |
| V$_C$ | 2.278 | 2.326 | 2.218 | 2.472 |
| $R$ | 2.368 | 2.425 | 2.295 | 2.567 |
| $R_C$ | 2.368 | 2.425 | 2.293 | 2.567 |
| $R_{ext}$ | 2.361 | 2.417 | 2.290 | 2.559 |
| $R_{extC}$ | 2.358 | 2.414 | 2.286 | 2.556 |

**Table 6.14:** Calculated magnetic dipole moment $\mu$ and electric quadrupole moment $Q$ for the $^{9}$B ground state, from various basis sets. Labels as Table 6.4. The numbers in brackets give the strength factor of the $LS$ term in the interaction.

| | $\mu$ [$\mu_N$] | $Q$ [efm$^2$] |
|---|---|---|
| Exp. | - | - |
| V (2.0) | 2.853 | 3.775 |
| V$_C$ (2.0) | 2.768 | 4.186 |
| $R_{ext}$ (2.0) | 2.814 | 4.380 |
| $R_{extC}$ (2.0) | 2.814 | 4.373 |
| $R_{ext}$ (1.5) | 2.926 | 4.401 |
| $R_{extC}$ (1.5) | 2.937 | 4.347 |

## 6.10 $^{10}$B

For $^{10}$B, as for all the preceding nuclei, one starts with unconstrained VAP states. In this case, states of angular momenta and parities $0^+$, $1^+$ and $3^+$ were projected out. For a $^{9}$B core in its $(3/2^-)$ state, and a neutron in the p-shell, states total spin and parity $0^+$ to $3^+$ are all possible. Only states of spin and parity $0^+$, $1^+$ and $3^+$ were projected out, as these correspond to the three lowest energy-levels in $^{10}$B. Each proton and neutron was described spatially by a single Gaussian wave-packet. Proton- and neutron-densities for these states are supplied in Fig. 6.24. Note the appearance of clustering in all three states. Diagonalising the Hamiltonian in this space gives energy levels provided in Fig. 6.27.

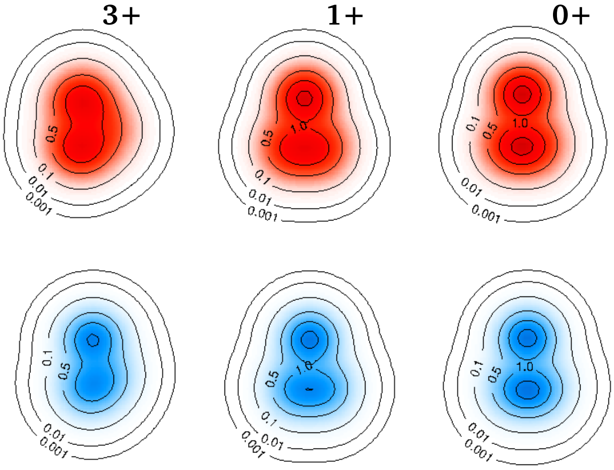

**Figure 6.24:** Intrinsic proton- (red) and neutron-densities (blue) for the VAP basis configurations for $^{10}$B. Numbers on the contour lines and to the right are as in Fig. 6.14.

As in all previous cases, constraints on the matter radius were used to extend the basis, and the size of the basis set chosen by checking convergence behaviour with basis size for the energies of the low-lying states, as shown as Fig. 6.25. The plot shows convergence behaviour around a basis set of 21 states. Energies calculated within this basis are provided in Fig. 6.27.

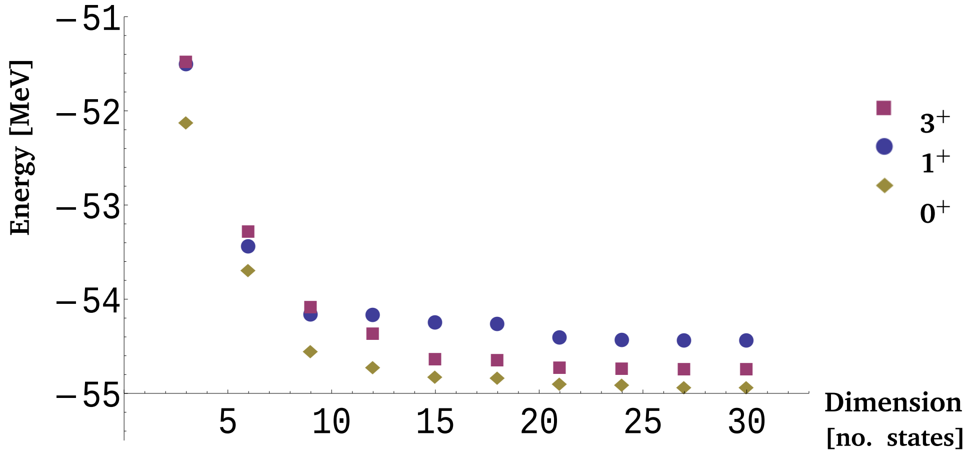

**Figure 6.25:** Energies of $^{10}$B states, plotted with basis size, showing convergence behaviour near a basis set of 21 basis states.

As the other characteristic property of $^{10}$B is its large quadrupole moment (8.472(56) e.fm$^2$), and the energies of the $^{10}$B states are clearly not well-reproduced in the radius constrained basis set alone (Fig. 6.27), it was decided to create also configurations with constraint on quadrupole moment $\langle Q \rangle$. In FMD, one does not constrain the quadrupole moment directly, but the constraint $Q$ is in fact on the square-root of the trace of the square of the quadrupole tensor, or:

$$Q = \sqrt{\mathrm{Tr}\,(\mathbf{Q} \cdot \mathbf{Q})}. \tag{6.3}$$

This is done because the square of the quadrupole tensor is rotationally-invariant.

These $Q$-constrained VAP basis states were also projected on $J^\pi$ of $3^+$, $1^+$ and $0^+$. These states were added to the $R$-constrained basis set (this whole set will be referred to as "R+Q" (as in 6.4)), and energies of the low-lying states were plotted to check for convergence behaviour, to choose a basis size. This plot is shown as Fig. 6.26, where one can see that energies start to converge near a basis of 42 basis states in total (21 radius-constrained basis states plus 21 $Q$-constrained basis states).

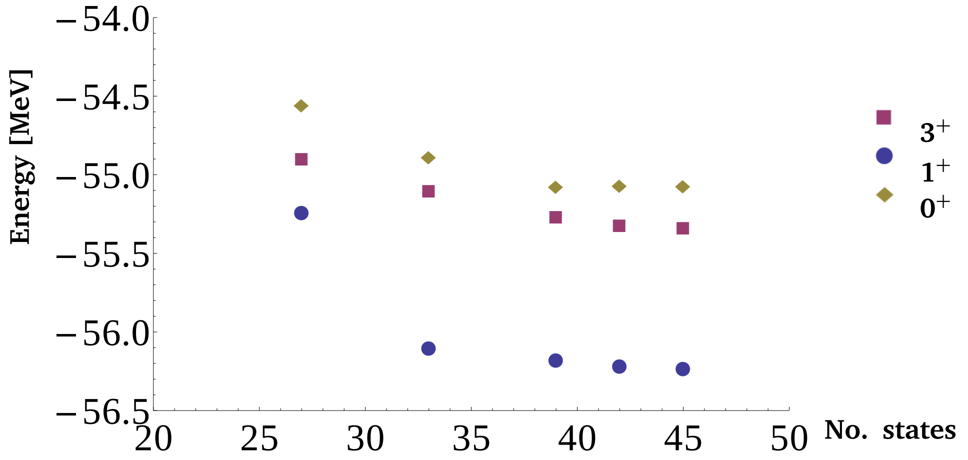

**Figure 6.26:** Energies of $^{10}$B states, plotted with basis size of the R+Q basis set, showing convergence behaviour near a basis set of 42 basis states.

Cluster states were also created for $^{10}$B. These consisted of $^6$Li plus $\alpha$ clusters, as the lowest-lying threshold for decay by particle emission is the $^6$Li+$\alpha$ threshold (4.460 MeV above the ground state). The value of $r_{min}$ (Eq.(5.23)) was 0.77 fm, and values of 1.54 fm were also used. This gives a total of 11 cluster basis states. The proton- and neutron-densities for these cluster states are provided in Table 42 in Appendix 4. These states were added to the set of the radius- and quadrupole-constrained states, (set $R+Q_C$) and the Hamiltonian was diagonalised in this Hilbert space. The energy levels calculated in this space are supplied in Fig. 6.27. The radii, moments and transition strengths are supplied in Tables 6.15-6.17.

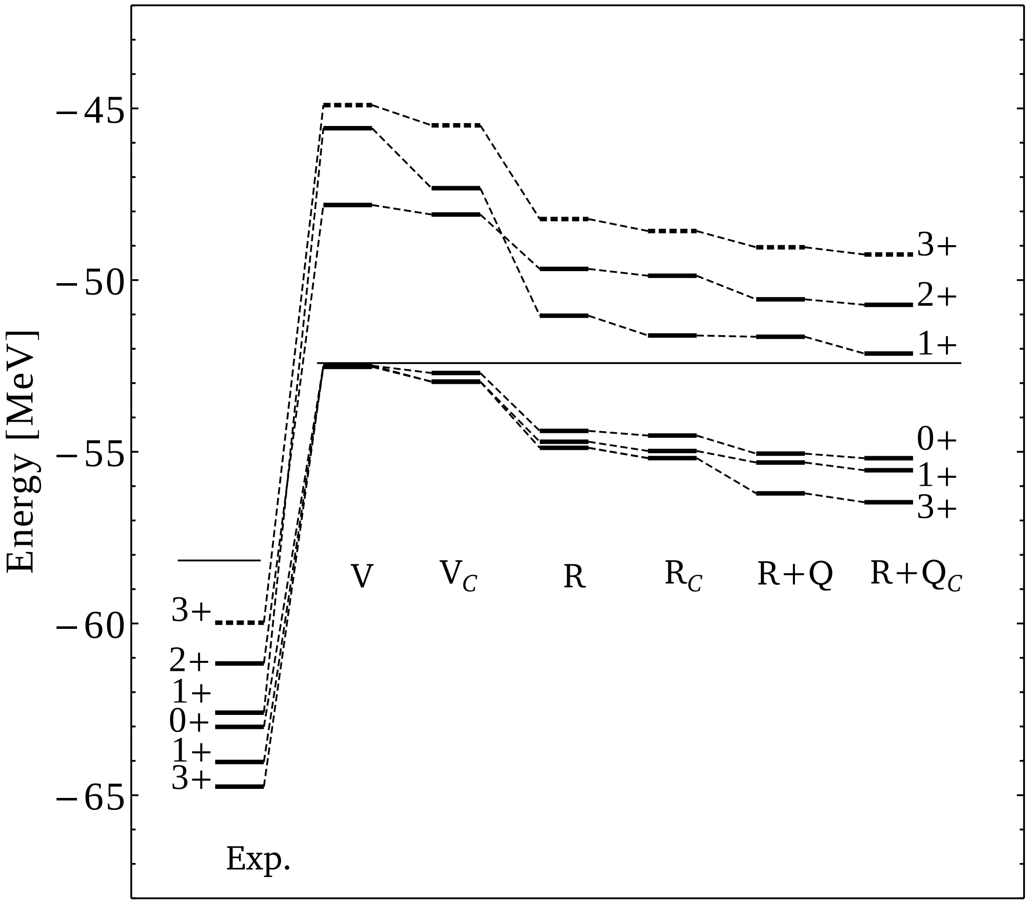

**Figure 6.27:** Level-scheme of $^{10}$B, comparing experimental and calculated ground and excited state energies in different basis sets. Labels for the six basis states are the same as those in Table 6.4. The thin lines indicate the experimental and calculated $^9$Be+p thresholds. Note that the ground state and the first $1^+$ state were almost-degenerate for the VAP basis sets.

**Table 6.15:** Calculated rms matter, charge, proton and neutron radii for the $^{10}$B ground state, from various basis sets. Labels as in Table 6.4. Experimental values from [40] and [101].

| | $R_{matter}$ [fm] | $R_p$ [fm] | $R_n$ [fm] | $R_{charge}$ [fm] |
|---|---|---|---|---|
| Exp. | 2.20(6) | | | 2.4277(499) |
| V | 2.193 | 2.198 | 2.187 | 2.348 |
| $V_C$ | 2.210 | 2.216 | 2.204 | 2.364 |
| R | 2.260 | 2.267 | 2.253 | 2.412 |
| $R_C$ | 2.262 | 2.264 | 2.260 | 2.409 |
| R+Q | 2.257 | 2.261 | 2.254 | 2.407 |
| R+$Q_C$ | 2.255 | 2.259 | 2.251 | 2.405 |

**Table 6.16:** Calculated magnetic dipole moment $\mu$ and quadrupole moment $Q$ for the $^{10}$B ground state, in various basis sets. Labels as Table 6.4. The numbers in brackets give the strength factor of the $LS$ term in the interaction. Experimental values from [5].

| | $\mu$ [$\mu_N$] | $Q$ [fm$^2$] |
|---|---|---|
| Exp. | 1.800065(1) | 8.472(56) |
| V (2) | 1.854 | 6.328 |
| $V_C$ (2) | 1.866 | 6.341 |
| R (2) | 1.849 | 7.442 |
| $R_C$ (2) | 1.863 | 7.410 |
| R+Q (2) | 1.852 | 7.834 |
| R+$Q_C$ (2) | 1.854 | 7.805 |
| R+Q (1.5) | 1.859 | 8.004 |
| R+$Q_C$ (1.5) | 1.863 | 7.952 |

**Table 6.17:** Transition strengths $B(\Lambda M)$ calculated in $^{10}$B in different bases. Labels as in Table 6.4. Measured values from [5].

| States | Basis | Experimental energy [MeV] | Calculated Energy [MeV] (2.0) | Calculated Energy [MeV] (1.5) | Experimental $B(M1)$ [$\mu_N^2$] | Calculated $B(M1)$ [$\mu_N^2$] (2.0) | Calculated $B(M1)$ [$\mu_N^2$](1.5) |
|---|---|---|---|---|---|---|---|
| $1^+ \rightarrow 3^+$ | V | 0.718 | 0.036 | 0.601 | 0.835 | 1.093 | 0.959 |
| | $V_C$ | | 0.002 | 0.747 | | 1.098 | 0.974 |
| | R+Q | | 0.899 | 0.533 | | 2.152 | 0.481 |
| | R+$Q_C$ | | 0.931 | 0.587 | | 2.175 | 0.404 |
| | | | | | Experimental $B(E2)$ [$e^2fm^4$] | Calculated $B(M1)$ [$e^2fm^4$] (2.0) | Calculated $B(M1)$ [$e^2fm^4$](1.5) |
| $0^+ \rightarrow 1^+$ | V | 1.021 | 0.001 | 0.198 | 7.392 | 11.735 | 13.205 |
| | $V_C$ | | 0.254 | 0.047 | | 11.776 | 13.629 |
| | R+Q | | 1.158 | 1.091 | | 12.421 | 13.753 |
| | R+$Q_C$ | | 1.282 | 1.170 | | 12.521 | 13.897 |

## 7 Discussion

The results obtained for each nucleus are discussed in detail in Sections 7.1-7.6. Observations for the $A$=8 and $A$=9 isomultiplets are discussed in Section 7.7 and 7.8. Results for the boron isotopic chain are compared and discussed in Section. 7.9.

### 7.1 $^8$Li

The energy levels and other observables for $^8$Li are quite well-reproduced in the $^8$Li basis set ($\mathrm{R}_{ext}C$) compared to experiment (Fig. 6.3 and Table 6.1-6.3). The energy levels also compare well with those from the No-Core Shell Model (Fig. 6.4), especially as regards binding relative to threshold, which is about equally well-reproduced in both cases.

The inclusion of cluster configurations does have an effect on the calculated energy levels: in Fig. 6.3, one can see that the binding of the ground state, $1^+_1$ and $3^+_1$ states is improved (by about 0.3 MeV) by the inclusion of cluster configurations in the $\mathrm{R}_{ext}$ basis set. This inclusion of cluster states affects the $1^+_2$ state a little more (binding is improved by 0.655 MeV). Naïvely one would expect it to lower the energy of the $3^+$ state more, since it lies at the $^7$Li+n threshold, while the $1^+_2$ state lies about halfway between the $^7$Li+n threshold and the $^4$He+t+n threshold. Perhaps the “extended” $^7$Li+n configurations are already included in $\mathrm{R}_{ext}$ basis set (as mirrors to the $^8$B halo states), meaning that the $^7$Li+n states do not contribute much new structure to the $3^+$ state.

Concerning reproduction of transition strengths and moments (Tables 6.3 and 6.2), both the $1^+_1 \rightarrow 2^+$ and $3^+ \rightarrow 2^+$ transitions are better-reproduced *before* the addition of cluster configurations (Table 6.2). A possible explanation is that the magnetic dipole moment of the $^8$Li $1^+$ and $3^+$ states arise from a deformed $^7$Li core. If the core is in a superposition of the $^7$Li $3/2^-$ and $1/2^-$ state it will be more deformed, since the $1/2^-$ is more deformed than the $3/2^-$ state, lying closer to the $\alpha$+$^3$H threshold [5]. In our cluster configurations, only the $3/2^-$ state of the $^7$Li core was considered. This means the core in our cluster configurations is less deformed than it ought to be, and this may reduce the magnetic dipole moment of these cluster configurations. If this is correct, one can conclude that $^7$Li($1/2^-$) may be important in the reproduction of the $S$ factor for $^7$Li(n,$\gamma$)$^8$Li, as already suggested by [36].

When selecting a spin-orbit strength for $^8$Li, one may note (in Tables 6.1 to 6.2) that all radii, and also the energy and strength of the 0.980 MeV $M1$ transition ($1^+_1 \rightarrow 2^+_1$), are better-reproduced with a spin-orbit term of strength 1.5. The energy of the 2.225 MeV $M1$ transition ($3^+_1 \rightarrow 2^+_1$) is better-reproduced with the spin-orbit strength of 2. We can see in Table 7.1 that reducing the strength of the spin-orbit term *increases* the magnitude of the magnetic dipole moment of the $1^+_1$ state by about 0.1 $\mu_N$, but *decreases* the magnitude of the magnetic dipole moment of the and $3^+_1$ state by about 0.1 $\mu_N$ (Table 7.1). This leads to enhancement of the $1^+_1 \rightarrow 2^+_1$ strength, but suppression of the $3^+_1 \rightarrow 2^+_1$ strength. Our model is more accurate in reproducing the low-lying nuclear states (being a bound-state approximation). The spin-orbit strength of 1.5 does better in reproducing the $1^+_1 \rightarrow 2^+_1$ transition (which connects the lowest-lying state to the ground state). Thus we consider that a spin-orbit term of strength 1.5 is best suited to $^8$Li, since the energy of the $3^+_1$ state is in any case not as well-reproduced in the model.

**Table 7.1:** Magnetic dipole moments of first and second excited states of $^8$Li, calculated with different spin-orbit strengths.

| Basis | $\mu$ of ground state $[\mu_N]$ | $\mu$ of $1_1^+$ state $[\mu_N]$ | $\mu$ of $3_1^+$ state $[\mu_N]$ |
|---|---|---|---|
| Exp. | 1.653560(18) | - | - |
| $R_{ext}$ (2) | 1.480 | -2.411 | 2.316 |
| $R_{extC}$ (2) | 1.477 | -2.408 | 2.302 |
| $R_{ext}$ (1.5) | 1.299 | -2.566 | 2.191 |
| $R_{extC}$ (1.5) | 1.296 | -2.569 | 2.159 |

## 7.2 $^8$Be

Results for the energy levels of $^8$Be also compare very favourably with the NCSM results of [99] (Fig. 6.11), especially as regards binding with respect to the 2 $\alpha$ threshold.

The reproduction of the $T=1$ states in $^8$Be is of special interest. It was found that, of the two basis sets (that with constraints on isospin and spin (basis T+S$_C$) and that using the isospin partner configurations from $^8$Li and $^8$B ($R_{extC}$), the one using the isospin partner states ($R_{ext}$) does a far better job in reproducing energies of $T=1$ states (Fig. 6.10). This is unsurprising given that the set of mirror states is an order of magnitude larger than the set of spin- and isospin-constrained basis states. This shows that there are high-energy configurations for $^8$Be missing from the $T+S+$C basis set, which are included in the set with $^8$Li, $^8$B isospin partner configurations.

Another area of interest in $^8$Be is the isospin-mixed $2^+$ states (denoted $2^+(0+1)$), which occur experimentally at 16.626 and 16.922 MeV above the ground state. The coefficients $\alpha_2$ and $\beta_2$ for isospin-mixing in this pair of $2^+$ states are defined as [102]:

$$\begin{aligned} |\Psi_a\rangle = &\quad \alpha_2|\phi_0\rangle + \beta_2|\phi_1\rangle \\ |\Psi_b\rangle = &\quad \beta_2|\phi_0\rangle - \alpha_2|\phi_1\rangle. \end{aligned} \tag{7.1}$$

where $E_a \leq E_b$, the subscript 2 on $\alpha$ and $\beta$ denotes the angular momentum $J$ of the states, the $|\Psi_a\rangle$ and $|\Psi_b\rangle$ are the two $2^+$ states, and the states $|\phi_{0,1}\rangle$ are states of good isospin. The value of $\alpha_2$ was determined experimentally by [102] via comparing the cross sections for single-nucleon transfer to these mixed states to cross sections for the same transfer to an analogous state of pure isospin (in this case the $J^\pi(T)=2^+(1)$ state in $^8$Li). By this method, they obtain a coefficient $\alpha_2$ of 0.81±0.01. Through

$$\begin{aligned} \langle\Psi_a|\hat{\vec{T}}^2|\Psi_a\rangle = &\quad 2\left(1-|\alpha_2|^2\right) \\ \langle\Psi_b|\hat{\vec{T}}^2|\Psi_b\rangle = &\quad 2|\alpha_2|^2, \end{aligned} \tag{7.2}$$

this value of $\alpha_2$ gives $\langle\hat{\vec{T}}^2\rangle \approx 1.31$ for the higher-lying state, and $\langle\hat{\vec{T}}^2\rangle \approx 0.69$ for the lower-lying state.

As a perturbative effect, the magnitude of the isospin-mixing depends on the energy difference of the two $2^+(0+1)$ states. In our results, this energy difference is 1.133 MeV (experimentally it is 0.296 MeV). Thus it is unsurprising that our results demonstrate less isospin-mixing, giving $\langle\hat{\vec{T}}^2\rangle = 1.934$ for the lower-lying state, and $\langle\hat{\vec{T}}^2\rangle = 0.096$ for the higher-lying state. Nonetheless, we get isospin-mixing in these states, which is not achieved in the latest No Core Shell Model results [99], in which the lower-lying state is isospin-zero, and the higher-lying state is isospin 1. It is discussed in [102] that these $2^+(0+1)$ states have a large overlap with $^7$Li+p and $^7$Be+n configurations, which may explain the difficulty of reproducing them in the shell model calculations, since it would mean they were based on a cluster structure.

In $^{8}$Be, the effect of increasing the magnitude of the spin-orbit term is also of interest. This is because the $T=1$ states are more compact, and will thus be affected more strongly by three- and higher-body forces. The effect of these forces is included via an increased strength of the spin-orbit term. We initially calculate the energies with a spin-orbit strength factor of 2 results in Fig. 6.10). The factor was changed to 3, 3.5 and 4, and these Hamiltonians were diagonalised in the "R$_{extC}$" basis set. The energy levels obtained are plotted in Fig. 7.1. It can be seen that increasing the strength of the spin-orbit term lowers the energy of the $T=1$ state energies, and also increases the binding-energy of the ground state. However, an effect of increasing the strength of the spin-orbit term is to unrealistically lower the energy of the $T=0$ states, which also upsets the transition energies between these states: the $2^+ \rightarrow 0^+$ transition is experimentally 3.03 MeV, with a spin-orbit strength factor of 3 it is 3.367 MeV, and with a spin-orbit term of strength 4 it is 2.284 MeV; more than 0.5 MeV too low. Likewise for the $4^+ \rightarrow 2^+$ state, which is experimentally 8.047 MeV, is 7.891 MeV with a spin-orbit strength factor of 3, but is 6.919 MeV (more than 1 MeV too low) with a spin-orbit strength factor 4.

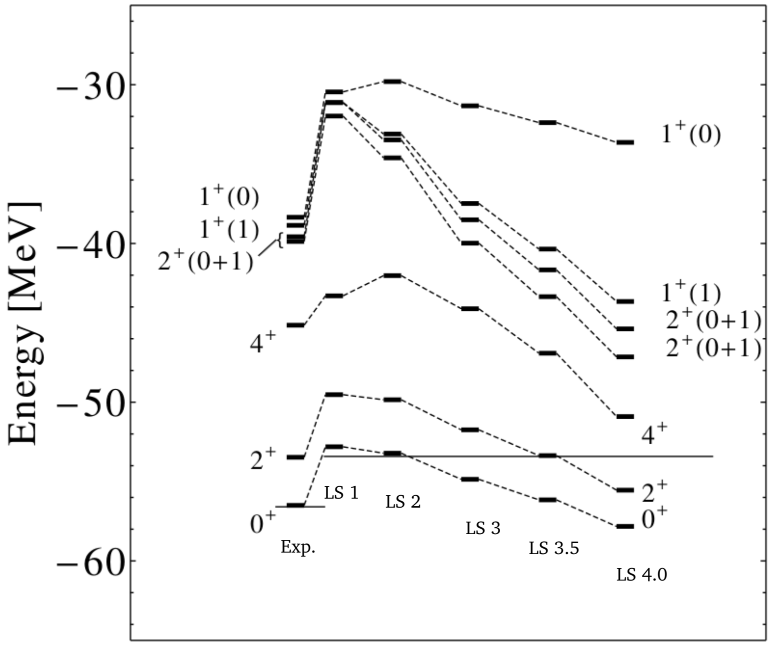

**Figure 7.1:** Level-scheme of $^{8}$Be, comparing experimental and calculated ground and excited state energies when the strength of the spin-orbit term is amplified. Labels below indicate the factor in front of the spin-orbit term. The effect of the strength on binding is The Hamiltonians were each diagonalised in the "R$_{extC}$" basis set defined in Table 6.4.

As regards the spin-orbit strength, it is interesting to note that a stronger spin-orbit term (of strength 3) reproduces the energies of the $T=1$ states far better (Fig. 7.1). This is unsurprising, given that these states are spatially compact in comparison to the $T=0$ states (based on $\alpha$ clusters), and thus the three- and higher-body terms may be significant, simply because the particles are all in closer proximity. However, increasing the strength of the spin-orbit term also alters the reproduction of radii and transition strengths and energies. Energy of the transition from the $1^+_1(1)$ state to the ground state is better reproduced in the R$_{ext}$ basis set with a spin-orbit strength factor of 2 (experimentally, the energy of this transition is 17.640 MeV. A spin-orbit amplification of 2 gives an energy of 16.940 MeV in the R$_{ext}$ basis, which is reduced to an energy of 14.258 when a spin-orbit strength of 3.0 is used). We can conclude that while increasing the strength of the spin-orbit term improves reproduction of the $T=1$ states, it does not improve the energies of the $^8$Be $T=0$ states.

**Table 7.2:** Calculated rms matter, charge, proton and neutron radii for $^8$Be using different spin orbit strength factors. Labels as in Table 6.4.

| | $R_{matter}$ [fm] | $R_p$ [fm] | $R_n$ [fm] | $R_{charge}$ [fm] |
|---|---|---|---|---|
| $R_{ext}$ (2.0) | 2.404 | 2.408 | 2.400 | 2.545 |
| $R_{ext}$ (3.0) | 2.278 | 2.282 | 2.274 | 2.427 |

## 7.3 $^8$B

The energy levels and other observables of $^8$B are fairly well-reproduced in the model (Fig. 6.14 and Table 6.7-6.9), and comparison to the NCSM calculations of [99] is not unfavourable (Fig. 6.15). A matter of particular interest is the proton point radius of $^8$B, which we conclude to be 2.389 fm. This is 0.1 fm larger than our calculated matter radius and $\approx$ 0.2 fm larger than the calculated neutron radius. This means that we reproduce a slight proton-halo in the ground state of $^8$B. The calculated matter radius is in itself in excellent agreement with the current measured value of 2.38(4) fm.

Reproduction of the $^8$B energy levels is rather good except for energy of the second excited $1^+$ and $2^+$ states, which our calculations place rather high in energy compared to experiment (Fig. 6.14). This is steadily improved as the basis size is increased. It can be seen also in the no-core shell-model study [99] that the reproduction of these levels depends strongly on model-space size, with all three tending to "bunch" (the same as in our study) when the model-space is reduced. The width of these states is not known experimentally [5], but this large dependence of their energy on model-space size suggests that these states are rather broad.

One may note that addition of cluster configurations reduces the magnetic dipole moment of the low-lying states (see Table 6.8 and Table 7.3), especially when the spin-orbit term is reduced. The same trend was observed in the moments of $^8$Li (se Table 6.2). As in the $^8$Li case, one can argue that our cluster states reduce the magnetic dipole moment of the excited states because only the $^7$Be($3/2^-$) core is included, while it should be in a superposition of the ($3/2^-$) and ($1/2^-$) states as shown by [24, 36]. Like in $^7$Li, the $^7$Be $1/2^-$ state can be expected to be more deformed than the $3/2^-$ state, as it lies closer to the $^4$He+$^3$He threshold [103]. Leaving out the $1/2^-$ state of the $^7$Be core thereby reducing the magnetic dipole moment of the excited states.

Transition strengths are well-reproduced in the full basis, with the magnitude of the $1_1^+ \rightarrow 2_1^+$ transition coming within 0.7 $\mu_N$ of the experimental value when a spin-orbit strength of 2 is used. One can therefore conclude that a spin-orbit term of strength 2 is best for $^8$B.

**Table 7.3:** Magnetic dipole moments of the first and second excited states of $^8$Li, as calculated with different spin-orbit strengths.

| Basis | $\mu$ of ground state [$\mu_N$] | $\mu$ of $1_1^+$ state [$\mu_N$] | $\mu$ of $3_1^+$ state [$\mu_N$] |
|---|---|---|---|
| Exp. | 1.0355(3) | - | - |
| $R_{ext}$ | 1.194 | 3.526 | 1.342 |
| $R_{extC}$ | 1.195 | 3.533 | 1.351 |
| $R_{ext}$ 1.5 | 1.392 | 3.683 | 1.530 |
| $R_{extC}$ 1.5 | 1.363 | 3.710 | 1.534 |

The energy levels of $^9$Be are fairly well-reproduced in the model when compared to experiment (Fig. 6.20 and Table 6.10-6.12). The $1/2^+$ state is somewhat higher in energy than in experiment, and in our results lies above the $5/2^-$ state. The $1/2^+$ state is rather broad (width 0.217(10) MeV) and is also 19 keV above the $^8$Be+n threshold, meaning that it has a complicated cluster structure. Using a spin-orbit strength factor of 1.5 helps to reproduce this loosely-bound structure, and somewhat improves reproduction of the $1/2^+$ state. Three- and higher-body correlations likely play less of a role in this state simply because the nucleons are not all in close proximity, explaining the improvement with a reduced spin-orbit strength.

It is interesting to note that radii of the $^9$Be ground state are also better-reproduced with a reduced spin-orbit strength in $^9$Be: Table 7.4 compares radii calculated with different spin-orbit strengths, and one may note that the matter radius calculated in the full basis using a spin orbit strength factor of 1.5 is within 0.03 fm of experiment. The charge radius calculated in this basis is rather extended (2.469 fm), which is within 0.5 fm of the meausured value for charge radius supplied by [80].

**Table 7.4:** Calculated rms matter, charge, proton and neutron radii for the $^9$Be ground state using different spin orbit strength factors. Labels as in Table 6.4.

| | $R_{matter}$ [fm] | $R_p$ [fm] | $R_n$ [fm] | $R_{charge}$ [fm] |
|---|---|---|---|---|
| Exp. | 2.38(1) [40] | - | - | 2.519(12) [80] |
| $R_{ext}$ (2.0) | 2.336 | 2.278 | 2.382 | 2.417 |
| $R_{extC}$ (2.0) | 2.338 | 2.279 | 2.384 | 2.417 |
| $R_{ext}$ (1.5) | 2.411 | 2.336 | 2.469 | 2.472 |
| $R_{extC}$ (1.5) | 2.409 | 2.334 | 2.468 | 2.469 |

The energy and strength of the $E2$ transition from $7/2^-_1 \rightarrow 3/2^-_1$ is rather well-reproduced in our model in the full basis set (Table 6.12). Interestingly, reducing the spin-orbit strength factor to 1.5 (from 2.0) improves reproduction of the transition energy, but over-enhances the strength of the transition by approx 3 $e^2fm^4$. Addition of $^8$Be+n cluster configurations to the basis raises the transition energy compared to experiment (by about 70 keV when a reduced spin orbit strength is used), but lowers the transition strength by 0.05 $e^2fm^4$, bringing it a little closer to the experimental value. The $7/2^-$ state is probably based on the odd neutron in the f 7/2 orbit. The ground state electromagnetic moments are also better-reproduced with an $LS$ term with coefficient 1.5 (see Table 6.12 and Table 7.5)). These higher-lying states derive their properties from the properties of the valence neutron, and its angular momentum is strongly influenced by the spin-orbit term.

Considering transition strengths, moments and radii, one can conclude that a spin-orbit strength of 1.5 is favourable for $^9$Be.

**Table 7.5:** Electromagnetic moments of the higher-lying states of $^9$Be. The values for the "complete" basis $R_{ext}C$ are given, with different strength factors of the spin-orbit term. The values of the strength factor are supplied in brackets.

| State | $\mu$ [$\mu_N$] | | $Q$ [e.fm$^2$] | |
|---|---|---|---|---|
| | $R_{extC}$ (2.0) | $R_{extC}$ (1.5) | $R_{extC}$ (2.0) | $R_{extC}$ (1.5) |
| $5/2^-$ | -0.472 | -0.663 | -2.392 | -2.724 |
| $1/2^+$ | -1.815 | -1.854 | 0.000 | 0.000 |
| $5/2^+$ | -1.423 | -1.428 | -8.844 | -9.070 |
| $1/2^-$ | 0.839 | 0.835 | 0.000 | 0.000 |
| $7/2^-$ | 0.378 | 0.097 | -6.571 | -7.471 |

## 7.5 $^{9}$B

As there is very little data on $^{9}$B besides its level-scheme, the results can only be assessed on their reproduction of level-energies, which appears to be satisfactory (see Fig. 6.23).

As in $^{9}$Be, the ordering of the $1/2^{+}$ and $5/2^{-}$ states is swapped. The level at 1.6 MeV which is presumed to be the “missing” $1/2^{+}$ state in $^{9}$B has a width of 3.130(200) MeV, however, so reproducing it is challenging, particularly in a model space of 21 states. In contrast, the $5/2^{-}$ state is 0.081(5) MeV in width, and is easier to reproduce accurately.

One may infer from reproduction of the energy-levels that a spin-orbit term of strength factor 2 is more appropriate for $^{9}$B (Table 7.6). The energy of the predicted $1/2^{+}$ state is lowered by 0.774 MeV when a reduced spin-orbit strength is used.

**Table 7.6:** Energies of the low-lying states of $^{9}$B, calculated with different values of spin-orbit strength factor, and with and without addition of clustering configurations. Energies are provided relative to ground state, and absolute energies are provided in round brackets in each case.

| Level | Energy ($R_{ext}$ (2)) [MeV] | Energy ($R_{extC}$ (2)) [MeV] | Energy ($R_{ext}$ (1.5)) [MeV] | Energy ($R_{extC}$ (1.5)) [MeV] | Energy (Exp.) [MeV] |
|---|---|---|---|---|---|
| $3/2_1^-$ | 0 (-50.909) | 0 (-51.253) | 0 (-49.320) | 0 (-49.687) | 0 (-56.314) |
| $1/2_1^+$ | 4.240 (-46.669) | 3.938 (-47.315) | 3.438 (-45.882) | 3.146 (-46.541) | 1.6 (-54.714) |
| $5/2_1^-$ | 3.190 (-47.719) | 3.198 (-48.055) | 2.978 (-46.342) | 2.991 (-46.696) | 2.345 (53.969) |
| $5/2_1^+$ | 5.118 (-45.791) | 4.816 (-46.437) | 4.490 (-44.830) | 4.205 (-45.482) | 2.751 (54.563) |
| $3/2_1^+$ | 7.966 (-42.943) | 7.696 (-43.557) | 6.858 (-42.462) | 6.578 (-43.109) | 4.800 (51.514) |

## 7.6 $^{10}$B

Energy levels of $^{10}$B are ordered in the same order as seen in experiment, although levels are somewhat under-bound compared to experiment (Fig. 6.27). The transition strengths and radii compare rather well with experiment (Tables 6.15-6.17).

The ground state radii of $^{10}$B are fairly well-reproduced in our model in the full basis R+Q+C (Table 6.15). Comparison of radii along the boron isotopic chain is thus valid, since radii of all the boron isotopes here studied seem well-reproduced with respect to experiment.

The plots of neutron- and proton-density for the unconstrained VAP states (Fig.6.24 are interesting: naïvely one would not expect clustering in the ground state, since the first threshold for decay by particle emission, the $^6$Li+$\alpha$ threshold, lies $\approx$ 4.5 MeV away from the ground state. The clustering we see in our unconstrained VAP states is probably this $^6$Li+$\alpha$ clustering.

In the level-scheme (Fig. 6.27) we see that the reproduction of the ground state and the first $1^+$ and $0^+$ states is rather drastically improved by inclusion of states with a constraint on quadrupole moment. The binding of the ground state improves by $\approx$ 0.6 MeV for all these states, and the spacing of the $1^+$ and $0^+$ state is improved. These two states are very broad indeed, (with lifetimes of 1.020±0.005 ns and 7±3 fs respectively), which explains their improvement with increased size of the model space! The first $0^+$ state is also a $T=1$ state, which would require “breaking” of the $^6$Li+$^4$He clustering.

Table 7.7 shows that moments of the higher-lying states differ rather markedly with change of the coefficient of the $LS$ term. This also shows in the reproduction of the transition strengths from these levels (Tab. 6.17). The higher-lying states are all $T=0$, except for the first $0^+$ state which is $T=1$, and which interestingly has zero magnetic dipole moment or electric quadrupole moment in our calculations. This suggests that the $^6$Li+$\alpha$ structure is broken in the $T=1$ first excited $0^+$ state, which in turn means that the large quadrupole moment of the $^{10}$B ground state is probably based on a $^6$Li+$\alpha$ clustering, or some other cluster structure, as is shown in the VAP density plots of $^{10}$B. this is interesting for a stable ground state which is $\approx$ 4 MeV below the nearest threshold for decay by particle emission.

**Table 7.7:** Moments of the higher-lying states in $^{10}$B calculated with different coefficients of the spin-orbit term. The spin-orbit strength factors are given in brackets.

| State | $\mu$ [$\mu_N$] | | $Q$ [e.fm$^2$] | |
|---|---|---|---|---|
| | R+Q (2.0) | R+Q (1.5) | R+Q$_C$ (2.0) | R+Q$_C$ (1.5) |
| $1^+$ | 0.748 | 0.847 | -2.701 | -1.099 |
| $0^+$ | 0.000 | 0.000 | -0.000 | -0.000 |
| $1^+$ | 0.484 | 1.203 | 0.583 | -1.458 |
| $2^+$ | 1.711 | 1.203 | -4.823 | -1.592 |
| $3^+$ | 1.823 | 1.848 | -7.013 | -8.125 |

Figure 7.2 shows the calculated energy levels for the $A = 8$ isotriplet nuclei plotted with the experimental levels on the same scale. We can see that relative binding of the isotriplet nuclei follows the same pattern as in experiment.

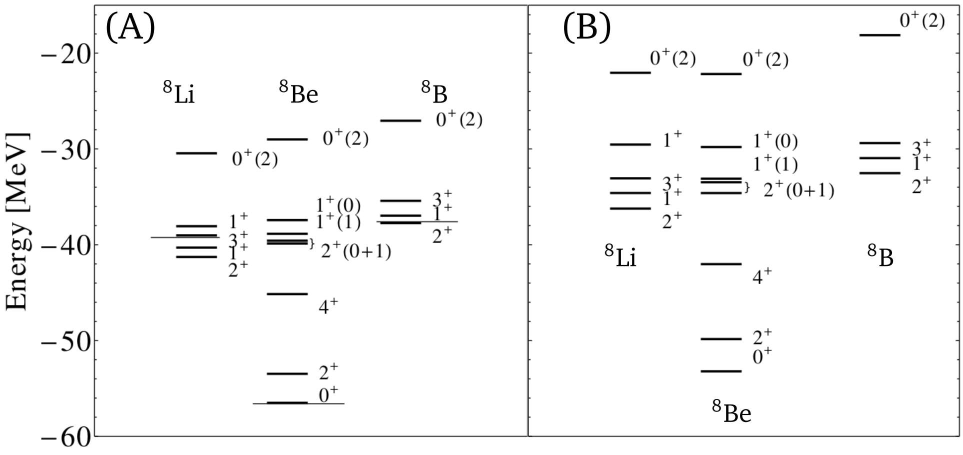

**Figure 7.2:** Experimental (A) and calculated (B) level-schemes for the $A$=8 nuclei.

A secondary goal of this thesis was to investigate the analogous energy levels of weakly-bound mirror pairs and how structure affects them.

In Fig. 7.3, the low-lying $T=1$ states in $^8$Be are compared to their analogue states in $^8$Li and $^8$B. Experimental and calculated energies are compared. Both "uniform sphere" Coulomb energy and "FMD" Coulomb energy (the Coulomb energy which we calculate using Eq.(5.34) are subtracted from the level energies. The uniform sphere and FMD Coulomb energies in question are provided in Table 7.9.

We can see clearly in this figure that the uniform sphere Coulomb energy gives too large a value for $^8$B and for $^8$Be. After subtraction of the FMD Coulomb energy from the calculated levels, they are almost degenerate. This shows that a correct treatment of the Coulomb energy is essential when performing calculations for weakly bound mirror nuclei. As the uniform sphere model also overestimates the Coulomb energy for $^8$Be, one can see that it is not only weakly-bound protons that perturb the Coulomb energy, but clustering as well.

In Table 7.8, we compare the Coulomb, kinetic and "nuclear" energies for the $2^+(1)$ and $1^+(1)$ levels whose energies are plotted in Fig. 7.3.

**Table 7.8:** Table of energies for the $T=1$ levels of $^8$Li, $^8$Be and $^8$B. Total energy , Coulomb energy and kinetic energy are all compared.

| Level | Nucleus | Total Energy [MeV] | Coulomb Energy [MeV] | Kinetic Energy [MeV] | Nucl. + Coul. [MeV] |
|---|---|---|---|---|---|
| $2^+(1)$ | $^8$Li | -36.225 | 1.825 | 118.194 | -154.420 |
| | $^8$Be | -34.609 | 3.405 | 120.058 | -154.668 |
| | $^8$B | -32.530 | 5.377 | 115.602 | -148.132 |
| $1^+(1)$ | $^8$Li | -34.603 | 1.809 | 115.006 | -149.609 |
| | $^8$Be | -33.106 | 3.398 | 117.040 | -150.145 |
| | $^8$B | -30.960 | 5.289 | 112.528 | -143.488 |

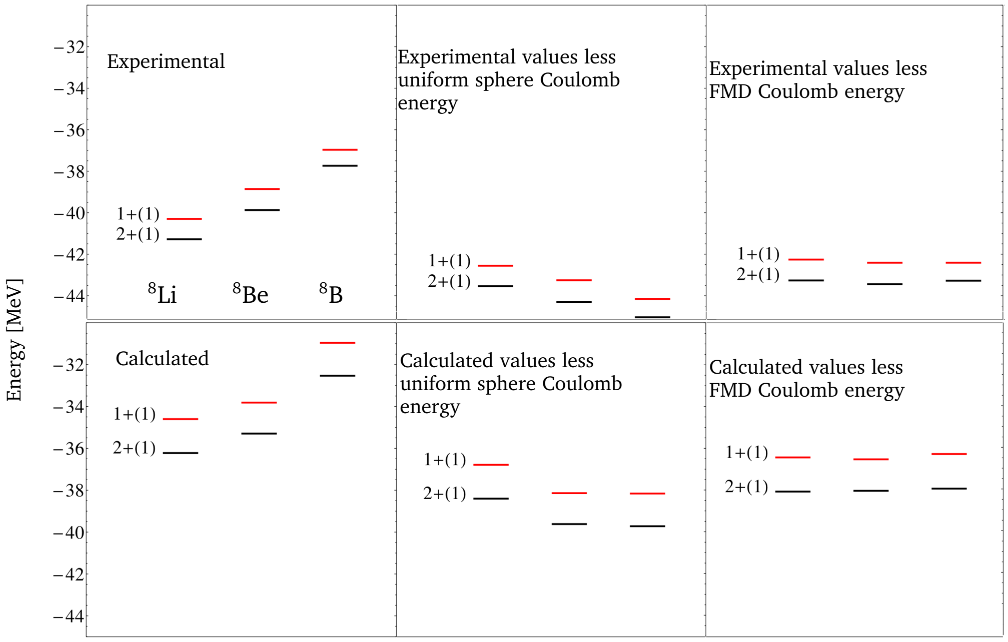

**Figure 7.3:** Experimental and calculated energies for the low-lying $T=1$ states of the $A=8$ isotriplet, plotted together. We subtract two different evaluations of the Coulomb energy: both an "FMD" Coulomb energy (calculated using Eq.(5.34)), and a "uniform sphere" Coulomb energy (calculated using Eq.(1.11)).

It should also be interesting to compare all the energy levels for the "mirror" nuclei $^8$Li and $^8$B, with and without the addition of our explicit clustering configurations to the basis. This acts as a gauge of the effect of the asymptotic region of the wave function on the analogous energy levels. Of course, this gauge is not perfect, since our VAP basis states certainly also show some clustering (Fig. 6.1-6.12). Figure 7.4 shows that low-lying levels in $^8$Li and $^8$B are almost-degenerate after subtraction of the FMD Coulomb energy both with and without the addition of cluster configurations.

Interestingly, Fig. 7.4 shows that the degeneracy of analogous levels after the subtraction of FMD Coulomb energy is actually improved by the inclusion of clustering configurations to the basis sets. The highest state (the first $0^+$ state), shows about a 1.2 MeV shift between $^8$Li and $^8$B after Coulomb energy is subtracted (Fig. 7.4(D)), but otherwise all levels in (D) are degenerate (within $\sim$ keV). One can deduce from Fig. 7.4 that a combination of accurate modelling of the asymptotic region with calculation of Coulomb energy from the eigenstates themselves allows one to reproduce the degeneracy of energy levels in the $^8$Li-$^8$B mirror nuclei.

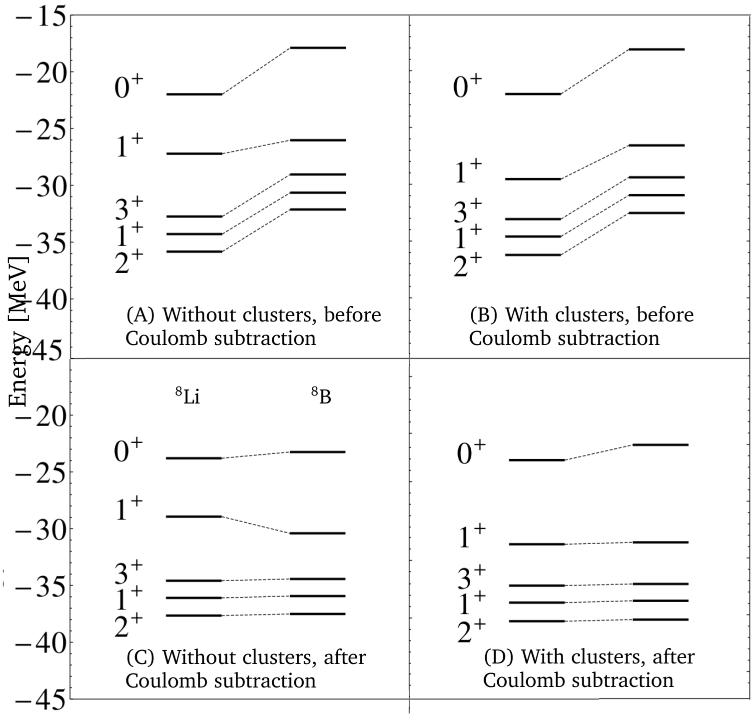

**Figure 7.4:** Energy-levels of $^8$Li and $^8$B, with and without explicit cluster configurations (referred to here as "clusters" for brevity) added to the basis sets, before and after Coulomb energy is subtracted. In all cases, the Coulomb energy was calculated in the same basis set as the energy of the states (that is, the Coulomb energy subtracted from states without cluster configurations added was itself calculated for the wave functions without the cluster configurations added). Note that subtraction of the Coulomb energy treats degeneracies of all except the highest-lying energy levels. It is interesting to note that degeneracy of analogous levels is actually improved by the inclusion of clustering configurations to the basis sets. The only level for which degeneracy is appreciably broken (by more than a few keV) is the $0^+$ level. Dotted lines guide the eye.

In Table 7.9, we compare our calculation of Coulomb energies (via Eq. 5.34) for the $T=1$ states in $^8$Li, $^8$Be and $^8$B to those calculated in the uniform sphere approximation (which gives only one Coulomb energy for all levels, since it depends only on $A$ and $Z$). The approximation and its corrections are discussed in detail in Section 1.3. What is of interest is how the $^8$B Coulomb energy is reduced for the $1^+(1)$ state, compared to that for the $2^+(1)$ state.The greater extension of the proton out of the core in the $1^+(1)$ state (calculated rms charge radii are 2.537 fm and 2.580 fm respectively for the $2^+(1)$ and $1^+(1)$ states) reduces the Coulomb energy inside the core, and this shows up as a decrease in the Coulomb energy of the $1^+(1)$ $^8$B state compared to that of the $2^+_1$ state. The effect of structure on the Coulomb energy can thus be seen to be small, but certainly present (Table 7.9).

We can conclude the section on the $A=8$ isotriplet by saying that a combination of accurate modelling of the asymptotic region and calculation of Coulomb energy from the wave functions reproduces degeneracy of energy levels in the whole isotriplet (Fig. 7.3). It was made very clear in Fig. 7.4 and Table 7.9 that comparison of energy levels in the $A=$ 8 isotriplet nuclei requires subtraction of a Coulomb energy calculated from structure. Fig. 7.3 also shows that Coulomb energy is the main breaker of degeneracy in the isotriplet, as subtracting a (structurally-dependent) Coulomb energy restores the degeneracy of the levels. The Coulomb energies listed in Table 7.9 show that the proton halo of $^8$B does reduce its Coulomb energy in the ground state and excited states.

**Table 7.9:** Comparison of Coulomb energies from FMD and from the uniform sphere approximation for the $A$=8 isotriplet nuclei.

| State | Nucleus | $E_c$ (FMD) [MeV] | $E_C$ (uniform sphere) [MeV] |
|---|---|---|---|
| $2^+(1,0)$ | $^8$Li | 1.825 | 2.151 |
| | $^8$Be | 3.398 | 4.302 |
| | $^8$B | 5.377 | 7.170 |
| $1^+(1)$ | $^8$Li | 1.809 | 2.151 |
| | $^8$Be | 3.405 | 4.302 |
| | $^8$B | 5.289 | 7.170 |

## 7.8 The A = 9 isodoublet

In Fig. 7.5, calculated level schemes for $^9$Be and $^9$B are compared to the experimental level schemes. A matter of particular interest in this isodoublet is the “missing” $1/2^+$ state in $^9$B. We place a $1/2^+$ state at 3.938 MeV above the $^9$B ground state (Figs. 6.23 and 7.5). This is about twice its expected experimental energy (1.6 MeV above ground state). This state is notoriously difficult to reproduce, as are all $^9$B states, especially when working in a bound-state approximation as we do here. This state is in all likelihood particularly broad (the width is not known, but it lies within a few tens of keV below the $^5$Li+$\alpha$ threshold [5] meaning it is probably very short-lived). Its reproduction even to this accuracy in a model-space of 53 states is thus rather impressive.

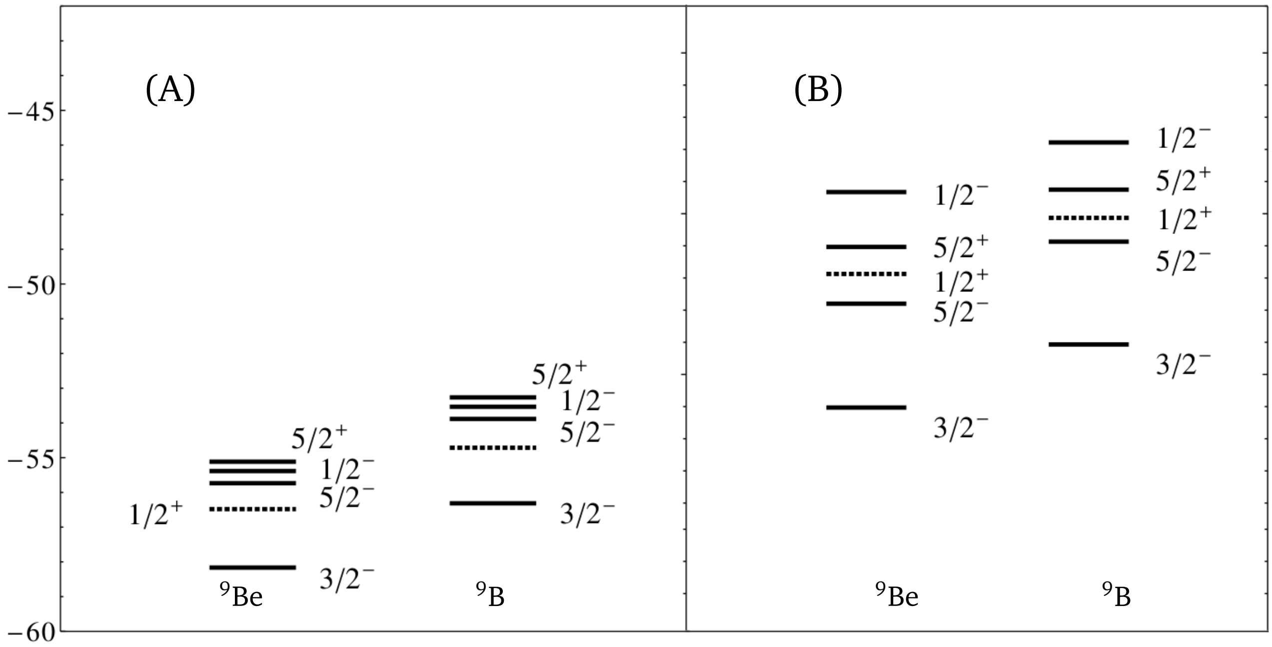

**Figure 7.5:** Experimental (A) and calculated (B) level-schemes for nuclei of the $A$=9 isodoublet.

A secondary goal of this thesis was to investigate the analogous energy levels of weakly-bound mirror pairs and how structural concerns affect them. In Fig. 7.6 the states in $^9$Be are compared to their analogue states in $^9$B. Both “uniform sphere” Coulomb energy and “FMD” Coulomb energy (the Coulomb energy which we calculate using Eq.(5.34) are subtracted from the level energies.

We can see clearly in this figure that energy levels of the mirror pair are degenerate (within a few keV) after subtraction of the “FMD Coulomb energy” (the Coulomb energy calculated from the wave function as per Eq.( 5.34)). This shows that, as long as the Coulomb energy is subtracted, and is calculated in a way that takes structure into account, the degeneracy of mirror levels is preserved.

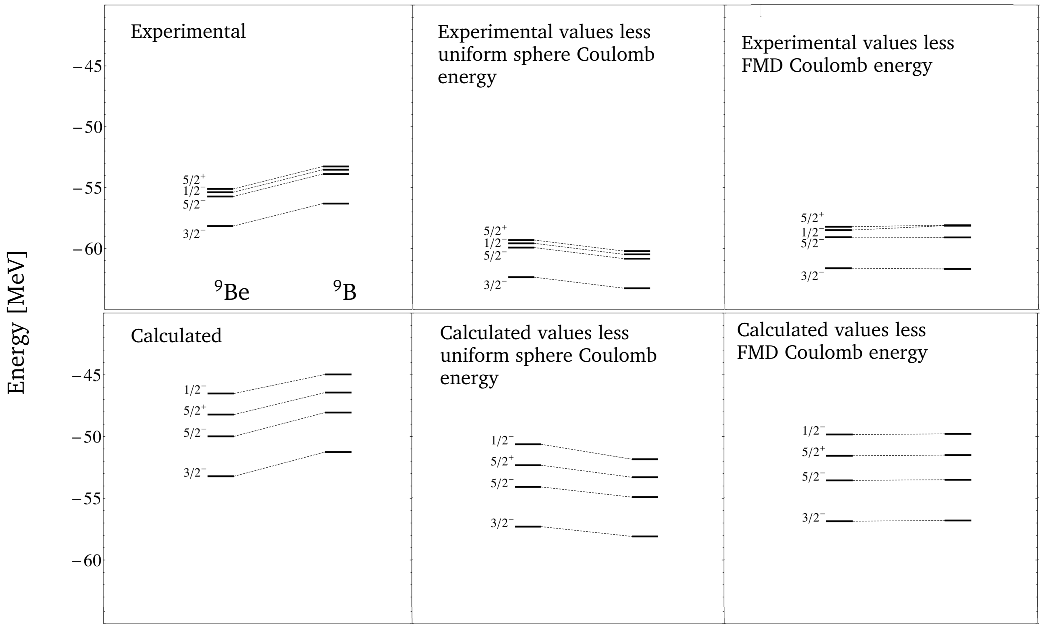

**Figure 7.6:** Calculated energies for the $A = 9$ isodoublet nuclei, plotted together. We subtract two different evaluations of the Coulomb energy: both an "FMD" Coulomb energy (calculated using Eq.(5.34)), and a "uniform sphere" Coulomb energy (calculated using Eq.(1.11)).

In Table 7.10, we compare the Coulomb, kinetic and "nuclear" energies for the levels whose energies are plotted in Fig. 7.6.

**Table 7.10:** Table of energies for the $T\!=\!1$ levels of $^{8}$Li, $^{8}$Be and $^{8}$B. Total energy , Coulomb energy and kinetic energy are all compared.

| Level | Nucleus | Total Energy [MeV] | Coulomb Energy | Kinetic Energy [MeV] | Nucl. + Coul. [MeV] |
|---|---|---|---|---|---|
| $3/2^-$ | $^{9}$Be | -53.215 | 3.446 | 139.026 | -192.240 |
| | $^{9}$B | -51.253 | 5.350 | 137.375 | -188.628 |
| $1/2^+$ | $^{9}$Be | -49.059 | 3.206 | 129.827 | -178.886 |
| | $^{9}$B | -47.315 | 4.904 | 128.516 | -175.832 |
| $5/2^-$ | $^{9}$Be | -49.984 | 3.398 | 137.658 | -187.642 |
| | $^{9}$B | -48.055 | 5.267 | 135.879 | -183.934 |
| $1/2^-$ | $^{9}$Be | -46.513 | 3.183 | 118.904 | -165.416 |
| | $^{9}$B | -44.969 | 4.683 | 117.745 | -162.714 |
| $5/2^+$ | $^{9}$Be | -48.219 | 3.184 | 130.892 | -179.111 |
| | $^{9}$B | -46.437 | 4.914 | 129.706 | -176.143 |

As for the $^{8}$Li-$^{8}$B pair, we also compare energy levels with and without the addition of our explicit clustering configurations to the basis. As before, this acts as a gauge of the effect of the asymptotic structure on the degeneracy of the energy levels of the pair. As for the $A = 8$ mirror nuclei, Figure 7.7 shows that low-lying levels in $^{9}$Be and $^{9}$B are almost-degenerate after subtraction of FMD Coulomb energy both with and without the addition of cluster configurations. Note that degeneracy of analogous levels is actually improved, as in the $A$=8 isotriplet nuclei, by the inclusion of clustering configurations to the basis sets. We thus deduce that a combination of accurate modelling of the asymptotic region, when combined with

**Table 7.11:** Comparison of Coulomb energies from FMD and from the uniform sphere approximation for the $A = 9$ isodoublet nuclei.

| State | Nucleus | $E_c$ (FMD) [MeV] | $E_C$ (uniform sphere) [MeV] |
|---|---|---|---|
| $3/2^-$ | $^9$Be | 3.446 | 4.136 |
| | $^9$B | 5.350 | 6.894 |
| $1/2^+$ | $^9$Be | 3.206 | 4.136 |
| | $^9$B | 4.904 | 6.894 |
| $5/2^-$ | $^9$Be | 3.398 | 4.136 |
| | $^9$B | 5.267 | 6.894 |
| $5/2^+$ | $^9$Be | 3.184 | 4.136 |
| | $^9$B | 4.914 | 6.894 |
| $1/2^-$ | $^9$Be | 3.183 | 4.136 |
| | $^9$B | 4.683 | 6.894 |

calculation of Coulomb energy from the wavefunctions themselves allows one to reproduce the degeneracy of energy levels in the $^9$Be-$^9$B mirror nuclei.

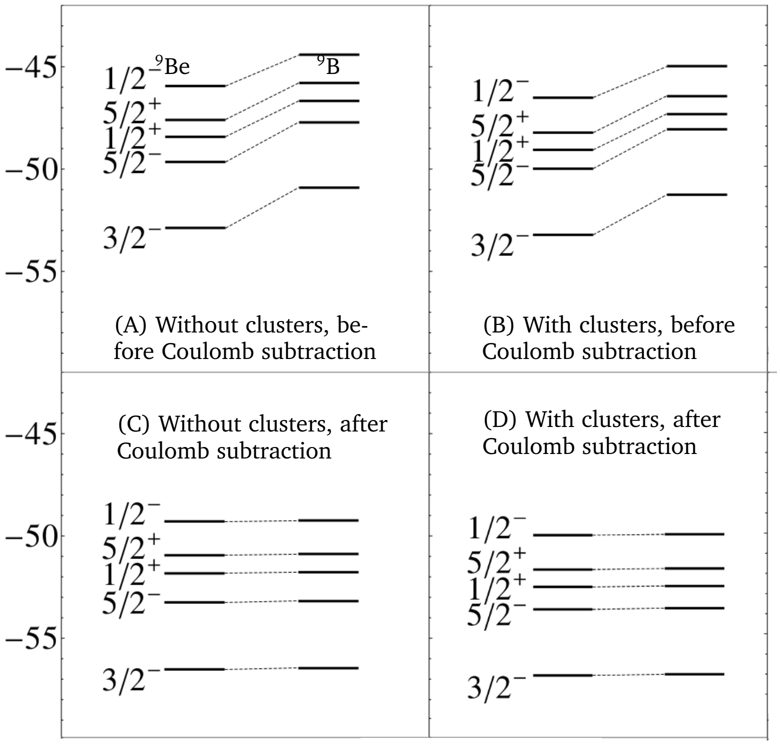

**Figure 7.7:** As in Fig. 7.4, but for $^9$Be and $^9$B.

It is of interest also for this isodoublet to compare the Coulomb energies calculated with a uniform sphere approximation to those calculated from the wave functions (as per Eq.(5.34)). These values are supplied in Table 7.11. As in the case of the $A = 8$ isotriplet nuclei, we see that the uniform sphere approximation overestimates the Coulomb energy, but to a lesser degree (about 1 MeV as opposed to 2 MeV).

We can conclude the section on the $A = 9$ isotriplet by saying that a combination of accurate modelling of the asymptotic region and calculation of Coulomb energy from the wave functions reproduces degeneracy of energy levels in the $^8$Li-$^8$B mirror pair and in the whole isotriplet (Fig. 7.6. The Coulomb energy was also seen here to be the primary lifter of the degeneracies of the isotriplet energy levels (Fig 7.6), and it was made very clear in Fig. 7.7 and Table 7.11 that comparison of energy levels requires subtraction of a Coulomb energy calculated from structure, as in these $A = 9$ nuclei, where clustering plays an important role, a uniform sphere approximation also overestimates the Coulomb energy, especially of the higher-lying levels.

## 7.9 The Boron chain

In this thesis, three nuclei of the Boron chain were modelled. Their radii and electromagnetic moments are plotted together, (Fig. 7.8-7.9) to look for trends in the isotopes with increasing neutron number.

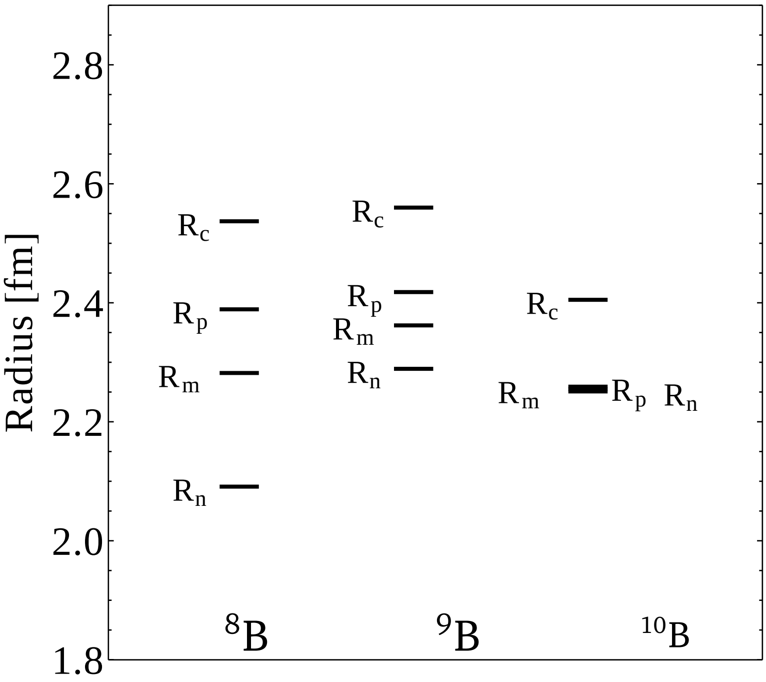

**Figure 7.8:** The radii of the Boron isotopic chain, calculated in this study.

Note in Fig. 7.8 that proton and neutron radii are not very different, and similar to the matter radius in contrast to $^{8}$B in $^{10}$B or $^{9}$B radii. This is unsurprising: Despite being quadrupole-deformed (quadrupole moment 8.427(56) $e^2$fm$^4$ [5]), $^{10}$B exhibits no clustering or weakly bound nucleons in the ground state, which could widen the discrepancy between the proton and neutron radii. The proton halo of $^{8}$B is obvious in this plot (Fig. 7.8) in the discrepancy between the its proton and neutron radius. Comparison of electromagnetic moments shows that $^{9}$B has the largest magnetic dipole moment: With the addition of an extra neutron, the dipole moment is again reduced. The $^{9}$B magnetic dipole moment probably arises from the unpaired proton (thought to pair with the neutron in $^{10}$B [104]).

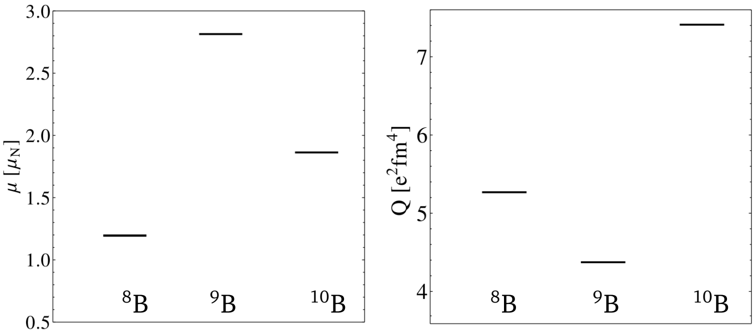

**Figure 7.9:** The magnetic dipole moments $\mu$ and electric quadrupole moments $Q$ of the Boron isotopes, calculated in this study.

# 8 Conclusion and summary

In this thesis we have modelled the nuclei $^{8}$Li, $^{8}$Be, $^{8}$B, $^{9}$Be, $^{9}$B and $^{10}$B. Our calculations reproduce the proton halo of $^{8}$B and the clustering in the ground states of the $A$=8,9 isotopes. The observable properties such as radii, quadrupole moments and transition strengths we determine for all six nuclides compare favourably with experiment and with current theory.

The question of “mirror nuclides” in the weakly-bound sector was addressed in light of the influence of thresholds and structural phenomena on Coulomb energy. It was found that the Coulomb energy is the primary lifter of the degeneracy of the energy of mirror nuclei, and that subtraction of a Coulomb energy calculated from structure can restore this degeneracy. The structural dependence of the Coulomb energy was clearly illustrated, and this serves as a caveat against oversimplification when calculating Coulomb energies of weakly bound nuclei, or when comparing weakly bound nuclei to their mirrors.

Future work would certainly include calculations of the $^{7}$Be(p,$\gamma$)$^{8}$B $S$-factor in FMD.

# 9 Appendices

## 9.1 Appendix 1: Nilsson quantum numbers

Nilsson states are the eigenstates of the single-particle anisotropic harmonic oscillator Hamiltonian $\hat{h}$ [105]:

$$\hat{h} = \frac{-\hbar}{2\mu}\nabla^2 + \frac{1}{2}\mu\left\{\omega_3^2\hat{\vec{x}}_3^2 + \omega_\perp^2\left(\hat{\vec{x}}_1^2 + \hat{\vec{x}}_2^2\right)\right\}, \tag{9.1}$$

where $\omega_3$ is the oscillator frequency along the symmetry axis, $\omega_\perp = \omega_0\left(1 + \frac{1}{3}\delta_{osc}\right)$ is the oscillator frequency along the perpendicular axis[a], and $\mu$ is the mass of the particle. The axes are defined in the body-fixed frame (*i.e.* the "perpendicular" axis is perpendicular to the symmetry axis).

The Hamiltonian of Eq.(9.1) does not commute with the angular momentum operator $\hat{J}$, since it is not symmetric under rotations. Thus the Nilsson states are not eigenstates of $\hat{J}$, and new quantum numbers are needed to characterise them.

One new quantum number is the eigenvalue of the operator $\hat{\Omega}$, which takes the projection of the single-particle angular momentum on the nuclear symmetry axis. This operator commutes with the Hamiltonian in ( 9.1) and has eigenvalue $\Omega$.

The complete list of Nilsson Model quantum numbers is then $N, n_3, \Lambda$ and $\Omega$. The $n_3$ counts the number of oscillator quanta along the symmetry-axis of the nucleus, $N$ gives the energy shell (in units of $\omega$) in which one finds the "parent orbital" (the shell-model orbital which corresponds to the Nilsson state in question); and $\Omega$; which, as stated, is the projection of the angular momentum onto the nuclear symmetry axis. The additional quantum number $\Lambda$ is related to the number of oscillator quanta along the perpendicular axis ($n_\perp$), *i.e.* [105]:

$$\Lambda = \pm n_\perp, \pm(n_\perp - 2), \pm(n_\perp - 4)\ldots \pm 1. \tag{9.2}$$

The only good quantum number of this set is $\Omega$. The others are really "labels" for a state.

## 9.2 Appendix 2: Sequential Quadratic Programming and DONLP2

This is a brief introduction to the minimisation routine DONLP2 which is used in FMD to minimise the energy of the Slater determinant with respect to the single-particle parameters. The reference [88] provides a thorough description.

The idea of any Sequential Quadratic Programming problem is that one has some twice-differentiable function $f(x)$ (hence "quadratic" programming) that one needs to minimise subject to the constraints $b(x) \geq 0$ and $c(x) = 0$. The initial step in such a problem is the method of Lagrange Multipliers: *i.e.* one has a Lagrangian $\mathfrak{L}$ which is given by [106]:

$$\mathfrak{L} = f(x) - \lambda b(x) - \sigma c(x), \tag{9.3}$$

for which $\lambda$ and $\sigma$ are Lagrange Multipliers. Instead of setting $\nabla\mathfrak{L} = 0$ and solving analytically, the SQP routines set up an algorithm in which one introduces a guess value $x^k$ that solves the Lagrange Multiplier equation, and a correction $d^k$ which is needed to make $x^k$ the solution.

---

[a] In the definition of $\omega_{perp}$, $\omega_0$ is the average frequency along all three axes and $\delta_{osc}$ is the quadrupole deformation parameter.

The Nonlinear Programming Problem routine of [88] take this general SQP problem further by allowing for more than one variable to be “active” (here “active” means it is violating the inequalities) at one time: *i.e.* it allows one to work with more than one constraint in each step [88].

## 9.3 Appendix 3: Calculating single-particle $M1$ transition strength ($B(M1)$)

$\langle {}^8B; \mathscr{J} || \hat{M}_k || {}^8B; \mathscr{J}' \rangle = \langle {}^8B; (J_7, j) \mathscr{J} || \hat{M}_k \otimes \hat{I} + \hat{I} \otimes \hat{M}_k || {}^8B; (J_7' j') \mathscr{J}' \rangle,$

where the $\mathscr{J}$'s denote total angular momentum of the nucleus ($^8$B), the $^8$B's denote the quantum numbers of $^8$B other than angular momentum; $\hat{I}$ and $\hat{M}_k$ are identity operator and electromagnetic transition operator of rank $k$ respectively, and the $J_7$ and $j$ denote the total angular momentum of the $^7$Be core and the valence nucleon.

$$\begin{aligned}
&\langle {}^8B; \mathscr{J} || \hat{M}_k || {}^8B; \mathscr{J}' \rangle = \\
&\sqrt{(2\mathscr{J}+1)(2\mathscr{J}'+1)(2k+1)} \begin{Bmatrix} J_7 & j & \mathscr{J} \\ J_7' & j' & \mathscr{J}' \\ k & 0 & k \end{Bmatrix} \times \langle {}^7Be; J_7 || \hat{M}_k || {}^7Be; J_7' \rangle \langle (p) j || \hat{I} || (p) j' \rangle + \\
&\sqrt{(2\mathscr{J}+1)(2\mathscr{J}'+1)(2k+1)} \begin{Bmatrix} J_7 & j & \mathscr{J} \\ J_7' & j' & \mathscr{J}' \\ 0 & k & k \end{Bmatrix} \times \langle (p) j || \hat{M}_k || (p) j' \rangle \langle {}^7Be; J_7 || \hat{I} || {}^7Be; J_7' \rangle
\end{aligned}$$

The first part (the term involving $\langle {}^7Be; J_7 || \hat{M}_k || {}^7Be; J_7' \rangle$) is related to the magnetic dipole moment of $^7$Be. This has an experimental value of $\underline{-1.398\ \mu_N}$ [107]. To extract the reduced matrix element from the magnetic dipole moment, one uses the relation

$$\langle JJ | \hat{M}_{10} | JJ \rangle = \sqrt{\frac{3}{4\pi}}\, \mu_{measured}. \tag{9.4}$$

Inserting into this the relation

$$\begin{pmatrix} J & 1 & J' \\ -M & q & M' \end{pmatrix} \langle J || \hat{M}_1 || J' \rangle = (-1)^{(J-M)} \langle JM | \hat{M}_{1q} | J'M' \rangle, \tag{9.5}$$

One has

$$\begin{pmatrix} J & 1 & J \\ -J & 0 & J \end{pmatrix} \langle J || \hat{M}_1 || J \rangle = \sqrt{\frac{3}{4\pi}}\, \mu_{measured}, \tag{9.6}$$

which gives a value of $\langle J_7 || \hat{M}_1 || J_7 \rangle = \underline{-1.763}\ \mu_N$ when $J_7 = 3/2$.

Now

$$\langle p; j || \hat{M}_1 || p; j' \rangle = \langle p; j || g_l \hat{\vec{l}} + g_s \hat{\vec{s}} || p; j' \rangle, \tag{9.7}$$

which means

$$\langle p(\lambda,\sigma)j||\hat{M}_1||p(\lambda'\sigma')j'\rangle = \sqrt{(2j+1)(2j'+1)(2+1)}\begin{Bmatrix} \lambda & \sigma & j \\ \lambda' & \sigma' & j' \\ 1 & 0 & 1 \end{Bmatrix} \times \langle\lambda||g_l\hat{\vec{l}}||\lambda'\rangle\langle\sigma||\hat{I}||\sigma'\rangle +$$

$$\sqrt{(2j+1)(2j'+1)(2+1)}\begin{Bmatrix} \lambda & \sigma & j \\ \lambda' & \sigma' & j' \\ 0 & 1 & 1 \end{Bmatrix} \times \langle\sigma||g_s\hat{\vec{s}}||\sigma'\rangle\langle\lambda||\hat{I}||\lambda'\rangle$$

The factors $\langle\sigma||\hat{I}||\sigma'\rangle$; $\langle\lambda||\hat{I}||\lambda'\rangle$, $\langle\lambda||\hat{\vec{l}}||\lambda'\rangle$ and $\langle\sigma||\hat{\vec{s}}||\sigma'\rangle$ evaluate according to the relation:

$$\begin{pmatrix} j & 1 & j' \\ -m & 0 & m' \end{pmatrix}\langle j||\hat{j}^{(1)}||j'\rangle = (-1)^{j-m}\langle jm|\hat{j}_0^{(1)}|j'm'\rangle = m'(-1)^{j-m}\delta_{jj'}\delta_{mm'}, \tag{9.8}$$

To reduce the 9-$J$ symbols, one can use the relation:

$$\begin{Bmatrix} J_1 & J_2 & J_3 \\ J_4 & J_5 & J_6 \\ J_7 & J_8 & J_9 \end{Bmatrix} = \begin{Bmatrix} J_1 & J_3 & J_2 \\ J_4 & J_6 & J_5 \\ J_7 & J_9 & J_8 \end{Bmatrix} \times (-1)^R, \tag{9.9}$$

where $R = \sum_i J_i$.

This gives (using the relationship below)

$$\begin{Bmatrix} J_1 & J_2 & J_3 \\ J_4 & J_5 & J_6 \\ J_7 & J_8 & 0 \end{Bmatrix} = \frac{(-1)^{J_2+J_3+J_4+J_7}\delta_{J_3J_6}\delta_{J_7J_8}}{\sqrt{(2J_3+1)(2J_7+1)}}\begin{Bmatrix} J_1 & J_2 & J_3 \\ J_5 & J_4 & J_7, \end{Bmatrix} \tag{9.10}$$

the equation:

$$\begin{aligned}
&\langle p;j(\lambda\sigma)||\hat{M}_1||p;j'(\lambda'\sigma')\rangle = \\
&\sqrt{(2j+1)(2j'+1)(2+1)} \times \{ \\
&\frac{(-1)^{2j+j'+2\sigma+\lambda+2\lambda'+\sigma'+3}}{\sqrt{(2\sigma+1)(2+1)}}\begin{Bmatrix} \lambda & j & \sigma' \\ j' & \lambda' & 1 \end{Bmatrix} \times g_l\lambda\delta_{\lambda\lambda'}\delta_{\sigma\sigma'}\sqrt{(2\sigma'+1)\lambda(\lambda+1)(2\lambda+1)} + \\
&\frac{(-1)^{2j'+2\lambda+\sigma'+2\sigma+\lambda'+j+3}}{\sqrt{(2\lambda+1)(2+1)}}\begin{Bmatrix} j & \sigma & \lambda \\ \sigma' & j' & 1 \end{Bmatrix} \times g_s\sigma\delta_{\sigma\sigma'}\delta_{\lambda\lambda'}\sqrt{(2\lambda'+1)\sigma(\sigma+1)(2\sigma+1)}\ \}
\end{aligned}$$

This is the expression one evaluates to calculate the $M1$ transition strengths with the single particle in different $l$-states.

The $B(M\lambda)$ is then [59]:

$$B(M\lambda;\mathscr{J}\to\mathscr{J}') = \frac{1}{2\mathscr{J}_i+1}|\langle{}^8B;\mathscr{J}||\hat{M}_\lambda||{}^8B;\mathscr{J}'\rangle|^2 \tag{9.11}$$

## 9.4 Appendix 4: Cluster structures

**Table 9.1:** Intrinsic proton- and neutron-density plots (cross-sections in the x-z plane) for joined Slater determinant states for $^8$B, using clusters of $^7$Be + p. Plots are arranged according to the magnitude of $r$ and the angle $\theta$ (as defined in Section 5.4). Numbers on the contour lines give nucleon density in units of nuclear saturation density (0.17 fm$^{-1}$).

| Angle [deg.] | Densities | Angle [deg.] | Densities |
|---|---|---|---|
| $r$ = 2.6 fm | | $r$ = 5.2 fm | |
| 0 | 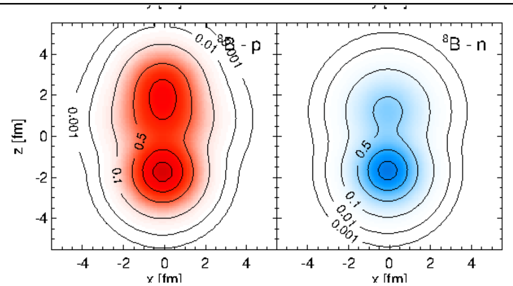 | 0 | 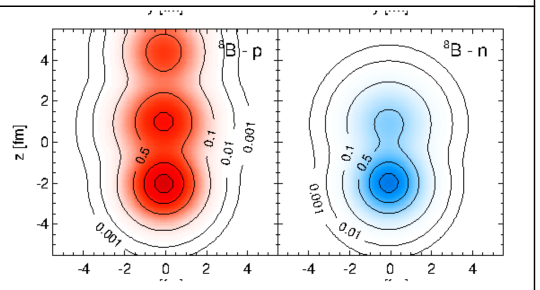 |
| 60 | 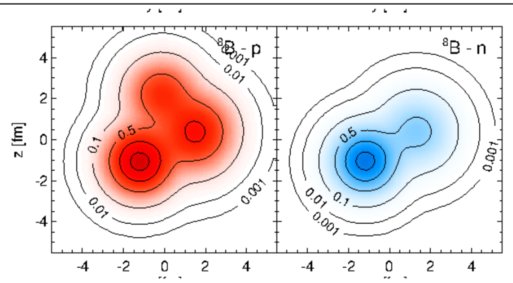 | 28 | 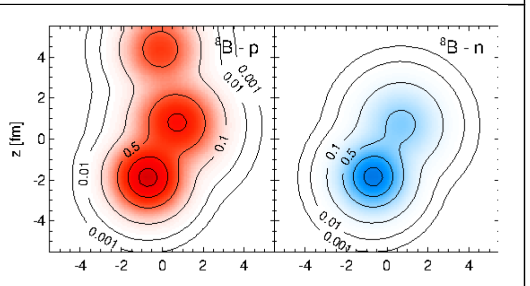 |
| 120 | 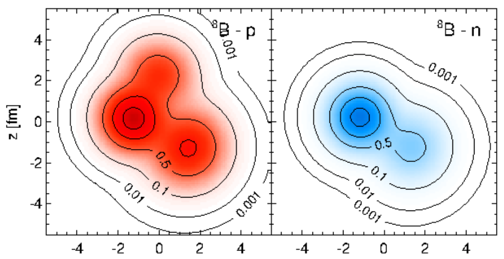 | 56 | 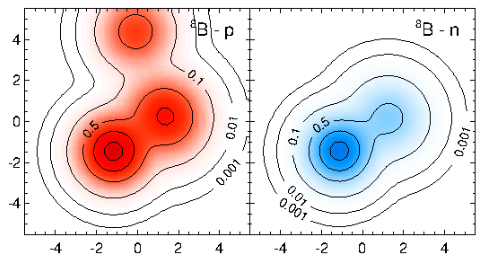 |

Continued on next page

**Table 9.1 – continued from previous page**

| Angle [deg.] | Densities | Angle [deg.] | Densities |
|---|---|---|---|
| 180 | 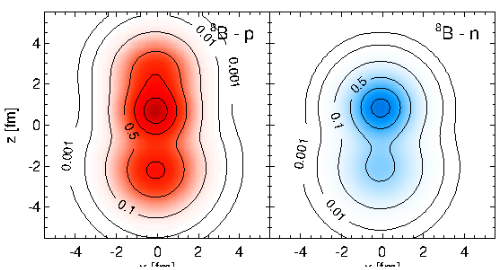 | 84 | 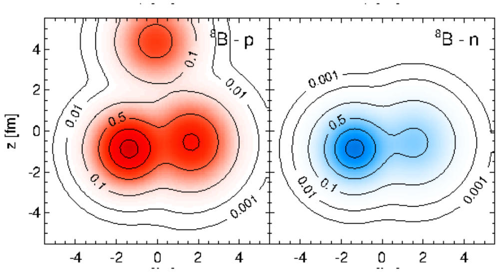 |
|  |  | 112 | 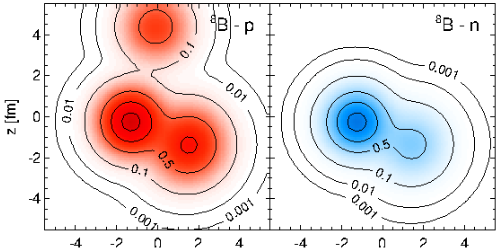 |
|  |  | 140 | 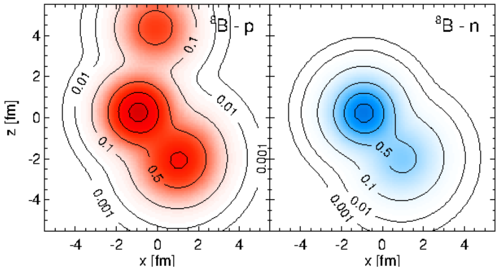 |
|  |  | 168 | 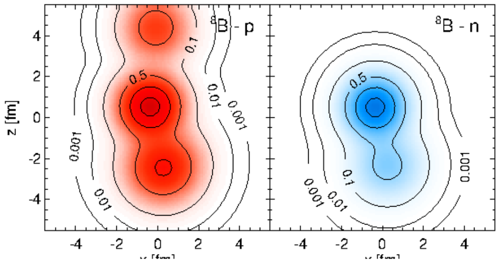 |

**Table 9.2:** Intrinsic proton- and neutron-density plots (cross-sections in the x-z plane) for joined Slater determinant states for $^8$Li, using clusters of $^7$Li + n. Plots are arranged according to the magnitude of $r$ and the angle $\theta$ (as defined in Section 5.4). Numbers on the contour lines give nucleon density in units of nuclear saturation density (0.17 fm$^{-1}$).

| Angle [deg.] | Densities | Angle [deg.] | Densities |
|---|---|---|---|
| | $r$ = 2.5 fm | | $r$ = 5 fm |
| 0 | 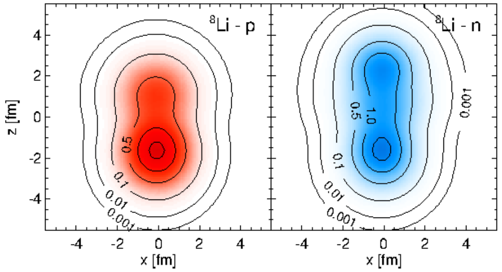 | 0 | 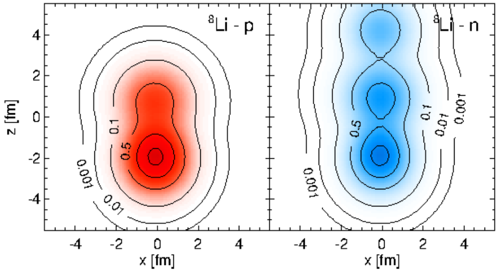 |
| 60 | 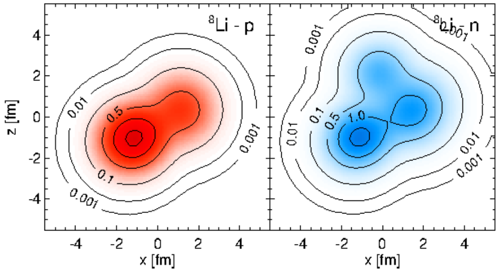 | 28 | 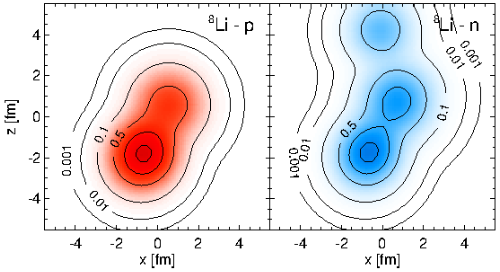 |
| 120 | 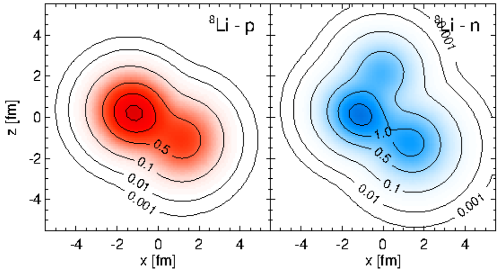 | 56 | 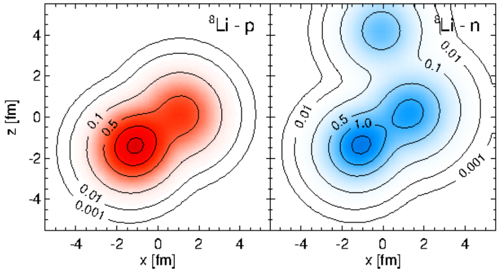 |

Continued on next page

**Table 9.2 – continued from previous page**

| Angle [deg.] | Densities | Angle [deg.] | Densities |
|---|---|---|---|
| 180 | 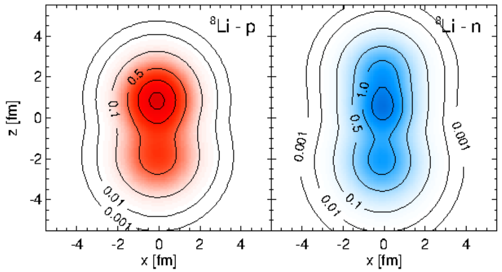 | 84 | 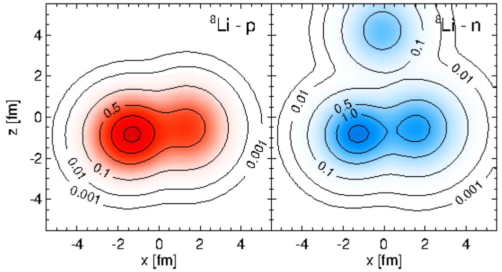 |
| | | 112 | 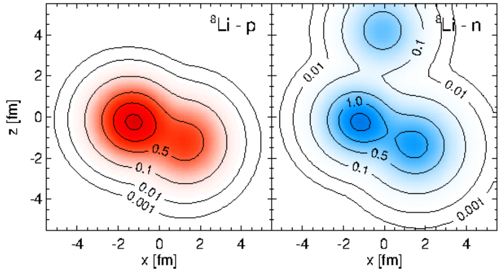 |
| | | 140 | 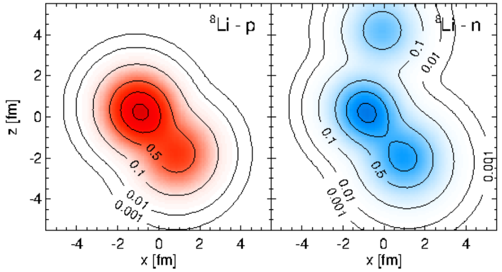 |
| | | 168 | 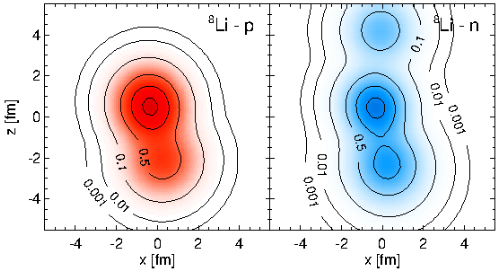 |

Continued on next page

Table 9.2 – continued from previous page

| Angle [deg.] | Densities | Angle [deg.] | Densities |
|---|---|---|---|
|  |  | 180 | 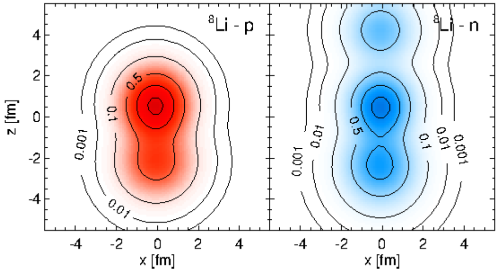 |

**Table 9.3:** Intrinsic proton- and neutron-density plots (cross-sections in the x-z plane) for joined Slater determinant states for $^8$Be, using two alpha clusters. Plots are arranged according to the magnitude of $r$ and the angle $\theta$ (as defined in Section 5.4). Numbers on the contour lines give nucleon density in units of nuclear saturation density (0.17 fm$^{-1}$).

| Angle [deg.] | Densities | Angle [deg.] | Densities |
|---|---|---|---|
| $r$ = 1.6 fm | | $r$ = 3.2 fm | |
| 0 | 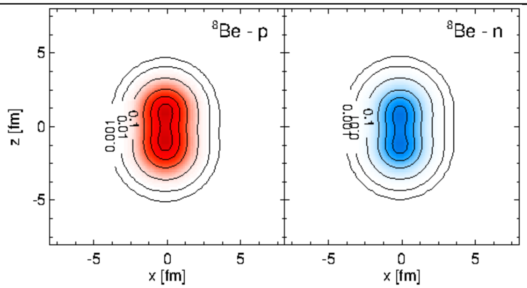 | 0 | 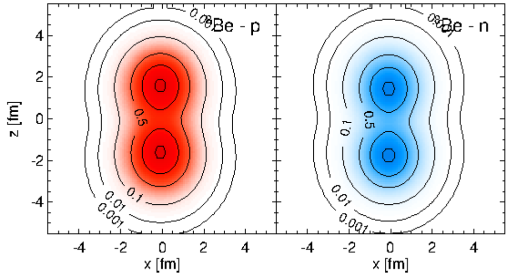 |
| 60 | 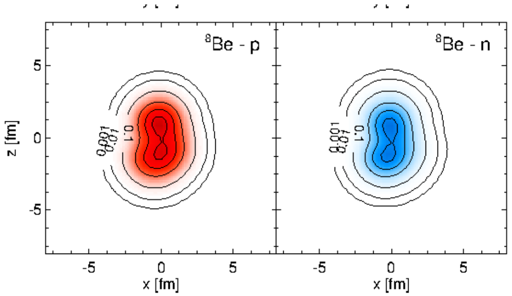 | 28 | 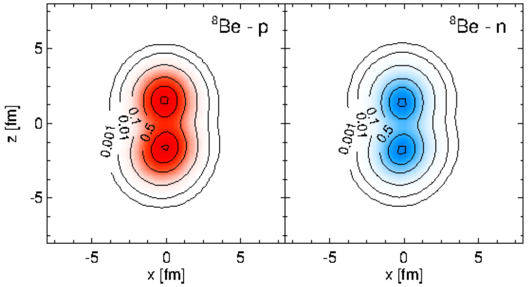 |
| 120 | 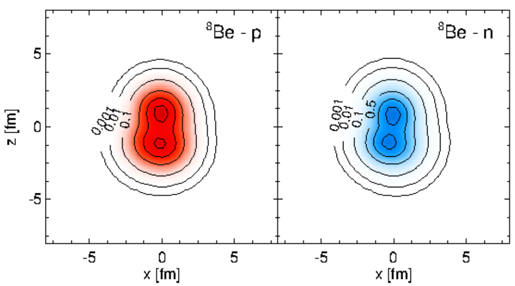 | 56 | 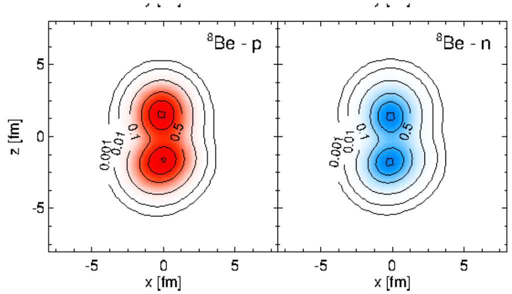 |

Continued on next page

**Table 9.3 – continued from previous page**

| Angle [deg.] | Densities | Angle [deg.] | Densities |
|---|---|---|---|
| 180 | 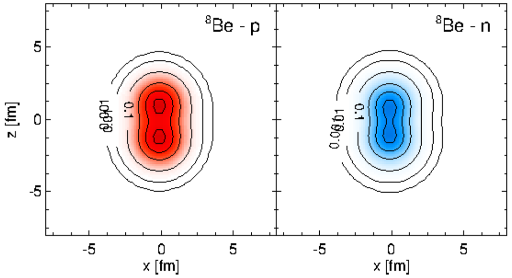 | 84 | 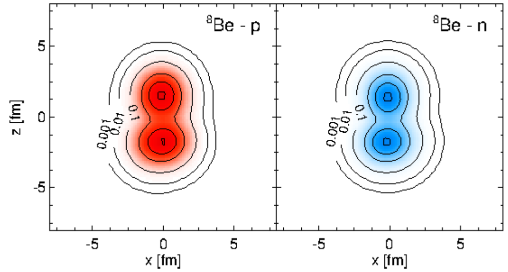 |
|  |  | 112 | 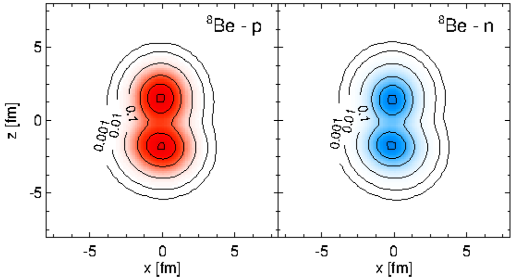 |
|  |  | 140 | 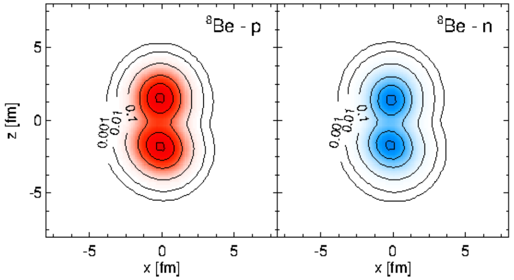 |
|  |  | 168 | 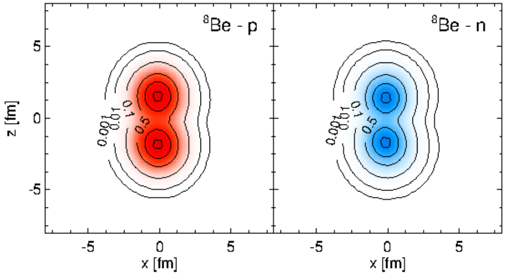 |

Continued on next page

**Table 9.3 – continued from previous page**

| Angle [deg.] | Densities | Angle [deg.] | Densities |
|---|---|---|---|
| | | 180 | 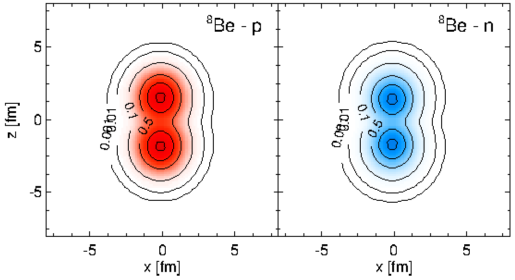 |

**Table 9.4:** Intrinsic proton- and neutron-density plots (cross-sections in the x-z plane) for joined Slater determinant states of $^{9}$Be, using clusters of $^{8}$Be + n. Plots are arranged according to the magnitude of $r$ and the angle $\theta$ (as defined in Section 5.4). Numbers on the contour lines give nucleon density in units of nuclear saturation density (0.17 fm$^{-1}$).

| Angle [deg.] | Densities | Angle [deg.] | Densities |
|---|---|---|---|
| $r$ = 2.5 fm | | $r$ = 5 fm | |
| 0 | 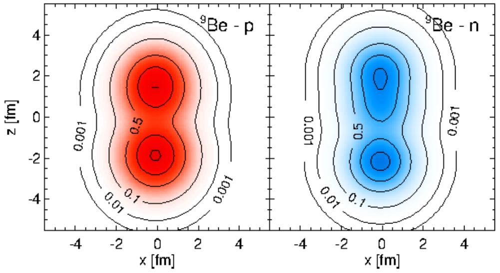 | 0 | 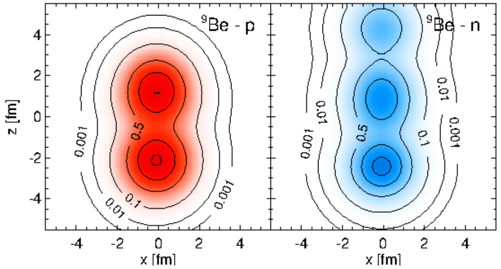 |
| 60 | 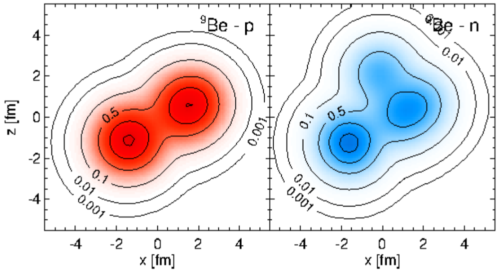 | 28 | 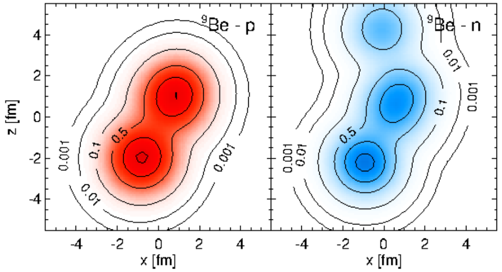 |
| 120 | 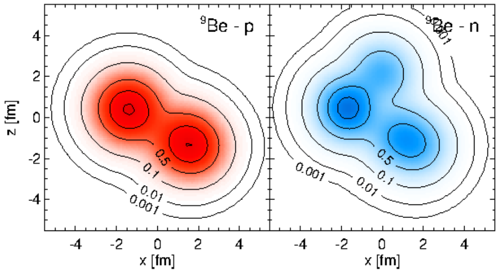 | 56 | 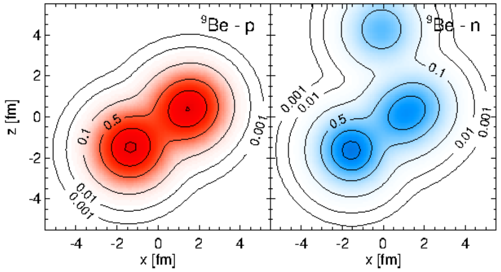 |

Continued on next page

**Table 9.4 – continued from previous page**

| Angle [deg.] | Densities | Angle [deg.] | Densities |
|---|---|---|---|
| 180 | 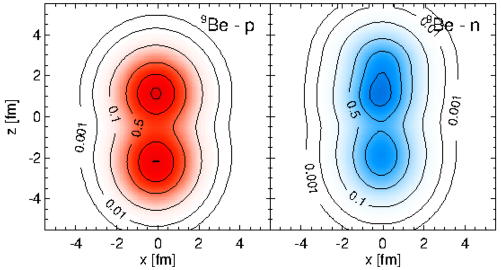 | 84 | 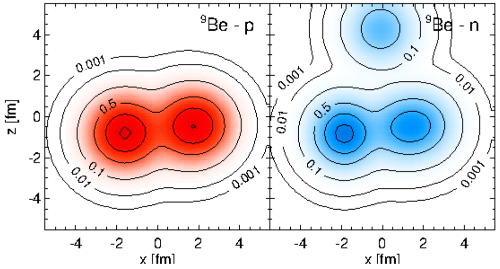 |
| | | 112 | 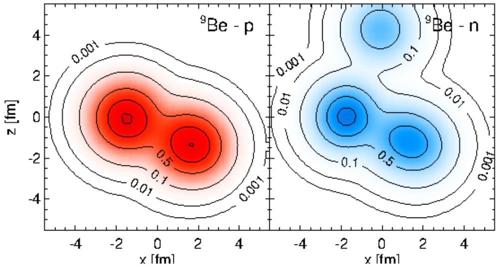 |
| | | 140 | 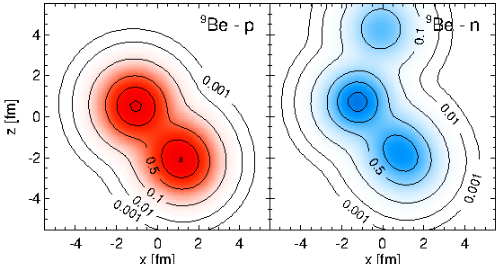 |
| | | 168 | 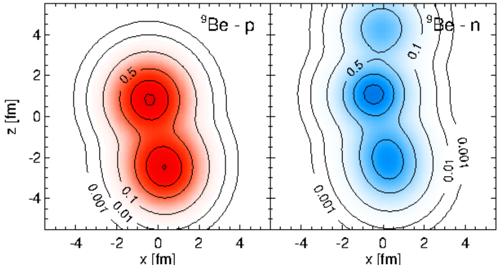 |

**Table 9.5:** Intrinsic proton- and neutron-density plots (cross-sections in the x-z plane) for joined Slater determinant states of $^{9}$B, using clusters of $^{8}$Be+H. Plots are arranged according to the magnitude of $r$ and the angle $\theta$ (as defined in Section 5.4). Numbers on the contour lines give nucleon density in units of nuclear saturation density (0.17 fm$^{-1}$).

| Angle [deg.] | Densities | Angle [deg.] | Densities |
|---|---|---|---|
| | $r$ = 2.5 fm | | $r$ = 5.0 fm |
| 0 | 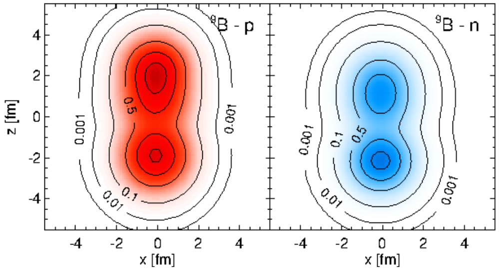 | 0 | 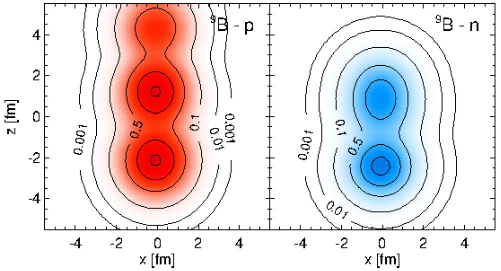 |
| 60 | 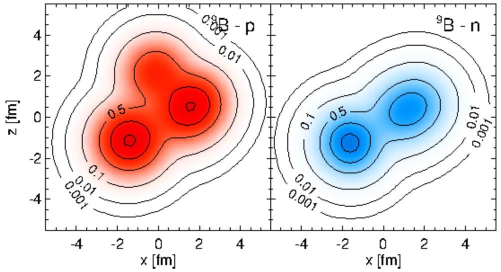 | 28 | 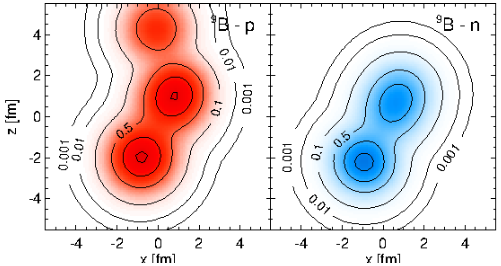 |
| 120 | 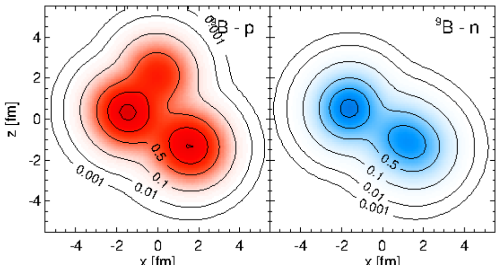 | 56 | 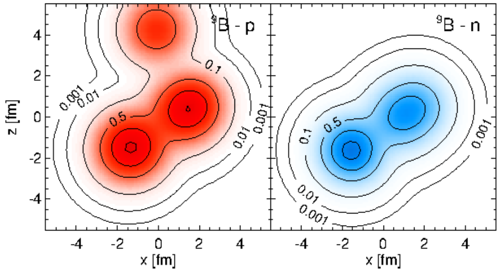 |

Continued on next page

**Table 9.5 – continued from previous page**

| Angle [deg.] | Densities | Angle [deg.] | Densities |
|---|---|---|---|
| 180 | 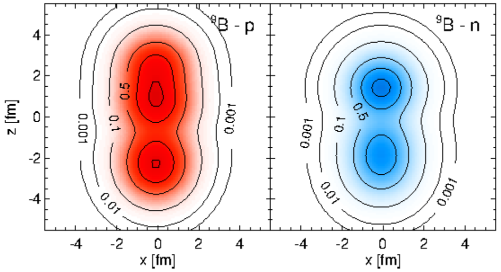 | 84 | 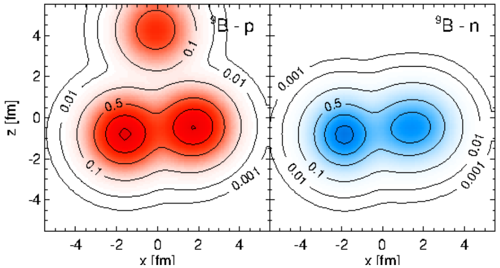 |
|  |  | 112 | 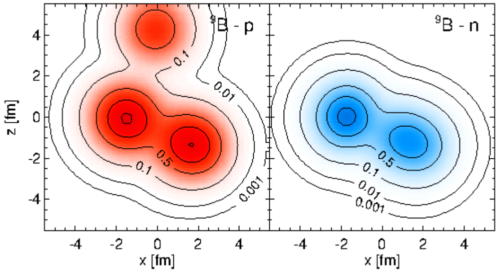 |
|  |  | 140 | 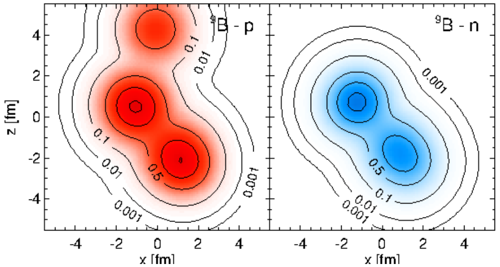 |
|  |  | 168 | 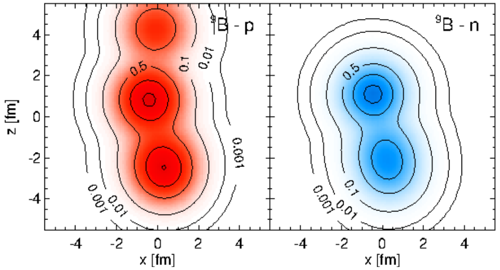 |

**Table 9.6:** Intrinsic proton- and neutron-density plots (cross-sections in the x-z plane) for joined Slater determinant states of $^{10}$B, using clusters of $^{6}$Li+$^{4}$He. Plots are arranged according to the magnitude of $r$ and the angle $\theta$ (as defined in Section 5.4). Numbers on the contour lines give nucleon density in units of nuclear saturation density (0.17 fm$^{-1}$).

| Angle [deg.] | Densities | Angle [deg.] | Densities |
|---|---|---|---|
| $r$ = 0.77 fm | | $r$ = 1.54 fm | |
| 0 | 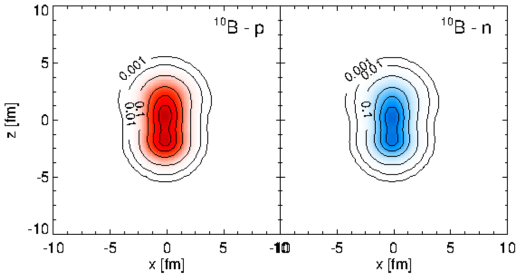 | 0 | 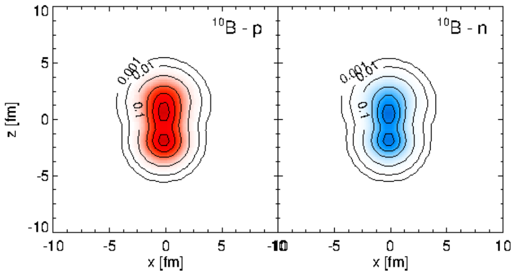 |
| 60 | 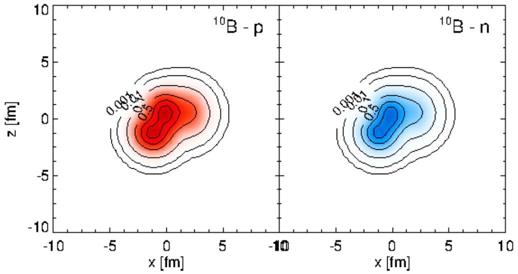 | 28 | 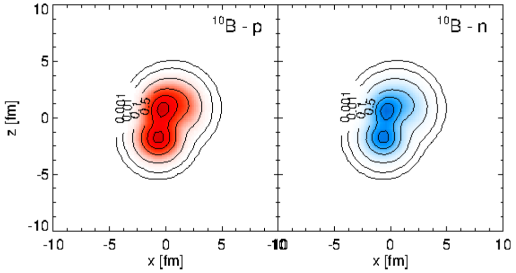 |
| 120 | 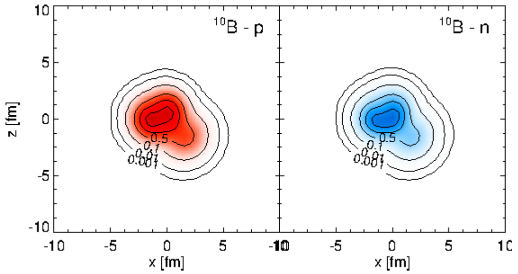 | 56 | 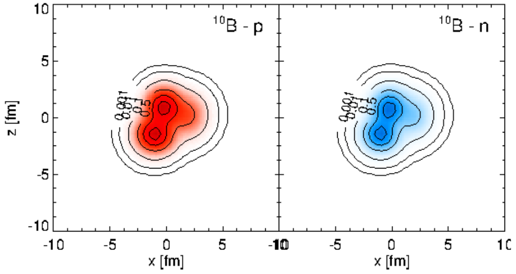 |

Continued on next page

**Table 9.6 – continued from previous page**

| Angle [deg.] | Densities | Angle [deg.] | Densities |
|---|---|---|---|
| 180 | 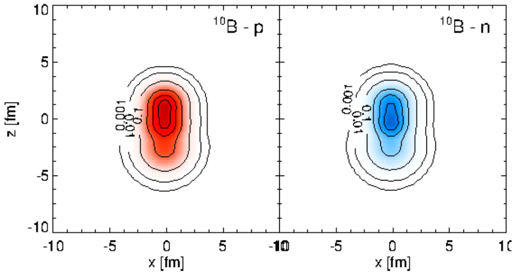 | 84 | 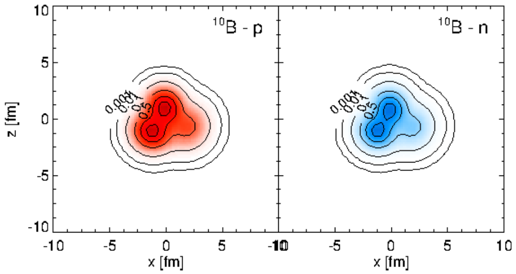 |
| | | 112 | 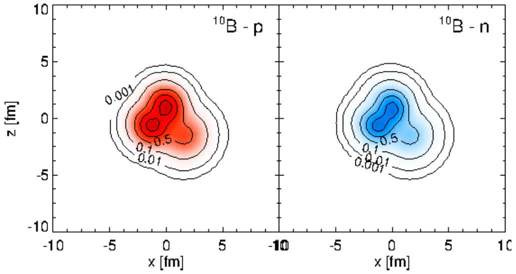 |
| | | 140 | 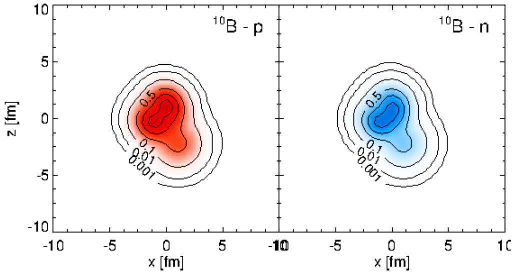 |
| | | 168 | 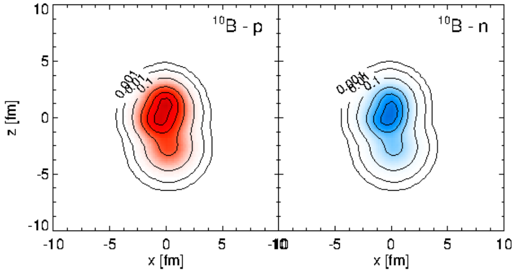 |

## Bibliography

[1] C. E. Rolfs and W. S. Rodney. Cauldrons in the Cosmos: Nuclear Astrophysics. The University of Chicago Press, Chicago, 1988. Pp 150, 156, 493.

[2] I. Bergström. *Introduction to the Lysekil Symposium 1966*. In C.J. Herrlander W. Forsling and H. Ryde, editors, *Nuclides Far off the Stability Line*, page Pg. 5. Alqvist and Wiskell publishing, 1966.

[3] K. Ikeda, N. Takigawa, and H. Horuichi. *The Systematic Structure Change into the Molecule-Like Structures in the Self-Conjugate 4*n *Nuclei.* Prog. Theor. Phys. *(Japan)*, Supplement:464, 1968.

[4] M. H. Smedberg, T. Baumann, T. Aumann, L. Axelsson, U. Bergmann, M. J. G. Borge, D. Cortina-Gil, L. M. Fraile, H. Geissel, L. Grigorenko, M. Hellstrom, M. Ivanov, N. Iwasa, R. Janik, B. Jonson, H. Lenske, K. Markenroth, G. Munzenberg, T. Nilsson, A. Richter, K. Riisager, C. Scheidenberger, Schrieder, W. Schwab, H. Simon, B. Sitar, P. Strmen, K. Summerer, M. Winkler, and M. . Zhukov. *New Results on the Halo Structure of* $^{8}$B. Phys. Lett., **452B**:1, 1999.

[5] D. R. Tilley, H.Kelley, J. L.Godwin, D. J. Millener, J. E. Purcell, C. G.Sheu, and H. R. Weller. *Energy Levels of Light Nuclei* $A = 8, 9, 10$. Nucl. Phys., **A745**:155, 2004 (revised 2014).

[6] X. Zhang, K. M. Nollet, and D. R. Phillips. *Marrying* ab initio *Calculations and Halo EFT: The case of* $^{7}\mathrm{Li} + \mathrm{n} \rightarrow ^{8}\mathrm{Li} + \gamma$. Phys. Rev C, **89**:024613, 2014.

[7] R. G. Thomas. *An Analysis of the Energy Levels of the Mirror Nuclei,* $^{13}$C *and* $^{13}$N. Phys. Rev., **88**:1109, 1952.

[8] J. B. Ehrman. *On The Displacement of Corresponding Energy Levels of* $^{13}$C *and* $^{13}$N. Phys. Rev., **81**:412, 1951.

[9] N. Michel, W. Nazarewicz, and M. Ploszajczak. *Isospin Mixing and Coupling to the Continuum in Weakly Bound Nuclei.* Phys. Rev. C, **82**:044315, 2010.

[10] H. T. Fortune and R. Sherr. *Constraints on Energy of* $^{9}\mathrm{B}(1/2^{+}_{1})$ *and* $^{10}\mathrm{C}(0^{+}_{2})$. Phys. Rev. C, **73**:064302, 2006.

[11] J.-P. Mitchell, G. V. Rogachev, E. D. Johnson, L. T. Baby, K. W. Kemper, A. M. Moro, P. Peplowski, A. Volya, and I. Wiedenhöver. *Structure of* $^{8}$B *from Elastic and Inelastic* $^{7}\mathrm{Be} + \mathrm{p}$ *Scattering.* arXiv:1303.0331v1 [nucl-ex], 2013.

[12] H. Feldmeier. *Fermionic Molecular Dynamics*. Nucl. Phys., **A515**:147, 1990.

[13] T. Neff and H. Feldmeier. *Cluster Structure in the Fermionic Molecular Dynamics Approach*. In M. Brenner, editor, *Cluster Structure of Atomic Nuclei*, pages 67–94. Research Signpost publishing, 2010.

[14] M. Chernykh, H. Feldmeier, T. Neff, P. von Neumann-Cosel, and A. Richter. *Structure of the Hoyle State in* $^{12}$C. Phys. Rev. Lett., **98**:032501, 2007.

[15] A. Zakova, Z. Andjelkovic, M. L. Bissell, K. Blaum, G. W. F. Drake, C. Geppert, M. Kowalska, J. Krämer, A. Krieger, M. Lochmann, T. Neff, R. Neugart, W. Nörtershäuser, R. Sanchez, F. Schmidt-Kaler, D. Tiedemann, Z.-C. Yan, and D. T. Yordanov C. Zimmermann. *Isotope Shift Measurements in the* $2\mathrm{s}1/2 \rightarrow 2\mathrm{p}3/2$ *Transition of* $\mathrm{Be}^{+}$ *and Extraction of the Nuclear Charge Radii of* $^{7,10,11}$Be. J. Phys. G.: Part. Nucl. Phys., **37**:055107, 2010.

[16] N. Auerbach. *Coulomb effects in Nuclear Structure*. Phys. Rep., **98**:273, 1983.

[17] J. A. Nolen and J. P. Schiffer. *Coulomb Energies*. Ann. Rev. Nucl. Sci., **19**:472, 1969.

[18] I. Kelson E. Comay and A. Zidon. *The Thomas-Ehrman Shift across the Proton Dripline*. Phys. Lett., **210B**:31, 1998.

[19] Y. Akaishi, S.A. Chin, H. Horiuchi, and K. Ikeda. Cluster Models and Other Topics . World Scientific Pubishing, Singapore, 1986. Pp 1-4, 15-17, 43-50.

[20] B. Ramin-Torabi. *Structure of Beryllium Isotopes in Fermionic Molecular Dynamics*. PhD Thesis. TU Darmstadt., 2010.

[21] L.R. Hafstad and E. Teller. *The Alpha Particle Model of the Nucleus.* Phys. Rev, **54**:681, 1938.

[22] W. Greiner, J. Y. Park, and W. Scheid. *Nuclear Molecules*. World Scientific Publishing, Singapore, 1995. Pp 118-122.

[23] S. Quaglioni and P. Navrátil. *Ab Initio Many-Body Calculations of n-*$^3$H*, n-*$^4$He*, p-*$^{3,4}$He*, and n-*$^{10}$Be *Scattering*. *Phys. Rev. Lett.*, 101:092501, 2008.

[24] D. Cortina-Gil *et al. New Proof of the* $^8$B *Ground State Configuration.* Phys. Lett ***B***, **529**:36, 2002.

[25] J. al Khalili. *An Introduction to Halo Nuclei*. *Lect. Notes Phys.*, **651**, Springer-Verlag Publishing, Berlin 2004. Pp 1-4.

[26] P. G. Hansen and B. Jonson. *The Neutron Halo of Extremely Neutron-Rich Nuclei*. Europhys. Lett., **4**:409, 1987.

[27] B. Jonson. *Halo Nuclei*. Nucl. Phys., **A574**:151–c, 1994.

[28] D. L. Canham and H-W. Hammer. *Universal Properties and Structure of Halo Nuclei*. Eur. Phys. J. A, **37**:367, 2008.

[29] K. Hagino, I. Tanihata, and H. Sagawa. *Exotic Nuclei far from the Stability Line.* arXiv:1208.1583 [nucl-th].

[30] J.-M. Richard, Q. Wang, and Q. Zhao. *Possibility of a New Neutral Hypernucleus* $^{4}_{\Lambda,\Lambda}\mathrm{n} = (n, n, \Lambda, \Lambda)$. I.O.P. (Conf. Ser.), **569**:012079, 2014.

[31] L. H. Thomas. *The Interaction Between a Neutron and a Proton and the Structure of* $^3$H. Phys.Rev., **47**:903, 1935.

[32] K. Riisager, A. S. Jensen, and P. Möller. *Two Body Haloes.* Nucl. Phys., **A548**:393, 1992.

[33] H. Feldmeier. *Clusters, Haloes and S Factors in Fermionic Molecular Dynamics*. arXiv:1307.6449 [nucl-th], 2014.

[34] H. M. Xu, C. A. Gagliardi, R. E. Tribble, A. M. Mukhamedzhanov, and N. K. Timofeyuk. *Overall Normalization of the Astrophysical S Factor and the Nuclear Vertex Constant for* $^7\mathrm{Be}(\mathrm{p},\gamma)^8\mathrm{B}$ *Reactions.* Phys. Rev. Lett, 73:2027, 1994.

[35] P. Descouvemont and D. Baye. *Microscopic Study of the* $^7\mathrm{Li}(n,\gamma)^8\mathrm{Li}$ *and* $^7\mathrm{Be}(p,\gamma)^8\mathrm{B}$ *Reactions in a Multiconfiguration 3-Cluster Model.* Nucl. Phys., **A567**:341, 1994.

[36] P. Navrátil, R. Roth, and S. Quaglioni. *Ab initio Many Body Calculations of the* $^7\mathrm{Be}(\mathrm{p},\gamma)^8\mathrm{B}$ *Radiative Capture.* Phys. Lett., **704B**:379, 2011.

[37] T. Myo, A. Umeya, K. Horii, H. Toki, and K. Ikeda. *Shell and alpha cluster structures in* $^8$Be *with Tensor-Optimised Shell Model.* Prog. Theor. Exp. Phys., 033D01, 2014.

[38] T. Minamisono, T. Ohtsubo, I. Minami, S. Fukuda, A. Kitagawa, M. Fukuda, K. Matsuta, Y. Nojiri, S. Takeda, H. Sagawa, and H. Kitagawa. *Proton Halo of* $^{8}$B *disclosed by its Giant Quadrupole Moment.* Phys. Rev. Lett., **69**:2058, 1992.

[39] E. Liatard *et al. Matter Distributions in Neutron-Rich Light Nuclei and Total Reaction Cross Sections.* Europhys. Lett., **13**:401, 1990.

[40] A. Ozawa, T. Suzuki, and I. Tanihata. *Nuclear Size and Related Topics* . Nucl. Phys A, **693**:32, 2001.

[41] J. S. Al Khalili, J.A. Tostevin, and I.J. Thompson. *Radii of Halo Nuclei from Cross Section Measurements*. Phys. Rev.*C*, **54**:1843, 1996.

[42] R. B. Firestone, V. S. Shirley, C. M. Baglin, S. Y. F. Chu, and J. Zipkin (Eds.). Table of Isotopes (Vol. 1). John Wiley and sons publishing, New York, 1996.

[43] A. Csótó. *Proton Skin of* $^{8}$B *in a Microscopic Model.* Phys. Lett., **315B**:24, 1993.

[44] K. Riisager and A.S. Jensen. *The Radius of* $^{8}$B *and Solar Neutrinos.* Phys. Lett., **301B**:6, 1993.

[45] H. Nakada and T. Otsuka. *E2 Properties of Nuclei Far from Stability and the Proton-Halo Problem of* $^{8}$B. Phys. Rev. ***C***, **49**:886, 1994.

[46] W. Schwab, H. Geissel, H. Lenske, K.-H. Behr, A. Brünle, K. Burkard, H. Irnich, T. Kobayashi, G. Kraus, A. Mage, G. Minzenberg, F. Nickel, K. Riisager, C. Scheidenberger, B.M. Sherrill, T. Suzuki, and B. Voss. *Observation of a Proton Halo in* $^{8}$B. Z. Phys. A, **350**:283, 1995.

[47] R. E. Warner, J. H. Kelley, P. Zecher, F. D. Becchetti, J. A. Brown, C. L. Carpenter, A. Galonsky, J. Kruse, A. Muthukrishnan, A. Nadasen, R. M. Ronningen, P. Schwandt, B. M. Sherrill, J. Wang, and J. S. Winfield. *Evidence for a Proton Halo in* $^{8}$B*: Enhanced Total Reaction Cross Sections at 20-60 MeV per Nucleon. Phy. Rev.* ***C***, **52**:R1106(R), 1995.

[48] M. M. Obuti, T. Kobayashi, D. Hirata, Y. Ogawa, A. Ozawa, K. Sugimoto, I. Tanihata, D. Olson, W. Christie, and H. Wieman. *Interaction Cross Section and the Interaction Radius of* $^{8}$B. Nucl. Phys., **A609**:74, 1996.

[49] A. Csótó. *Off-Shell Effects in the Energy Dependence of the* $^{7}$Be$(p,\gamma)^{8}$B *Astrophysical S Factor.* Phys. Lett., **394B**:247, 1997.

[50] W. C. Haxton, P. D. Parker, and C. E. Rolfs. *Solar Hydrogen Burning and Neutrinos*. Nucl. Phys., **A777**:226, 2006.

[51] E. G. Adelberger *et al. Solar Fusion Cross Sections II: The* pp *chain and* CNO *cycle.* Rev. Mod. Phys., **83**:195, 2011.

[52] R. Bass. *Nucler Reactions with Heavy Ions*. Springer-Verlag publishing, Berlin, 1980. Pp 285-290.

[53] P. D. Parker. $^{7}$Be(p,$\gamma$)$^{8}$B *Reaction.* Phys. Rev., **150**:851, 1966.

[54] R. W. Kavanagh *et al.* $^{7}$Be$(p,\gamma)^{8}$B *and* $^{7}$Be$(d,\gamma)^{8}$Be *Cross Section Measurements.* Bull. Am. Phys. Soc., **4**:444, 1958.

[55] F. J. Vaughn, R. A. Chalmers, D. Kohler, and L. F. Chase Jr. *Cross Section for the* $^{7}$Be(p,$\gamma$)$^{8}$B *Reaction.* Phys. Rev. ***C***, **2**:1657, 1970.

[56] B. W. Fillipone, A. J. Elwyn, C. N. Davids, and D. D. Koetke. *Proton Capture Cross Section of* $^{7}$Be *and the Flux of High Energy Solar Neutrinos.* Phys. Rev. C, **28**:2222, 1983.

[57] T. Motobayashi, N. Iwasa, Y. Ando, M. Kurokawa, H. Murakami, J. Ruan, S. Shimoura, S. Shirato, N. Inabe, M. Ishihara, T. Kubo, Y. Watanabe, M. Gai, R. H. France III, K. I. Hahn, Z. Zhao, T. Nakamura, T. Teranishi, Y. Futami, K. Furutaka, and Th. Delbar. *Coulomb Dissociation of* $^8$B *and the* $^7$Be(p, $\gamma$)$^8$B *Reaction at Low Energies.* Phys. Rev. Lett., **73**:2680, 1994.

[58] F. Strieder *et al. Observation of a Proton Halo in* $^8$B. Nucl. Phys., **A696**:219, 2001.

[59] F. Schümann *et al. Absolute Cross Section of* $^7$Be(p, $\gamma$)$^8$B. Phys. Rev. ***C***, **73**:015806, 2006.

[60] R. J. Furnstahl and K. Hebeler. *New Applications of Renormalisation Group Methods in Nuclear Physics.* Rep. Prog. Phys., **76**:126301, 2013.

[61] A. Csótó and K. Langanke. *Effects of* $^8$B *size on the Low Energy* $^7$Be*(p*$\gamma$*)*$^8$B *Cross Section.* Nucl. Phys., **A636**:240, 1998.

[62] D. W. Bardayan *et al. Direct Measurements of* (p, $\gamma$) *Cross Sections at Astrophysical Energies using Radioactive Beams and the Daresbury Recoil Separator*. Eur. Phys. J. A, **42**:457, 2009.

[63] P. Descouvemont. *Reanalysis of the* $^7$Be*(p,*$\gamma$*)*$^8$B *S Factor in a Microscopic Model.* Phys. Rev. C, **70**:065802, 2004.

[64] R. Davis, D. S. Harmer, and K. C. Hoffman. *Search for Neutrinos from the Sun.* Phys. Rev. Lett., **20**:1205, 1968.

[65] Q. R. Ahmad *et al. Measurement of the Rate of* $\nu_e + \mathrm{d} \rightarrow \mathrm{p} + \mathrm{p} + e^-$ *Interactions Produced by* $^8$B *Solar neutrinos at the Sudbury Neutrino Observatory.* Phys. Rev. Lett., **87**:071301–1, 2001.

[66] Borexino Collaboration. *Neutrinos from the primary proton - proton fusion process in the Sun*. Nature, **512**:383, 2014.

[67] P. Navrátil, C. A. Bertulani, and E. Caurier. $^7$Be(p, $\gamma$)$^8$B *S Factor from* ab initio *No-Core Shell Model Wave Functions.* Phys Rev. ***C***, **73**:065801, 2006.

[68] H. Geissel. *Physics with Exotic Nuclei and Exotic Atoms at Relativistic Energies.* Lecture at the Euroschool Valencia, September 2003.

[69] J. Livesay. *Structure of* $^8$B *through* $^7$Be + p *Scattering.* Talk at the ORNL workshop, December 2012.

[70] C. J. Gallagher and S. A. Moszkowski. *Coupling of Angular Momenta in Odd-Odd Nuclei.* Phys. Rev., **111**:1282, 1958.

[71] A. Csótó, R. Roth, H. Hergert, P. Papakonstantinou, T. Neff, and H. Feldmeier. *The* $^7$Be($p, \gamma$)$^8$B *Reaction and the Properties of* $^7$Be. Phys. Rev. C, **52**:1130, 1995.

[72] F. M. Nunes, R. Crespo, and I. J. Thompson. *Uncertainties in the Ground State Structure of* $^8$B *and Implications for the* $S_{17}$ *Astrophysical S Factor.* Nucl. Phys., **A634**:527, 1996.

[73] B. V. Pritychenko. *Intermediate-Energy Culomb Excitation of the Neutron-Rich Radioactive Isotopes* $^{26-28}$Ne*,* $^{28-31}$Na*,* $^{30-34}$Na*,* $^{36-38}$Al*,* $^{33}$Si *and* $^{34}$P. PhD Thesis, Michigan State University, 2000.

[74] B. V. Danilin V. D. Efros J. M. Bang J. S. Vaagen Russian-Nordic-British Theory (RNBT) collaboration, N. B. Shul'gina and M. V. Zhukov. *Three-body Structure of* $^8$Li *and the* $^7$Li(n, $\gamma$)$^8$Li *Reaction*. Nucl. Phys., **A597**:197, 1996.

[75] G. Ewald, W. Nörtershäuser, A. Dax, S. Götte, R. Kirchner, H.-J. Kluge, Th. Kühl, R. Sanchez, A. Wojtaszek, B. A. Bushaw, G. W. F. Drake, Z.-C. Yan, and C. Zimmermann. *Nuclear Charge Radii of* $^{8,9}$Li *determined by Laser Spectroscopy*. Phys. Rev. Lett., **93**:113002, 2004.

[76] T. Kajino. *Cosmological Nucleosynthesis in the Big Bang and Supernovae*. *Journal of Nuclear Science and Technology*, **39**:530, 2002.

[77] R. Sherr and G. Bertsch. *Coulomb Energy Systematics and the Missing State in* $^{9}$B. Phys. Rev. C, **32**:1809, 1985.

[78] H. Reeves and J.-P. Meyer. *Cosmic Ray Nucleosynthesis and the Infall Rate of Extragalactic Matter in the Solar Neighborhood*. Astrophys. J, **226**:613, 1978.

[79] O. Burda, P. von Neumann-Cosel, A. Richter, C. Forssen, and B. A. Brown. *Resonance Parameters of the first* $1/2^{+}$ *excited state in* $^{9}$Be *and Astrophysical Implications*. Phys. Rev. C, **82**:015808, 2010.

[80] W. Nörtershäuser *et al. Nuclear Charge Radii of* $^{7,9,10}$Be *and the One Neutron Halo Nucleus* $^{11}$Be. Phys. Rev. Lett, **102**:062503, 2009.

[81] F. C. Barker. *Energy of the First Excited State of* $^{9}$B. Phys. Rev. C, **53**:2539, 1996.

[82] A. G. M. Van Hees and P. W. M. Glaudemans. *A Shell Model Treatment of* $(0+1)\hbar\omega$ *States in* $A = 4 - 16$ *Nuclei (II)*. Z. Phys. A, **315**:223, 1984.

[83] H. Nishioka. *Two Alpha Particle plus Dinucleon Cluster Model for* $^{10}$B *and* $^{10}$Be. J. Phys. G, **10**:1713, 1984.

[84] T. Neff. *Microscopic Calculation of the* $^{3}\mathrm{He}(\alpha,\gamma)^{7}\mathrm{Be}$ *and* $^{3}\mathrm{H}(\alpha,\gamma)^{7}\mathrm{Li}$ *Capture Cross Sections using Realistic Interactions*. Phys. Rev. Lett., **106**:042502, 2011.

[85] H. Feldmeier and J. Schnack. *Fermionic Molecular Dynamics.* Prog. Part. Nucl. Phys., **39**:343, 1997.

[86] T. Neff and H. Feldmeier. *Clustering and Other Exotic Phenomena in Nuclei.* Eur. Phys. J., **156**:69, 2008.

[87] H. Feldmeier, K. Bieler, and J. Schnack. *Fermionic Molecular Dynamics for Ground States and Collisions of Nuclei.* Nucl. Phys., **A586**:493, 1995.

[88] P. Spellucci. *An SQP Method for General Nonlinear Programming using only Equality-Constrained Subproblems.* Math. Program., **82**:413, 1998.

[89] G. H. Golub and C. F. val Loan. *Matrix Computations (3rd edition)*. Johns Hopkins University Press, Baltimore, 1996. Pg 69-75.

[90] T. Neff. *Fermionische Molekulardynamik mit Konfigurationsmischungen und Realistischen Wechselwirkungen.* Diplomarbeit; TU Darmstadt, 1998. Pp 5-6 and 11-12.

[91] R. B. Wiringa, B. G. J. Stokes, and R. Schiavilla. *Accurate Nucleon-Nucleon Potential with Charge Independence Breaking.* Phys. Rev ***C***, **51**:38, 1995.

[92] B. A. Brown. *Lecture Notes in Nuclear Structure Physics*. Unpublished lecture notes, 2005.

[93] R. Roth, T. Neff, and H. Feldmeier. *Nuclear Structure in the Framework of the Unitary Correlation Operator Method.* Prog. Part. Nucl. Phys., **65**:50, 2010.

[94] R. Roth, S. Reinhart, and H. Hergert. *Unitary Correlation Operator Method and Similarity Renormalization Group: Connections and Differences*. Phys. Rev. C, **77**:064003, 2008.

[95] H. Feldmeier, R. Roth, T. Neff, and J. Schnack. *A Unitary Correlation Operator Method.* Nucl. Phys., **A632**:61, 1998.

[96] T. Neff and H. Feldmeier. *Tensor Correlations in the Unitary Correlation Operator Method.* Nucl. Phys., **A713**:311, 2003.

[97] R. Roth, H. Hergert, P. Papakonstantinou, T. Neff, and H. Feldmeier. *Matrix Elements and Few Body Calculations within the Unitary Correlation Operator Method*. *Phys. Rev.* ***C***, **72**:034002, 2005.

[98] T. Neff. *Short-Range Central and Tensor Correlations in Nuclear Many-Body Systems.* PhD Thesis; TU Darmstadt, 2002. Pg 11-14, 69.

[99] P. Maris, J. P. Vary, and P. Navrátil. *Structure of* $A = 7 - 8$ *Nuclei with Two- Plus Three-Nucleon Interactions from Chiral EFT.* Phys. Rev. C, **87**:014327, 2013.

[100] V. M. Datar, S. Kumar, D. R. Chakrabarty, V. Nanal, E. T. Mirgule, A. Mitra, and H. H. Oza. *Direct Observation of the* $4^+$-$2^+$ *Gamma Transition in* $^8$Be. Phys. Rev. Lett., **94**:122502, 2005.

[101] I. Angeli and K. P. Marinova. *Table of Experimental Nuclear Ground State Charge Radii: An update*. At. Data Nucl. Data Tables.

[102] M. A. Oothoudt and G. T. Garvey. *Isospin-mixed states in* $^8$Be. Nucl. Phys., **A284**:41, 1977.

[103] F. Ajzenberg-Selove. *Energy Levels of Light Nuclei* $A = 7$. Nucl. Phys., **A490**:1, 1988.

[104] N. Vinh-Mau. $T = 10$ Effective Interaction in $^{14}$N and $^{10}$B. arXiv:0711.3173v1 [nucl-th], 2007.

[105] S. S. M. Wong. *Introductory Nuclear Physics*. Pearson Prentice-Hall publishers, New Jersey, 2002. Pp 11-13, 261-274 and 372-375.

[106] J.-F. Bonnans, J. C. Gilbert, C. Lemarechal, and C. A. Sagasitzàbal. *Numerical Optimization: Theoretical and Practical Aspects*. Springer-Verlag publishing, New York, 2006. Pg 2.

[107] D. R. Tilley, C. M. Cheves, J. L.Godwin, G. M. Hale, H. M. Hofmann, J. H. Kelley, C. G. Sheu, and H. R. Weller. *Energy Levels of Light Nuclei* $A = 5, 6, 7$. Nucl. Phys., **A708**:3, 2002.

**Acknowledgements**

At the end of what have been three of the most testing, thrilling and transformative years of my life, I find I have so many people to thank for so many things that it may well take another hundred pages to do it all properly! I shall have to content myself with not doing all these wonderful people full justice, and merely writing a few words to each of you.

First I thank the late Prof. Dr Paul Nathanson, without whom I would not be doing Physics at all. Thank you for making it all possible, and for making me believe in myself when I needed it most.

Meeting my supervisor, Prof. Dr Hans Feldmeier, changed my life: without him I would never have moved from a small semi-rural African town to a hub of the European Physics community. My life would have been bereft of many opportunities I now have, and I am indebted indeed. Thank you also for the bicycle - another life-changer!

I also thank Dr Thomas Neff for his insights and guidance, for keeping me motivated, and for laboriously explaining the same things $n$ times (where $n$ is a very large number) during the course of this work. Deepest thanks.

My sister, Dr Helen Henninger, is an example, an inspiration and a wellspring of sanity, strength, insight and love, without whom I would never have got to this place in my life. Thank you, Helen, for more than I can say.

My parents have been amazing. Thank you, Mum, for your presence, for counselling, wisdom, love (and the best home-cooked meals). I am spoiled to have you in my life. Thank you to my father for sharing this journey and for being an example of endurance and courage.

To my colleagues (Sofija, Hans, Gabor, Enrico and Xiaoyu): In your unique ways, you have each provided support, fun and shoulders to cry on throughout these years, and I thank you. Thanks to Maciek for delightful weekly letters, to David for his humour, to Diana, for guidance, and to C for so much. I thank also my late grandmother for years of teaching and support, and for being a great example.

I know that there are many others who have shaped my life and my thinking, and who have brought me to this point. Thank you for everything. Neither this work nor my present happy state would exist without you.

## Lebenslauf

| | |
|---|---|
| Name: | Katharine Rose Henninger |
| Geburtsdatum: | 24 Juli 1987 |
| Geburtsort: | King William's Town (Südafrika) |
| Familienstand: | ledig |
| January 2001 - December 2005 | Clarendon High School for Girls |
| February 2006 - March 2012 | Studium der Physik am Rhodes University, Grahamstown. |
| December 2009: | Abschluss: Bachelor of Science in Physik<br>Titel der Bachelorarbeit: "Proton-scattering observables from Skyrme-Hartree-Fock densities." |
| March 2012 | Abschluss: Master of Science in Experimental Nuclear Physics<br>Titel der Masterarbeit: "In-beam Spectroscopy of $^{72}$Ge" |
| seit Oktober 2012 | Promotionsstudium an der Technischen Universität Darmstadt<br>Doktorandin in der Theorie-Abteilung des GSI Helmholtzzentrum für Schwerionenforschung und Anfertigung der Dissertation. |